# Stellar occultations by Trans-Neptunian Objects and Centaurs : Application to Chariklo and its ring system

Rodrigo Andres Leiva

**Université Pierre et Marie Curie**
**Pontificia Universidad Católica de Chile**

École doctorale d'Astronomie et d'Astrophysique d'Ile de France
Laboratoire d'Etudes Spatiales et d'Instrumentation en Astrophysique (LESIA)/ Instituto de Astrofísica, PUC

# Occultations stellaires pour l'étude des objets trans-neptuniens et les Centaures

*Applications aux anneaux de Chariklo*

# Stellar occultations by Trans-Neptunian Objects and Centaurs

*Application to Chariklo and its ring system*

Par

**Rodrigo LEIVA**

Pour obtenir le grade de

**Docteur de l'Université Pierre et Marie Curie**
**Docteur en Astrophysique, Pontificia Universidad Católica de Chile**

soutenue le 21 Juillet 2017

devant le jury composé de :

| | |
|---|---|
| Bruno SICARDY | Co-directeur de thèse |
| Leonardo VANZI | Co-directeur de thèse |
| César FUENTES | Rapporteur |
| Jean-Marc PETIT | Rapporteur |
| Mme. Marie-Christine ANGONIN | Examinateur |
| Alejandro CLOCCHIATTI | Examinateur |
| Andrés JORDAN | Prof. invité |

## Résumé

Cette thèse a été développée dans le cadre d'une cotutelle entre la Pontificia Universidad Católica de Chile et l'Université Pierre et Marie Curie.

Je décris les tests effectués sur deux kits d'occultation, chacun constitué d'une caméra rapide, d'un système de datation et d'un logiciel d'enregistrement. En plus, j'ai observé plusieurs occultations stellaires par des objet transneptuniens et des centaures, y compris celle qui a mené à la découverte des anneaux de Chariklo.

J'utilise des occultations stellaires pour obtenir les paramètres physiques de trois objets. Pour 2007 $UK_{126}$, je déduis la densité la plus probable en analysant les ajustements elliptiques du limbe sur une occultation stellaire. Pour 2003 $AZ_{84}$, en analysant deux occultations stellaires, je limite la densité et l'orientation de l'objet. Pour le centaure Chariklo, j'adopte une approche statistique bayésienne pour analyser cinq occultations stellaires et je déduis une forme ellipsoïdale de demi-axes $a = 148$ km, $b = 132$ km et $c = 102$ km, avec des irrégularités topographiques de $\sim 6$ km, comparables à celles de satellites de Saturne de taille et densité similaires. L'albédo géométrique du Chariklo est de $3.7 \pm 0.1\%$ et la réflectivité de l'anneau est de $4.9 \pm 0.3\%$.

En fin, j'étudie les résonances de type Lindblad entre le moyen mouvement des particules de l'anneau et la rotation d'un corps irrégulier. L'excès de masse en provenance d'un corps sphérique exerce des moments forts sur un disque collisionnel, et repousse le matériau situé au niveau du rayon de la corotation jusqu'à la résonance la plus externe. Pour Chariklo, les courtes échelles de temps ($< 10^5$ ans) expliquent l'emplacement actuel de ses anneaux.

# Abstract

The present PhD thesis has been developed in the context of a cotutelle between the Pontificia Universidad Católica de Chile (PUC) and the Université Pierre et Marie Curie (UPMC). The first half of the PhD was done in the Instituto de Astrofísica at PUC and the second half at the Laboratoire d'Etudes Spatiales et d'Instrumentation en Astrophysique (LESIA) at the Observatoire de Paris, in the context of the European Research Council (ERC) project "Lucky Star", whose goal is to study the small objects of the outer Solar System using stellar occultations.

Here, I address three important stages of the project: observations with fast cameras, data analysis and physical interpretation of the results.

In the first part I describe tests performed on two occultation kits, each consisting in a fast camera, a time registration system and an acquisition software. I show that the EMCCD-based camera performs better than the alternative CMOS camera, reaching stars one magnitude fainter in equivalent conditions. The time registration system (the TimeBox device) has an accuracy below 20 ms with respect to the UTC reference time which is adequate for the timing of the observation of stellar occultations. Interactions with the acquisition software manufacturer lead to the adaptation of such software to the needs of the project.

In the second part I study the physical characterization of three object with the analysis of stellar occultations. For the scattered disk object 2007 $UK_{126}$ I derive the range and more probable density values analyzing the elliptical fits to a multi chord stellar occultation. For the plutino 2003 $AZ_{84}$ I constrain the range of compatible density and orientation to a narrow region around $\sim$870 kg m$^{-3}$ and opening angle $B \sim 48^{\circ}$ analyzing two multi-chord stellar occultations. The main subject of this section is the adoption of a Bayesian-MCMC approach for analysis of five stellar occultations by the Centaur object Chariklo. Chariklo appears to be consistent with an ellipsoid with semiaxes $a = 148^{+6}_{-4}$ km, $b = 132^{+6}_{-5}$ km, and $c = 102^{+10}_{-8}$ km presenting topographic features of the order of 6 km. From this nominal model, I derive a body geometric albedo of 4.9$\pm$0.1% and a ring reflectivity of 3.7$\pm$0.3%. The topographic features for this model are $\sim$ 6 km, comparable to those of Saturnian icy satellites with similar size

and density.

In the third part, I consider Lindblad resonances between the mean motions of ring particles and the rotation of an irregular body. Mass excess departing from a spherical body exert strong torques on a collisional disk that clear the material from the corotation radius up to the outermost resonance. Application to Chariklo indicates very short clearing timescales ( $< 10^5$ years) and explains the current location of the rings.

# Contents


**1 Introduction** **7**

**2 Characterization of cameras and time acquisition** **25**
2.1 Conversion factor and read-out noise . . . . . 27
2.1.1 CMOS camera . . . . . 29
2.1.2 EMCCD camera . . . . . 32
2.2 Dead times . . . . . 36
2.2.1 CMOS camera . . . . . 36
2.2.2 Kite camera . . . . . 37
2.3 Accuracy of time registration . . . . . 38
2.4 Test at the sky and SNR estimation . . . . . 40

**3 Physical characterization by stellar occultations** **43**
3.1 2007 $UK_{126}$ and 2003 $AZ_{84}$ . . . . . 45
3.1.1 Stellar occultation by 2007 $UK_{126}$ . . . . . 45
3.1.2 Stellar occultation by 2003 $AZ_{84}$ . . . . . 47
3.2 Size and shape from multi-epoch stellar occultations . . . . . 49
3.2.1 Body models . . . . . 49
3.2.2 Bayesian approach . . . . . 51
3.2.3 Shape and size of the Centaur object (10199) Chariklo 55

**4 The dynamics of rings around a non-spherical body** **103**
4.1 Two simple cases of non axisymmetric potential . . . . . 104
4.2 Lindblad resonances . . . . . 107
4.2.1 Single-mass anomaly . . . . . 108
4.2.2 Triaxial ellipsoid . . . . . 110
4.2.3 Summary of the section . . . . . 111

4.3 Corotation resonance . . . . . 112
4.3.1 Azimuthal dependence of the corotation potential . . 112
4.3.2 Stability of the corotation fixed points . . . . . 114
4.4 Evolution of a debris disk: Lindblad resonances . . . . . 115
4.4.1 Torques at Lindblad resonances . . . . . 115
4.4.2 Angular momentum deposition . . . . . 116
4.4.3 Truncation of the disk . . . . . 118
4.4.4 Clearing the corotation zone: time scales . . . . . 118
4.5 Applications to Chariklo's ring system . . . . . 119
4.5.1 Lindblad resonances . . . . . 120
4.5.2 Corotation resonances . . . . . 123
4.6 Discussion . . . . . 124

**5 Conclusions 129**

**A Potential of a homogeneous triaxial ellipsoid 145**
A.1 Axisymmetric part of the potential . . . . . 147
A.2 Resonant terms . . . . . 148

**B Search for gas emmision from Chariklo with ALMA 151**

**C Other observations 157**

# List of Figures


1.1 Description of a stellar occultation. . . . . 10
1.2 Perihelion distance vs eccentricity of ETNOs. . . . . 17

2.1 Noise versus average signal for CMOS. . . . . 30
2.2 Signal variance for CMOS. . . . . 31
2.3 Signal variance for EMCCD. . . . . 32
2.4 Deadtimes for CMOS. . . . . 36
2.5 Cameras spectral response. . . . . 40
2.6 SNR for Kite and CMOS. . . . . 42

3.1 Chariklo's rotation angle in 2013. . . . . 57
3.2 Equivalent radius $r_{\rm eq}$ as a function of time. . . . . 60

4.1 Models considered for the Lindblad resonances. . . . . 105
4.2 Structure of corotation orbits. . . . . 112
4.3 Normalized torque density functions. . . . . 117
4.4 Migration of ring particles away from corotation radius. . . . 120
4.5 Disk truncation by resonant torques. . . . . 122

A.1 Values of $\log(S_p)$ vs. $p$. . . . . 149

B.1 Chariklo imaged with VLT/SPHERE. . . . . 153
B.2 Expected CO(2-1) line flux with ALMA. . . . . 156

# List of Tables


2.1 Camera features. . . . . 26
2.2 Readout noise for CMOS camera. . . . . 31
2.3 Conversion factor for the Kite camera. . . . . 34
2.4 Readout noise for the EMCCD Kite camera. . . . . 35
2.5 Dead time for the CMOS camera. . . . . 36
2.6 Dead time for the Kite camera. . . . . 37
2.7 Time difference respect to UTC. . . . . 39

4.1 Strength of Lindblad and corotation resonances . . . . . 127
4.2 Torque densities near a Lindblad Eccentric Resonance (LER) 128

A.1 Values of $S_p$ . . . . . 149

C.1 Observations of stellar occultations from Observatory UC. . 158

# Chapter 1

# Introduction

The present PhD thesis has been developed in the context of a cotutelle between the Pontificia Universidad Católica de Chile (PUC) and the Université Pierre et Marie Curie (UPMC). The first half of the PhD was done in the Instituto de Astrofísica at PUC and the second half at the Laboratoire d'Etudes Spatiales et d'Instrumentation en Astrophysique (LESIA) at the Observatoire de Paris.

During my stay at PUC, my work involved the observations and data reduction of stellar occultations by several transneptunian objects (TNOs) and Centaur objects mainly from the teaching observatory at PUC (see Appendix C). During this period, I was one of the co-discoverers of rings around the small Centaur object Chariklo, during the 2013 June 3 stellar occultation that was observed from several sites in South America. During my stay at Paris Observatory, I continued my involvement in observations of stellar occultations, concentrating my work on the analysis of observations to characterize the physical parameters of the occulting objects.

This thesis addresses three important stages of stellar occultations: observations, data analysis and physical interpretation.

The first step focuses on the sensitivity and timing accuracy of the cameras that we are using for simultaneous observations of occultations.

The second part of the thesis addresses the problem of how to extract physical properties of an outer Solar System object from occultation data.

My work concentrates on the Centaur object Chariklo, using stellar occultations observed between 2013 and 2016.

However, I also worked on the Scattered Disk Object TNO's 2007 $UK_{126}$

and the plutino object 2003 $AZ_{84}$, see below.

The third part of my thesis is to study the dynamics of rings around an irregular body such as Chariklo. In particular, I investigate how the elongated shape and/or topographic features of Chariklo may affect the ring dynamics through spin-mean motion resonances.

This thesis work has been done in the context of the European Research Council (ERC) project “Lucky Star", whose goal is to study the small objects of the outer Solar System using stellar occultations.

#### Portable cameras and time registration

A stellar occultation can be visible from any part of the Earth's surface. The path of the occultation shadow span from a few tenths to several hundred kilometers. This corresponds essentially to the size of the occulting object plus distortions by the Earth's sphericity, refraction for bodies with atmospheres and possibly relativistic effects for the massive giant planets. With some exceptions as Pluto and Chariklo, the occultation path for TNOs and Centaurs has typical uncertainties of a few hundred kilometers. In the scenario of the positive detection of an occultation, it is also required an appropriate extension in the geographic coverage in order to derive the size, shape, orientation, and topographic features of atmosphereless objects; derive the geometry of ring systems (e.g. Chariklo); reconstruct atmospheres geometries (e.g. Pluto); and detect the presence of debris, satellites and rings around the objects.

Given this facts, it is clear that the observation of stellar occultations cannot rely solely on the use of fixed observatories. Given that stellar occultations by TNOs and Centaurs are rare, and that predictions of those events require huge efforts, the planning of observations must involve the use of mobile stations, so that to improve the chances of detection and to obtain useful results.

As stated before, photometric light curves from occultations must have good absolute time accuracy (some 0.1 second or better) in order to compare the occultation chords from different stations. It must be remembered that the shadow of a body on Earth typically moves at a velocity of 20 km $s^{-1}$, so a 0.1 s error means a corresponding 2-km error for the size of a body, its

atmosphere and/or its rings. This may result in wrong conclusions on the size, shape of the objects under study.

Additionally, the acquisition cycle time sets the spatial resolution obtained in an occultation light curve. Considering again the 20 km $s^{-1}$ velocity mentioned above, an acquisition rate of ten frames per second (fps) means a spatial resolution of 2 km. This scale is typical, for instance, of the gravity waves observed in Pluto's or Titan's atmospheres. Likewise, this is of the order of topographic features at the surfaces of small bodies, or of the fine structures observed in rings. High cadence implies the camera used must have short *dead times* between image acquisitions, of the order of a fraction of a second. In other words, we want the camera effectively capturing photons most of the time.

Conversely, high acquisition rates of, say, 40 fps are in general useless. They correspond to distances, traveled in the sky plane, of some 0.5 km. At that stage, Fresnel diffraction and/or the finite stellar diameter limits the achievable resolution to about one kilometer. This makes high acquisition rates (associated with high prices for the camera) usually superfluous.

Data acquisition during a stellar occultation typically requires several minutes. This is done to take into account the uncertainties in the occultation predicted time, to search for debris, satellites and rings around objects, and to have a good baseline for the photometry analysis. The high cadence combined with long acquisition time also imposes some practical and non-trivial characteristics of the acquisition software. In particular, it is desirable to have the possibility to acquire sub-sections of an image (usually called Regions Of Interest, ROI), so that (1) to have data set of reasonable size and (2) record images at a high rate, thus avoiding image loss.

Given these circumstances, the use of mobile stations requires the use of (1) a sensitive camera, (2) a reliable time registration chain and (3) dedicated acquisition software. Cameras must have other practical desirable characteristics, not less important than the technical ones mentioned above. They must be small and lightweight so that they can be easily transported and used on small telescopes.

Finally, the budget is always a constrain and a compromise must be reached between the desirable characteristics of the system and the price

such that enough mobile stations can be deployed and the scientific goals can be achieved.

**Physical characterization of TNOs from Stellar occultations**

As mentioned above, a large part of the thesis makes use of the stellar occultations technique to study minor bodies of the Solar System, in particular TNOs and Centaur objects. In practice, an occultation occurs when the light of a star is blocked totally or partially by an object passing in front of it (Figure 1.1).

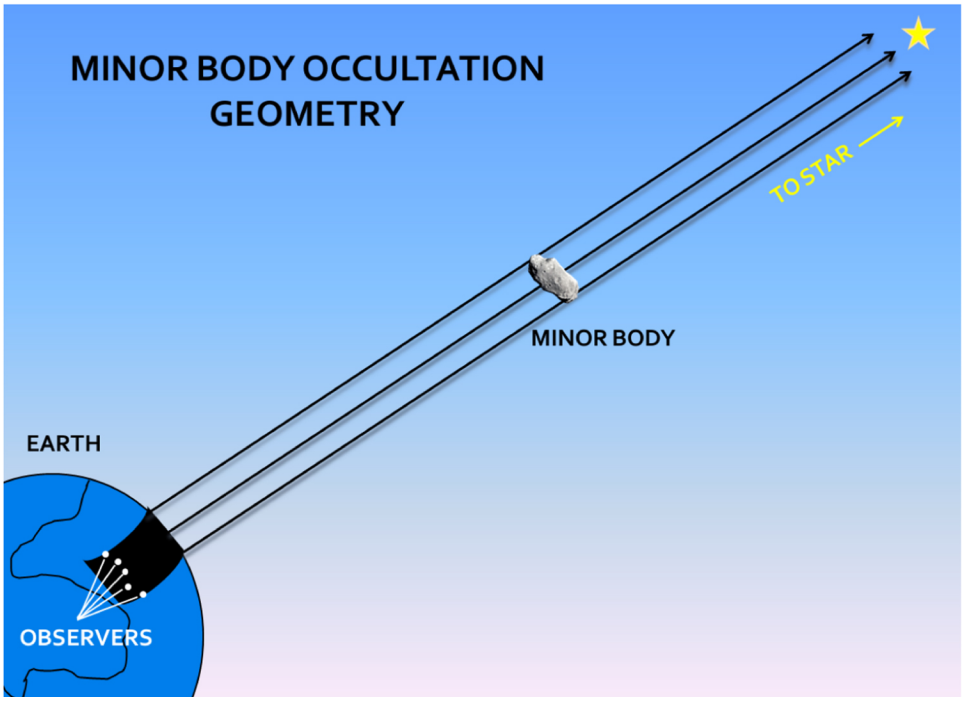


Figure 1.1: A stellar occultation occurs when the light of a star is blocked totally or partially by an object passing in front of it. The shadow projected by the object is observed from several locations simultaneously. The durations and the respective positions of the "occultation chords" allow us to reconstruct the projected shadow (size and shape) of the object at the moment of the occultation, while the shape of the ingress/egress light curves provide details of the local topography. Figure from (Santos-Sanz et al., 2016).

Observers located at different locations in the shadow path measure the instants of disappearance and reappearance of the star. The duration of the occultation is then translated into a segment in the sky plane at the distance of the occulting object. Here, we will refer it as an "occultation chord".

The analysis of these occultation chords then gives constraints on the size and shape of the object. The accuracy of the measurements is typically a few kilometers and depends mainly on the cadence of the photometric acquisition. In some cases, extra information about topography can be obtained from features of the light curve, produced by diffraction effects at the limb of the object.

The data used in this work mainly consist in stellar occultations by the Centaur object Chariklo observed between 2013 and 2016. The observations are scarce and separated by months to years and, in each case, only one or two stations detected the occultation by the main body. The data considered here involve occultation both by Chariklo's main body and by its rings. In those cases, the general geometry of the ring system can be constrained. Note that observation providing negative results (that is, no occultation by the body nor by the rings) also give strong constrains in the extension of the object if the occultation chords are sufficiently close to it.

Classically, size and shape are derived from stellar occultations by adjusting a circular or elliptical limb model to the occultation chord extremities. These fits account for uncertainties in the chord extremities product of the uncertainties in timing registration of the star disappearances and reappearances. This simple approach has provided size estimates for a dozen of objects (TNOs and Centaurs) with typical formal uncertainties in the range of few kilometres.

If the mass of the body is known independently (usually from a satellite motion), then constraints on the size provide constraints on the bulk density and, from there, on the bulk composition and on porosity for an assumed composition. Assuming that the body is relaxed or in equilibrium, other questions can be addressed. For instance, equilibrium shape for an homogeneous body depends on the density and rotational speed. So, in the absence of mass determination, knowledge of rotation period may also gives constraints on the density.

Most of occultations by TNOs and Centaurs have been observed only once. An obvious limitation of this is that we need to derive a tridimensional shape based solely on a bidimensional projection at a unique time.

When several stellar occultations at different epochs are observed for

a given object, then the tridimensional shape can be better constrained if the changing geometry is taken into account. For instance, a spherical object generates a circular shadow with a constant size. A spheroidal object generates elliptical profiles roughly of the same size, shape and orientation. But its size slowly changes with time as the aspect of the object changes as seen from Earth. Finally, an ellipsoidal object can generate circular or elliptical profiles of variable size and orientation on few hours timescale.

In the most general case, when we obtain elliptical limbs with different sizes and/or orientations with occultations observed at different dates, we need to consider more general shapes and deal with different possible orientations and shapes for the body. When only one or two chords are observed during an occultation, no elliptical profile can be fitted (five points are needed to uniquely define an ellipse) but such occultation can give information by combining it with others observations.

The data from stellar occultations are complemented with the short-term and long-term photometric variability of the object. The long-term brightness variability, on years timescale, provides independent constraints in the size and albedo of the object, since they correspond to different aspects of the object. On the other hand, the short term variability, in the range of hours, gives clues about the elongation of the body, using rotational light curves.

Observations of stellar occultation by Chariklo are still scarce.

In that context, I adopt here a Bayesian statistical approach to derive the most probable values of the models parameters. Spherical, spheroidal and ellipsoidal models for the shape are then considered, motivated by physical considerations and observational data. In this approach, the physical considerations and photometric evidences are incorporated quantitatively to derive constraint in the parameters of these models. This approach has also the advantages to provide an incremental knowledge in the shape and size of the object under the light of new evidence.

This also gives guidelines for the planning of new observations in order to improve the scientific payoff.

This thesis only considers occultations by opaque objects. Modeling of atmospheres and occultation by semi-transparent rings are out of the

scope of this work. Here, the rings are assumed circular, concentric with the central body and located in the equatorial plane of the body. These hypothesis provide an a priori orientation of the main central body, that is the position of the apparent center of the object and how its rotation axis is oriented in the sky.

Finally, it is worth mentioning that this thesis is developed in the time frame of the first Data Release (DR1) of the *Gaia* mission. Gaia provides accurate positions for a thousand million stars. While the DR1 catalog has typical accuracy of $\sim 5$ milliarcsec (mas) when propagated from the initial epoch (2015.0) to, say 2017, subsequent releases will improve the accuracy of positions and provide also proper motions. For instance the DR2 release will have a typical accuracy of 0.2-0.3 mas . The availability of accurate stellar position will considerably improve the accuracy of the predictions and consequently will increase the amount of successful stellar occultation by TNOs and Centaurs. Under this scenario, the approach I adopted is to have in mind its applicability to the broader goal of the Lucky Star project, i.e. to improve the analysis of multi-chord and multi-epoch stellar occultations by other TNOs and Centaurs.

**How asphericity and irregularities affect dynamics around Small objects**

The third part of this thesis is the description of resonances between the spin of an irregular body and the mean motion of orbiting particles. The motivation is the existence of a double ring system around the Centaur Chariklo.

Besides Chariklo, only the giant planets of our Solar System are known to posses rings. They have nearly axisymmetric gravitational potential, with negligible equatorial bulges and departures from axial symmetry. The main source of resonances in planetary rings are thus with satellites.

Results from stellar occultations and long term photometric behavior suggest that Chariklo is not spherical. From what it is known about icy satellites in the same range of size and expected density (e.g. Phoebe, Hyperion), Chariklo is expected to have topographic features in the order of 5-10 % of its radius.

Both, elongation and topographic features generate non-axisymmetric terms in the gravitational potential. In the similar case of satellites perturbing rings, these terms in the potential generate resonances in the ring particles orbiting close to the object.

Two basic models are considered in this thesis. The first is a spherical body with uniform density with a small mass anomaly located in the equator and the second is an elongated triaxial ellipsoid. No other North-South asymmetries are introduced and only ring particles in the equatorial plane of the body are considered. These simplified models resemble the shape models considered in the analysis of the occultations and the level of irregularities constrained from the observations.

Both models generate, in the gravitational potential, non-axisymmetric terms acting in particles in the equatorial plane. Lindblad and corotation resonances (still to be defined) will be considered and analyzed.

Chariklo and its ring system constitute a rich laboratory that will make it very interesting to compare with the giant planets rings. The best studied example, the Saturn ring system, shows a rich and complex variety of phenomena with interactions with several satellites trough resonances, interaction with the magnetic field of the planet and replenishing of material from satellites. In the case of Chariklo, the system is in some aspects simpler with only two rings and the gravitational potential of the central body as main elements.

In spite of its difficulties, the stellar occultation technique remains the most powerful tool we have from the ground to study a system as Chariklo and its rings.

## Road map

The next chapters of the thesis are developed as follows. First, Section 1 provides a review of the literature about TNOs and their relations with Centaur objects. It includes a description of the observational techniques used for their physical characterization, and how they complement the stellar occultation method. It also includes a summary of main topics about orbital dynamics, rings around elongated and irregular bodies and the scenarii proposed so far for the origin of Chariklo's rings.

Chapter 2 describes the tests I performed on the fast portable cameras used by the Lucky Star project to record stellar occultations. I also describe the tests I did to assess the time registration accuracy.

Chapter 3 describes the physical characterization of minor bodies obtained thanks to stellar occultations.

Chapter 4 develops the models and formalisms used to analyse resonance effects between an irregular and/or elongated body and a collisional disk.

Conclusions highlights the main results, possible improvements and perspectives.

Other activities that I had, related with the main topics described above, are included in the Appendices. More precisely, Appendix B described the current status of an ALMA program approved during Cycle 4 to search for CO gas around Chariklo, and for which I am the P.-I. Finally, Appendix C summarizes the observations I participated in during the development of this thesis.

## Background

TNOs are small objects orbiting in the vast region outer region of the Solar System that extends beyond Neptune (with semimajor axis a=30 au). The existence of objects beyond Neptune, remaining from the early Solar System and too sparce to form planets, were proposed by Edgeworth (1949). After the discovery of Pluto in 1930 and the so-called first Edgeworth-Kuiper Belt object 1992 $QB_1$ (Jewitt & Luu, 1993), more than 2000 TNOs have been discovered as of today (Minor Planet Center, 2017).

Several dynamical structures had been identified in the trans-Neptunian region, such as the resonant objects, the scattered disk Luu et al. (1997), the classical belt and the extended scattered disk. These structures were sculpted by interactions with the giant planets during the planets migration in the early Solar Sytem (Levison & Morbidelli, 2003).

Figure 1.2 ((Sheppard et al., 2016)) shows recently discovered extreme transneptunian objects (ETNOs) with perihelion beyond 50 au (Allen et al., 2006; Chen et al., 2013; Sheppard et al., 2016; Sheppard & Trujillo, 2016). Among these, we find Sedna, with semimajor axis $a = 480$ au and a perihelion $q = 76$ au, and 2012 $VP_{113}$ with $a = 266$ au and $q = 80$ au. These objects are part of the Inner Oort Cloud, with semimajor axes that are too large to be explained by interactions with Neptune (Brown et al., 2004; Trujillo & Sheppard, 2014). Surprisingly, the argument of perihelion of several ETNOs seem to be clustered. A possible explanation is the existence of a massive planetary object in the transneptunian region (Trujillo & Sheppard, 2014).

TNOs are small bodies that probably were never part of a larger planet-size object. Then, they are not modified by endogenous geological processes as are the planets. Given the great distance from the Sun, TNOs preserve most of the volatiles and they are a reservoir of primordial material preserving a record of the formation of the Solar System. Together with their relatives, the Centaur objects, orbiting between the giant planets, the TNOs contain valuable information about the formation and evolution of the Solar System in their physical properties such as bulk density and surface composition.

Unfortunately, to determine the physical properties of these objects is a

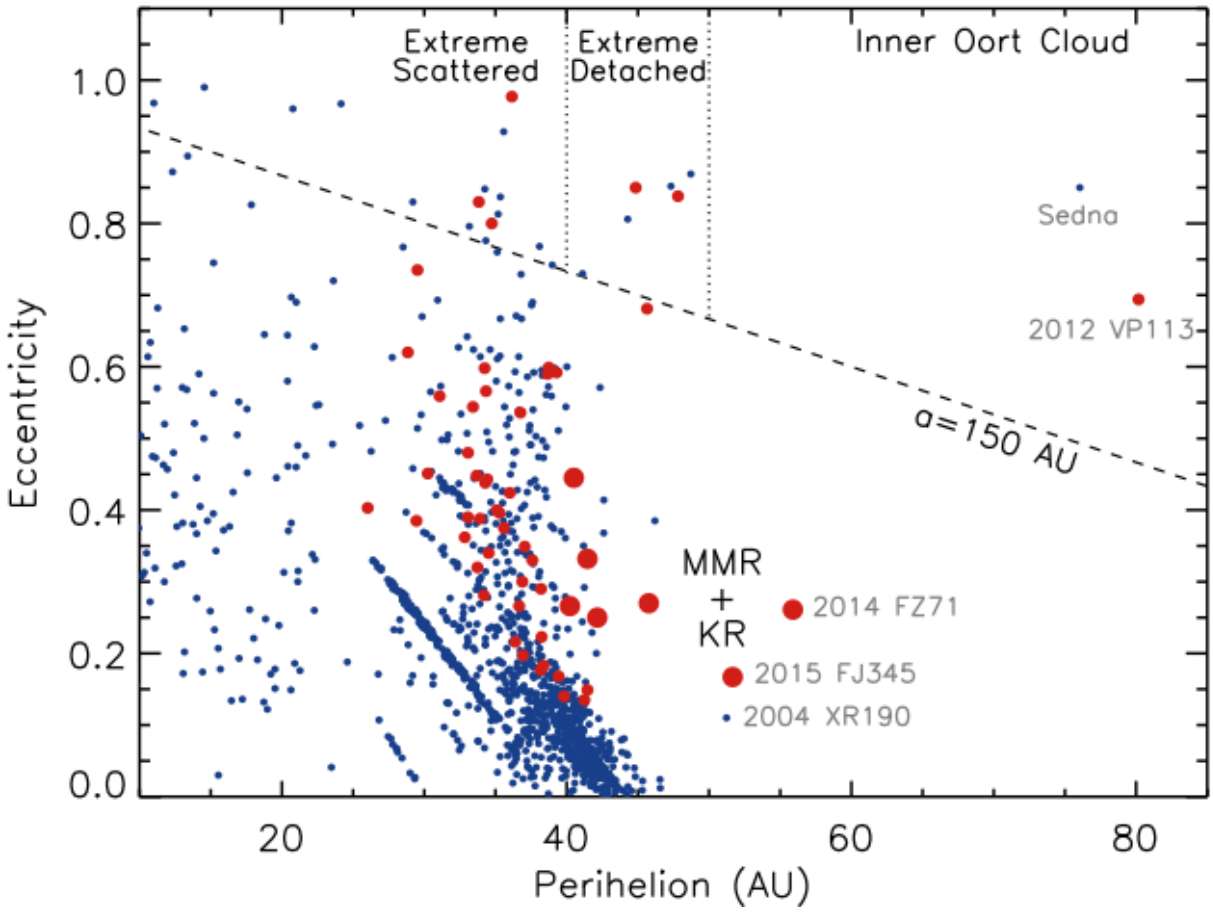


Figure 1.2: Perihelion distance vs eccentricity of transneptunian objects showing some of the recently discovered extreme TNOs and Inner Oort Cloud objects (Sheppard et al., 2016).

difficult task and the TNOs and Centaurs are poorly characterized. Sizes and shapes, albedos, thermal properties, surface and bulk compositions, internal structure and density are fundamental properties but difficult to measure for these distant and small objects.

### Centaurs as TNO relatives

The Centaurs are small objects orbiting the Sun between Jupiter and Neptune. Using the MPC definition "Centaur object have perihelia beyond the orbit of Jupiter and semimajor axes inside the orbit of Neptune", there are more than 200 known Centaurs (Minor Planet Center, April 2017).

Centaur objects are dynamically linked to the TNOs. Perturbations by

giant planets make theirs orbits chaotic. Numerical integrations indicate that the typical half-life of a Centaur is $\sim 10^7$ year. After that time, a typical Centaur is ejected from the Solar System, is captured by a giant planet, migrates into a transneptunian orbit or becomes a Jupiter-family comet (Tiscareno & Malhotra, 2003; Horner et al., 2004).

Centaurs, after having formed in the transneptunian region, undergo interactions with Neptune and migrate inward in the giant planet region. Different regions of the outer Solar System can be the origin of the Centaurs. For instance, the Classical Kuiper Belt (Levison & Duncan, 1993), the Scattered Disk (Duncan, 1997), Neptune trojans (Horner & Lykawka, 2010), the plutinos (Yu & Tremaine, 1999) are all possible origins of at least a fraction of the Centaurs population.

Centaurs give us the opportunity to take a closer look at the primordial material of the outer Solar System with the advantage of being brighter and hence relatively less difficult to study. Moreover, some Centaurs exhibit cometary-like activity and provide the chance to study the material sublimated from their surfaces. Among the largest active Centaurs are Chiron ($\sim$100 km) (Meech & Belton, 1990) and Echeclus (84 km) (Rousselot, 2008). The exothermal conversion of amorphous water ice into crystalline with liberation of trapped carbon monoxide (CO) has been proposed as the main source of volatiles in objects beyond 10 au (Prialnik et al., 1995; Choi, 2002). Among a study including 23 Centaurs, 9 of them exhibit a detectable coma. The activity in these Centaurs is thermally driven given that their average perihelia (5.9 au) was smaller than their inactive counterparts (8.7 au). The observed activity is compatible with the water ice crystallization mechanism (Jewitt, 2009).

#### The Centaur object (11990) Chariklo

The Centaur object (10199) Chariklo was discovered in 1997 and it is the largest known Centaur with an equivalent radius of 119 km (Fornasier et al., 2014). Chariklo showed a sustained decrease in its brightness of about 0.6 magnitudes between its discovery and 2008 (Belskaya et al., 2010). In the same time period, the absorption feature at 1.5 and 2 $\mu$m in its spectrum revealed the presence of water ice (Brown & Koresko, 1998; Brown, 2000;

Dotto et al., 2003), with the subsequent disappearance of the water ice feature in the following years (Guilbert et al., 2009).

To explain this intriguing behavior, Guilbert-Lepoutre (2011) proposed a thermophysical model where Chariklo experiences cometary activity. However, no cometary activity has been detected so far around Chariklo by direct imaging and an upper limit for the dust production rate has been estimated in 2.5 kg $s^{-1}$ (Guilbert et al., 2009; Fornasier et al., 2014). Similarly, no gas emission has been detected so far around Chariklo. Search for CO emission puts an upper limit of $\sim 10^{28}$ mol $s^{-1}$ at heliocentric distance of 13.5 au (Bockelee-Morvan et al., 2001). The increased sensitivity of the Atacama Large Millimeter Array (ALMA) will detect fainter CO emission or put tighter upper limits (see Appendix B)).

An alternative explanation was given for these observational features after the discovery of rings around Chariklo. The stellar occultation by Chariklo in 2013 revealed the presence of a $\sim$400 km radius ring system. The observation of this occultation involved about a dozen of observation sites spread in South-America from small 40 cm telescopes up to 1.5 m telescopes (including a station near Santiago de Chile, from which I contributed to the ring discovery (Braga-Ribas et al., 2014b)).

The higher signal to noise ratio observations at the 1.5-m Danish telescope actually revealed two rings at ingress and egress (ie before and after the occultation by Chariklo's main body). Several other stations detected the rings. These detections, even unresolved, helped to constraint the orientation and size of the system. The observations fitted well to two concentric and circular rings of radius 390.6 km and 400.3 km respectively.

After the reappearance of the water ice features in 2013 and with the ring model deduced from stellar occultations, the photometric and spectrometric behavior of Chariklo was consistently explained by the changing orientation of icy rings as seen from Earth. Under the assumption of a spherical body, the reflectivity of the rings was found to be $\sim$ 9 %, while a spheroidal body lowered the estimate to $\sim$ 6 % (Duffard et al., 2014; Braga-Ribas et al., 2014b) that compares to Chariklo's dark surface (geometric albedo near 4%). This will be discussed again on Chapter 3.

Chariklo's ring formation is not yet understood, but some mechanisms

have been proposed. Rings can form around a differentiated Centaur object after close encounter with giant planets (Hyodo et al., 2016). While this favors the formation of Chariklo's ring during its Centaur stage (before its migration from the transneptunian region), close encounter of Centaurs with giant planet are unlikely (Wood et al., 2017). For Melita et al. (2017), the formation of rings after a collision is unlikely during the lifetime of Chariklo as a Centaur and is more likely in the primordial transneptunian belt where collisions were more frequent. Finally, Chariklo's rings are stable under perturbations by planetary encounters, suggesting that rings around Centaurs may be a common feature if an efficient ring formation mechanism exist (Araujo et al., 2016).

### Stellar occultations

A stellar occultation occurs when an object pass in front of a star blocking totally or partially its light. It is a powerful technique that allows kilometric absolute accuracies on the shape of remote bodies in the solar system. This technique is more fruitful when a stellar occultation is observed simultaneously from several locations, which samples different regions of the occulting object, or more precisely, of its limb. The rotation period of TNOs is typically of a few hours while the duration of an occultation is in the range of seconds to a few minutes. Then, the rotation of the object can be neglected and what is obtained is a discrete sampled snapshot of the limb of the object (Elliot, 1979).

From the analysis of light curves taken from several locations simultaneously, we can infer some properties of the occulting object. Each light curve provides a so-called "occultation chord", whose duration is translated into a chord length in the sky plane at the distance of the occulting object. Note that even a single chord provides a hard lower limit for the size of an object.

The accuracy of the measurements greatly depends on the Signal to Noise Ratio (SNR), time resolution, and absolute time accuracy of the photometric light curve. Higher SNR are obtained for brighter stars and/or observations with larger telescope apertures and, clearly, none of these two aspects can be controlled.

In the pre-Gaia era, the uncertainties on occultation predictions was typically 30 milliarcsec (mas) projected in the sky plane (300-1000 km projected on Earth, depending of the object), while the occultation shadow projected on Earth's surface is usually narrow (ie the diameter of the object, some hundreds of km). Thus, the geographic coverage of observers must be relatively large, so that to increase the chances of success. To reconstruct the 2D shadow of the occulting body from simultaneous light curves, the homogeneity of data is of paramount importance. Then, observations with portable telescopes, trustful fast cameras and reliable time registration are critical.

Stellar occultations by TNOs and Centaurs are still scarce. It is largely because of the difficulty of predictions. The uncertainties in predictions arise from uncertainties on the star positions and on the ephemerides of the occulting objects. Until recently, UCAC4 (Zacharias et al., 2013) was the most accurate source of stellar positions, with positional accuracy of 15-100 mas per coordinate. However, the mid-epoch is between 1998-2004 and proper motion error of 1-10 mas $\mathrm{yr}^{-1}$, which quickly deteriorates the position determined after a few years. The use of existing stellar catalogs makes the prediction of stellar occultations by distant objects impracticable.

One approach for improving the predictions is to obtain local astrometric catalogs of stars in the path of the candidate objects. With this approach, a typical relative uncertainty of ∼50-100 mas is obtained for prediction of the major TNOs and Centaurs (Assafin et al., 2010, 2012; Camargo et al., 2014). New astrometric positions of objects of interest are then reduced with this local catalogs to determine offsets with respect to a reference ephemerides or to recalculate the orbit of the object (Fraser et al., 2013; Desmars et al., 2015). For a body at a distance $d$ in astronomical units (au), an uncertainty in the relative position between star and the object of $\sigma_{mas}$ translates into an uncertainty of $\sigma_d = 0.725 * d_{au} * \sigma_{mas}$ in the path of the occultation shadow. Then, a typical uncertainty of up to 100 mas translates into ∼3000 km for a typical TNO (at $\sim$ 40 au) and ∼1000 km for a typical Centaur (at $\sim$ 15 au). These uncertainties make the planning of occultation observations difficult.

*Gaia*, currently in its first Data Release (2016), provides stellar positions

with typical uncertainties of $\sim 10$ mas for the main bulk of 1.1 billion stars and proper motions with uncertainties of $\sim 1$ mas yr$^{-1}$ for the TGAS subset of 2 million brighter stars Gaia Collaboration et al. (2016b,a). Subsequent releases will improve the position accuracy and proper motions for the full catalog allowing to obtain accurate stellar position. In the meantime, the UCAC-5 catalog provides proper motions with typical accuracies of $1-2$ mas yr$^{-1}$ in the range R=11-15 mag, degrading to $\sim 5$ mas yr$^{-1}$ for 16-magnitude stars (Zacharias et al., 2017).

The availability of such accurate star positions and proper motions will improve significantly the accuracy of the predictions of stellar occultations. The availability of an homogeneous and accurate stellar catalog will improve the reduction of new positions of TNOs and Centaurs, as well as those positions from the re-reduction of old images. Finally, the detection of positive occultations is in itself an accurate astrometric measurement of the occulting object. This will result in a virtuous circle in the prediction of subsequent occultations by the same object.

Several ground based stellar occultations by the larger TNOs and Centaurs had been observed and reported so far. Stellar occultation revealed the presence of an atmosphere in Pluto (Hubbard et al., 1988; Elliot et al., 1989). Since then, the atmosphere of Pluto has been monitored revealing a sustained expansion, well after its perihelion (Brosch, 1995; Elliot et al., 2003; Sicardy et al., 2003; Dias-Oliveira et al., 2015). The second successful observation of a stellar occultation by an TNO (other than Pluto) was recent with the occultation by 2002 $TX_{300}$ in 2009 (Elliot et al., 2010). This provided an accurate radius of $143\pm5$ km and the object resulted to be highly reflective, with an geometric albedo of 0.88. Over a dozen other TNOs and Centaurs has been observed with stellar occultations, among those Eris (Sicardy et al., 2011), Makemake (Ortiz et al., 2012), Varuna (Sicardy et al., 2010), Quaoar (Braga-Ribas et al., 2013), 2002 $KX_{14}$ (Alvarez-Candal et al., 2014), 2007 $UK_{126}$ (Benedetti-Rossi et al., 2016; Schindler et al., 2017) and 2003 $AZ_{84}$ (Braga-Ribas et al., 2011). Other unpublished results include occultations by 2003 $VS_2$, Sedna, Asbolus and 2005 $TV_{189}$ (Braga-Ribas et al., 2014a).

These observations provide accurate size, shapes and albedos. However,

these results must be interpreted with caution as the data are limited and the results are sensitive to assumptions. For instance, the stellar occultation by Makemake leads to an accurate bulk density in one case (Ortiz et al., 2012) while a reanalysis of the same data concludes that no constraint in the density can be obtained (Brown, 2013). In this thesis, a statistical approach similar as to Brown (2013)'s is adopted where all assumptions are based in physical constrains or observational evidence complementing the results from stellar occultations.

Finally, the detection of rings around Chariklo opens a new set of questions: How and when these rings formed?, what are the mechanisms of rings confinement and how common are ring systems among Centaurs and TNOs? With less than 100 mas across projected in the sky plane (rings included), Chariklo's system can not be resolved from Earth-based telescopes and this makes its study difficult. As for other outer solar system objects, stellar occultation is a unique and powerful technique to study this system. Knowing the size and shape of Chariklo and the geometry and evolution of the rings will help to understand the dynamics of the system.

The results from stellar occultations benefit from complementary observations, such as time-resolved photometry and radiometric techniques. The objects brightness variation in time scale of hours and in longer time scales of years gives clues about the their shape and albedo. Photometric light curves show variations of brightness. They are due to changes in the projected area of the object with the body rotation, or to albedo variegations or, more in general, by a combination of both. The inversion of rotational light curves has been used to derive shapes and thermal properties of asteroids and can, in principle, be extended to TNOs (Durech et al., 2017).

The light received by a body from the Sun is partially reflected while the rest is absorbed to be re-emitted as thermal radiation at longer wavelengths. Combining observations in visible and in thermal infrared allows us to derive the size and geometric albedo of a body. The Herschel Key Project "TNOs are cool" characterized about 140 of the largest (>200 km) TNOs and Centaurs providing size, albedo and thermal properties. Knowledge of the mass of about twenty of those objects also provides density estimates. From a representative sample of objects in the diameter range 90-2400 km,

the radiometric technique provides sizes with accuracies of about 2-50% with a typical value of 10%. Similarly, geometric albedos have accuracies about 2-70% with a typical value of 20% (Lellouch et al., 2013). Thus, with respect to sizes determined by radiometry, stellar occultations can improve the size determination by two orders of magnitude.

# Chapter 2

# Characterization of cameras and time acquisition

As stated before, it is critical to have trusted fast cameras and reliable time registration in order to reconstruct the 2D shadow of distant bodies from stellar occultations.

The Lucky Star project considered the acquisition and deployment of several *occultation kits*, with each kit consisting of camera, time registration system, acquisition software and various optical and mechanical adapters.

In that context, this chapter describes my role in this project and the tests/validations that I performed in those kits.

The tests have as main goals:

• evaluate and validate the performances of alternative camera models under typical conditions,
• evaluate the accuracy of the time registration system,
• evaluate the adequacy of the acquisition software.

I performed tests in the laboratory and on the sky and involved interactions with the software manufacturer in order to solve flaws and to put in adequation the software and the needs of the project. The tests also consider the re-evaluation of kits already in use by the project(called here-on the "Merlin kit"), in particular, their time registration. Part of the data analyzed in this thesis was taken with several of those kits and the results of some tests were incorporated in the data analysis (see Chapter 3).

For portable cameras it is commonplace to use fast Charged Coupled Devices (CCD) which can reach fast readout rates of several images per second with dead times of fraction of a second (corresponding to readout and writing). In particular, Interlined CCDs reach dead times below the millisecond. Similarly, the lower prices of CMOS-based cameras make them attractive for these applications, having dead times comparable to those of CCDs.

However, the main disadvantages of CMOS against CCDs cameras are the smaller size of pixels and higher readout noises. Both effects combined can reduce the SNR obtained under equivalent conditions, as the stellar light is spread among a larger number of more noisy pixels. Nonetheless, current performances and prices make both alternatives comparable in terms of price versus performance, so that favoring one over the other is not a simple task.

Table 2.1: Camera features.

| KITE EM247 digital B/W camera. | | KI247-CL |
|---|---|---|
| Active pixel | 568×496 | 3096×2080 |
| Pixel size ($\mu m$) | 10x10 | 2.4×2.4 |
| Full Well Capacity ($e^-$) | 24000 | ... |
| Readout noise ($e^-$) | <1 (with $EM_{gain}$ ON) (a) | 1.4-2.2 |
| | <20 (with EM gain OFF) | ... |
| Dark Current ($e^-$/px/s) | <1 | ... |
| Digital Output Format (bit) | 16 | 14 |
| Interface | CameraLink | USB(2.0,3.0) |
| Peak Quantum Efficiency | 53% @ 530 nm | ... |
| Spectral response ($\nu m$) | 350 - 1100 | 400-1000 |
| Cooling | -20°C with ambient air @20°C | -40°C (b) |
| Binning | 1×1, 2×2, 3×3, 4×4 | 1×1, 2×2 |
| Trigger | Yes | No |
| Weight (g) | < 550 | 410 |

Note. — (a) $EM_{gain}$ is the Electro-multiplication factor which can be changed from the acquisition software. When no $EM_{gain}$ is applied, the camera behaves as a regular CCD. (b) Relative to ambient temperature.

After an initial round of evaluation (out of the scope of this work and not

described here), the decision of which camera to include in the kits was narrowed down to two alternatives. The first-one is the *Kite* camera, based on an Electro-multiplied CCD (EMCCD) from the Raptor Photonics company, and the ZWO ASI178MM-Cool camera, a CMOS-based from ZWOptical. The main differences between these two cameras are the smaller pixel size of the CMOS, the electro-multiplication and possibility of external trigger in the Kite, and the different interfaces between PC and camera (see Table 2.1). The electro-multiplication is an extra stage of amplification introduced in the camera before the signal is digitized. The main effect is to decrease the effective readout noise (RON). The electro multiplication factor can be changed from the acquisition software trough a '$\mathrm{EM_{gain}}$' parameter going from a minimum of 0 (the camera behaves as a regular CCD) to a maximum of 3500. The relation between the gain parameter and the electro-multiplication factor is derived below as well as the reduction of the readout noise as a function of the $\mathrm{EM_{gain}}$ applied.

With respect to the time registration, the Kite presents the advantage that each image acquisition can be triggered from an external signal.

Combined with an external device as the TimeBox (see below), it can provide an accurate time stamping for each image. However, the accuracy achieved with the CMOS camera is good enough for most applications and the lack of external trigger is not a limitation to achieve the scientific goals of the project (see Section 2.3).

## 2.1 Conversion factor and read-out noise

Both cameras were tested to determine the conversion factor $g$ and read-out noise (RON) for different configurations. The factor $g$ gives the conversion between the number of electrons $e^-$ recorded by the camera into digital counts, or Analog-Digital Units (ADUs), in the recorded image. The factor $g$ is expressed in electrons per ADU ($e^-$/ADU). This basic quantity is used below to express the RON in comparable units (i.e. $e^-$ ) so the performances of both cameras can be consistently compared. Knowing $g$, it is possible to estimate the SNR given a star magnitude, a telescope collecting area, and the sky brightness. In practice, several other conditions will determine the

final SNR achieved in a particular observation. Among these are the star altitude, the star color, the moon light background, linked to its phase and angular distance from the star, the seeing, telescope shaking by wind, to name some. However, it is useful to have some quantitative way to compare the expected performances of the cameras under typical conditions.

The conversion factor $g$ is calculated using the 'photon transfer curve' (PTC) (Janesick, 2001) which basic steps are summarized here. The camera is illuminated by a source of white light with constant and uniform intensity. A centered squared region of each image is used and the rest of the image is discarded. This is done to take only the region with the most uniform illumination, and to avoid the so-called 'amplifier glow' typically present in the borders of CMOS-based cameras. Images are taken with the acquisition software 'Genika Astro' by Airylab using different level of illumination, starting from no light (detector totally covered) and increasing the illumination level up to the saturation of the detector. This is repeated changing the parameters of interest in each camera such as $CMOS_{\text{gain}}$ (respectively $EM_{\text{gain}}$ for the EMCCD camera) and binning factor.The tests were performed at room temperature of $\sim$20 C, keeping the detector temperature constant with the camera cooling system activated.

With the images acquired, the average signal $S$ in units of ADU is calculated. Then, the same images with same level of illumination are taken in pairs and subtracted to each other, and from the difference-image the variance $\sigma^2_{\text{diff}}$ is calculated. Subtracting pairs of images eliminates the effect of pixel-to-pixel variations leaving only the photon noise. The variance in the original image is calculated as $\sigma^2 = \sigma^2_{\text{diff}}/2$ where it is assumed that noises add in quadrature. Then, from a plot of $\sigma^2$ vs $S$ the slope $m$ is obtained using a linear fit. From that, the conversion factor $g$ is:

$$g = \frac{1}{m}(e\ ADU^{-1}) \tag{2.1}$$

Given some differences in the cameras, the procedure and results for each are explained separately.

### 2.1.1 CMOS camera

The CMOS camera permits to change a gain factor ($CMOS_{\text{gain}}$) as well as a *gamma* factor. The $CMOS_{\text{gain}}$ have a direct impact in the amount of readout noise (see Table 2.2). On the other hand, the gamma factor introduces a non-linearity in the relation between the incident light and the signal in ADUs (see Figure 2.1). This is useful in some applications[1] but obviously unwanted in the case of stellar occultations, e.g. for analyzing tenuous atmospheres or diffraction effects by airless bodies and their rings. In that case, the retrieval of physical parameters of the body under study (e.g. atmospheric density profiles or ring optical depths) are directly linked to the linearity of the device.

#### Linearity

To determine the gamma factor for which the camera response is linear, $\sigma$ versus $S$ for different gamma factor is compared in a log-log plot. In images dominated by photons noise we have $\sigma^2 \propto S$, so the linear relation will be evidenced by a slope of 1/2 in a log-log plot.

The Figure 2.1 shows a plot of $\sigma^2$ versus $S$ for different gamma values, where is clearly seen that the linear behavior is obtained with gamma equal 50.

Adopting gamma=50 for the rest of the tests, a conversion factor $g = 0.228\ e^-/ADU$ is obtained from the $\sigma^2$ vs $S$ with no $CMOS_{\text{gain}}$ applied (see Figure 2.2).

Repeating the PTC for different $CMOS_{\text{gain}}$ it is found that the gain-factor g($CMOS_{\text{gain}}$) is logarithmic and given by

$$g(CMOS_{\text{gain}}) = g \times 10^{-CMOS_{\text{gain}}/200}. \tag{2.2}$$

#### Readout noise

Table 2.2 shows the RON as a function of the $CMOS_{\text{gain}}$ for different binning factors. The RON is in units of $e^-$ using the factors calculated above. The

[1]For instance, to increase the dynamical range if stars with largely different fluxes are present in the field of view.

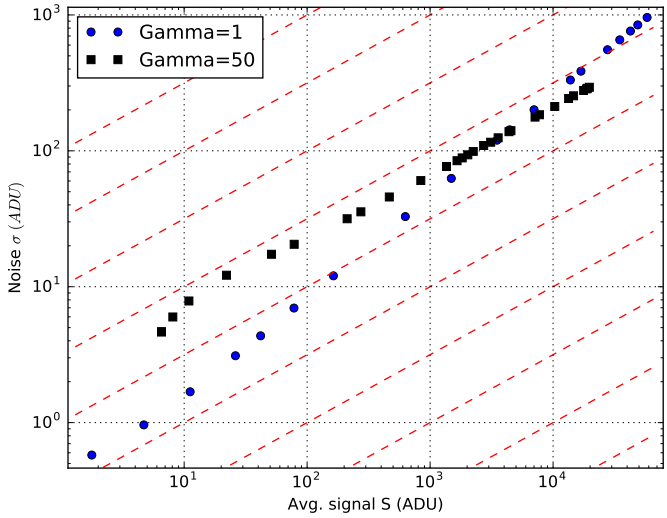


Figure 2.1: Log-log plot of Noise $\sigma$ versus average signal $S$ for the CMOS camera with two values of gamma. Points correspond to measurements at different levels of illumination in a 300×300 px sub-region and no $CMOS_{\text{gain}}$ applied. The blue points correspond to measurements with gamma=1 while black squares correspond to gamma=50. Red dashed lines have slopes of 1/2, corresponding to linear behavior under presence of photon noise. The camera is close to a linear photon-dominated regime with gamma=50 from signal levels >100 ADU. The blue dots clearly depart from the linear behavior as a consequence of the gamma factor.

readout noise change in a factor of $\sim$ 2 as a function of the $CMOS_{\text{gain}}$ and stay roughly constant for $CMOS_{\text{gain}} > 250$. The tests showed that the binned (2×2) pixel value (in ADUs) is the average of the four original pixels. This reduces the RON measured in ADUs by half but increase the RON in electrons by 2 Similarly, the RON roughly increases by a factor of 2 between binning 2x2 and 4x4. This is the expected behavior if the noise of the binned pixel is the addition, in quadrature, of the noise of the original unbinned pixel.

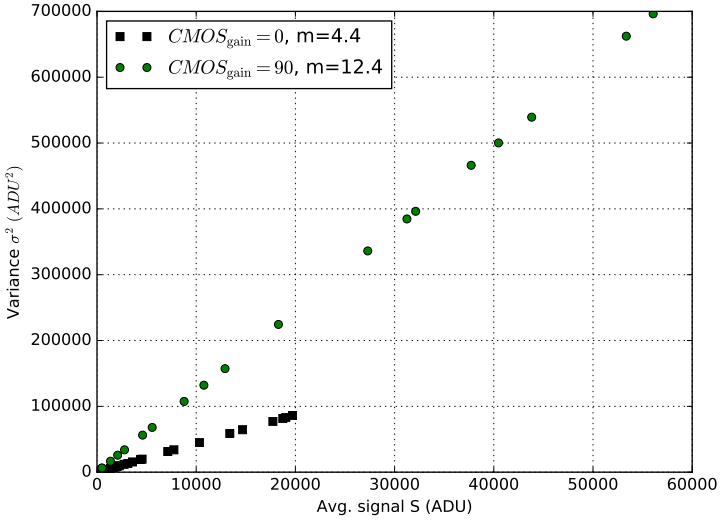


Figure 2.2: Signal variance $\sigma^2$ versus average signal $S$ for the CMOS camera. Black squares corresponds to no $CMOS_{\rm gain} = 0$ from where is determined a conversion factor $g = 0.228\ e^-/ADU$. Blue circles corresponds to $CMOS_{\rm gain} = 90$ from where is determined a conversion factor $g = 0.08\ e^-/ADU$ implying a logarithmic gain factor (see text).

Table 2.2: Readout noise for CMOS camera.

| $CMOS_{\rm gain}$ (units of 0.1 dB) | RON ($e^-$) Binning 1x1 | RON ($e^-$) Binning 2x2 | RON ($e^-$) Binning 4x4 |
|---|---|---|---|
| 0 | 1.996 | 5.63 | 11.704 |
| 50 | 1.768 | 4.532 | 9.278 |
| 100 | 1.598 | 3.927 | 7.914 |
| 150 | 1.474 | 3.445 | 6.958 |
| 200 | 1.357 | 3.082 | 6.473 |
| 250 | 1.296 | 2.853 | 5.733 |
| 300 | 1.270 | 2.832 | 5.745 |
| 350 | 1.297 | 2.859 | 5.681 |
| 400 | 1.284 | 2.800 | 5.574 |
| 450 | 1.266 | 2.791 | 5.522 |
| 500 | 1.226 | 2.555 | 3.778 |
| 510 | 1.226 | 2.424 | 3.348 |

Note. — Readout noise RON as a function of camera gain and binning. Exposure time is 0.5 s. The RON decreases by a factor of ∼2 between minimum and maximum $CMOS_{\rm gain}$, while it increases by a factor of ∼2 between binning 1x1 and 2x2 (correspondingly between binning 2x2 and 4x4).

### 2.1.2 EMCCD camera

The EMCCD Kite camera possesses an Electro-multiplication stage that multiplies the collected charge in each pixel before the signal is digitized. When no electro-multiplication is applied, the Kite behaves as a regular CCD, so that the conversion factor $g$ is obtained from the PTC as explained before. With the electro-multiplication applied, the slope $m$ of the PTC gives the electro-multiplication factor g($EM_{\text{gain}}$).

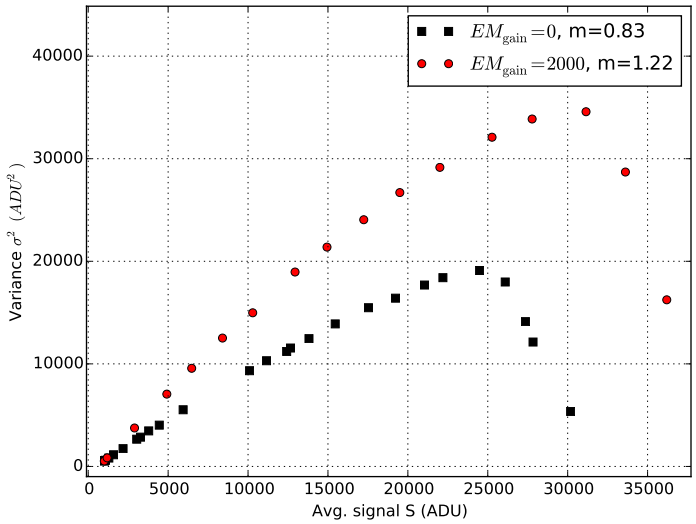


Figure 2.3: Signal variance $\sigma^2$ versus average signal $S$ for the EMCCD camera Kite. Black squares correspond to a value $EM_{\text{gain}} = 1$ set by the manufacturer (corresponding in fact to no gain) from which I derive a conversion factor $g = 1.2\ e^-/ADU$. Blue circles corresponds to $EM_{\text{gain}} = 2000$ from which I derive a conversion factor $g = 0.82\ e^-/ADU$ and an electro-multiplication factor of 1.5.

A conversion factor $g = 1.2\ e^-/ADU$ is obtained from the $\sigma^2$ vs $S$ with no $EM_{\text{gain}}$ applied (see Figure 2.3). The Table 2.3 shows the results for the Kite camera for different $EM_{\text{gain}}$ and binning factor 1×1 and 2×2. These values are in turn used to evaluate the RON of the camera under different configurations.

**Readout noise**

The readout noise is obtained, as before, measuring the noise in images with the shortest exposure time possible and with no illumination. The Table 2.4 summarizes the results of the tests. The RON have a larger range (of $\sim 20$ times) than for the CMOS camera and it is highly dependent on the electro-multiplication applied, exhibiting a strong decrease for larger values of the $\mathrm{EM_{gain}}$. It must be noticed that the relation between the $\mathrm{EM_{gain}}$ adjusted in the acquisition software and the effective electro-multiplication factor applied in the detector is, in principle, dependent of operational conditions (from private communication with the manufacturer). Nonetheless, no significant differences were detected among the tests performed in different test sessions and the results given here are representatives of the performance under normal circumstances.

Table 2.3: Conversion factor for the Kite camera.

| Signal range (ADU) | Range used to estimate 'g' (ADU) | $EM_{\text{gain}}$ (unit-less) | g($EM_{\text{gain}}$) e/ADU |
|---|---|---|---|
| Binning 1x1 | | | |
| 1016-30186 | 3274-19229 | 0 | 1.15 |
| 1008-33655 | 3446-20179 | 500 | 1.15 |
| 1056-33823 | 2037-19968 | 1000 | 1.12 |
| 1006-41211 | 2897-27776 | 2000 | 0.82 |
| 1146-20106 | 1995-18047 | 2500 | 0.27 |
| 2249-57610 | 2936-22013 | 3000 | 0.03777 |
| 1116-59323 | 3263-23760 | 3100 | 0.01816 |
| 1227-56234 | 3997-23485 | 3200 | 0.00873 |
| 1993-53949 | 4246-22897 | 3300 | 0.00352 |
| 9360-62709 | 9360-24139 | 3400 | 0.00143 |
| 6173-61877 | 6173-25780 | 3500 | 0.00043 |
| Binning 2x2 | | | |
| 4005-54469 | 7977-43094 | 0 | 1.21 |
| 4085-54491 | 5681-42969 | 500 | 1.22 |
| 3905-52890 | 3905-46361 | 1000 | 1.19 |
| 2797-56571 | 5043-31327 | 2000 | 0.3 |
| 2797-56571 | 5043-25478 | 2500 | 0.286 |
| 2803-58608 | 4424-31443 | 3000 | 0.038 |
| 2248-59929 | 6513-31113 | 3100 | 0.02 |
| 2273-61696 | 5325-22366 | 3300 | 0.00320 |
| 5180-53735 | 7769-32382 | 3500 | 0.00046 |

Note. — Conversion factor $g$ in $e^-$/ADU for the Kite EMCCD camera at different $EM_{\text{gain}}$ values and binning factors. The second column indicate the range of illumination in ADUs used to estimate $g$ (see also figure 2.3). It is seen that the variation of $g$ with $EM_{\text{gain}}$ is stronger at high electro-multiplication gains. $EM_{\text{gain}}$ is a unit-less value adjusted at the high-level software. The real EM factor can be obtained as the ratio between g at a given $EM_{\text{gain}}$ and the $EM_{\text{gain}}$ with no Electro-multiplication applied: 1.15 for binning 1x1 and 1.21 for binning 2x2.

Table 2.4: Readout noise for the EMCCD Kite camera.

| Binning | 1x1 | | | | 2x2 | | | | | |
|---|---|---|---|---|---|---|---|---|---|---|
| Exp. time (s) | 0.5 | | 1.0 | | 0.1 | | 0.5 | | 1.0 | |
| $EM_{\text{gain}}$ | RON (ADU) | RON (e) | RON (ADU) | RON (e) | RON (ADU) | RON (e) | RON (ADU) | RON (e) | RON (ADU) | RON (e) |
| 0 | 23.4 | 27.0 | 23.5 | 27.0 | 44 | 51 | 44.6 | 54 | 45 | 54 |
| 500 | 22.9 | 26.3 | 23.2 | 26.7 | 40 | 46 | 44.1 | 54 | 44 | 51 |
| 1000 | 23.3 | 26.2 | 23.5 | 26.3 | 60 | 67 | 59.3 | 71 | 59 | 66 |
| 1500 | 23.0 | 25.0 | 23.2 | 25.2 | 60 | 65 | 59.5 | 43 | 60 | 65 |
| 2000 | 23.7 | 19.5 | 23.3 | 19.1 | 61 | 50 | 60.8 | 18 | 60 | 49 |
| 2500 | 23.8 | 6.4 | 23.2 | 6.3 | 61 | 16 | 60.0 | 17 | 60 | 16 |
| 2600 | 23.2 | 4.5 | 24.5 | 4.7 | 61 | 12 | 60.8 | 15 | 61 | 12 |
| 2700 | 23.0 | 3.1 | 24.5 | 3.3 | 61 | 8.3 | 60.7 | 12 | 61 | 8.2 |
| 2800 | 24.2 | 2.3 | 24.3 | 2.3 | 62 | 5.8 | 60.5 | 8.1 | 62 | 5.8 |
| 2900 | 26.0 | 1.6 | 36.1 | 2.3 | 63 | 3.9 | 63.1 | 4.9 | 63 | 3.9 |
| 3000 | 30.3 | 1.1 | – | – | 67 | 2.5 | 66.9 | 2.5 | 69 | 2.6 |
| 3100 | 45.2 | 0.8 | 221.4 | 4.0 | 81 | 1.5 | 83.4 | 1.7 | 85 | 1.5 |
| 3200 | 87.8 | 0.8 | 225.5 | 2.0 | 135 | 1.2 | 137 | 1.4 | 144 | 1.3 |
| 3300 | 209.1 | 0.8 | 219.5 | 0.8 | 293 | 1.0 | 315 | 1.0 | 312 | 1.1 |
| 3400 | 569.8 | 0.8 | 3874.3 | 5.5 | 805 | 1.2 | 824 | - | 845 | 1.2 |
| 3500 | 1850.8 | 0.8 | 3954.5 | 1.7 | 2609 | 1.1 | 2747 | 1.3 | 2821 | 1.2 |

## 2.2 Dead times

### 2.2.1 CMOS camera

The dead time is derived from the time stamp in consecutive exposures and the exposure time. The dead time measured in the CMOS camera shows some jitter (see Figure 2.4), while in average it is negligible and it stays below the millisecond level (see Table 2.5).

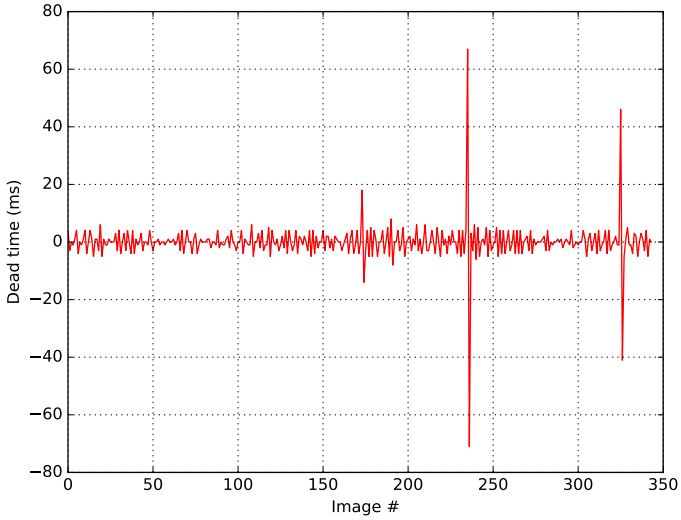


Figure 2.4: Dead time in the CMOS camera with exposure time of 290 ms. Dead time present some jitter for the CMOS camera but, in average, it remains negligible below the millisecond.

Table 2.5: Dead time for the CMOS camera.

| Exposure time (ms) | Dead time (ms) | Frame size px |
|---|---|---|
| 45 | 0±5 | 3096x2080 (Full frame) |
| 191 | 0±3 | Full frame |
| 291 | 0±7 | Full frame |
| 491 | 0±1 | Full frame |

### 2.2.2 Kite camera

The Table 2.6 shows the measurements of the dead time for the Kite camera derived as explained above. For full-frame images, the dead time is consistently ∼18 milliseconds. This is higher than for the CMOS camera but it is still negligible for the typical exposure times used in stellar occultations. In practice, and using a small telescope (in the range 25-50 cm diameter), the exposure time rarely goes below 100 ms, so that a 18 ms dead-time ensures that more than 80% of the photons are eventually collected. However, this time must be taken into account when the Kite camera is used with an external source of trigger to avoid the lost of frames (see Section 2.3).

Table 2.6: Dead time for the Kite camera.

| $t_{exp}$ (s) | Dead time (ms) | Frame size (px) |
|---|---|---|
| 0.045 | 18+-1 | 658x496 (full frame) |
| 0.045 | 7 +- 0.5 | 208x160 ( 1/9 frame) |
| 0.199 | 18+-1 | full frame |
| 0.299 | 18+-0.5 | full frame |
| 0.399 | 18+-0.5 | full frame |
| 0.993 | 18+-1 | full frame |

## 2.3 Accuracy of time registration

The time registration system under test consists of a *TimeBox* obtaining the UTC time from a GPS signal. It provides two basic modes of functioning, the first, so called 'computer mode', allows to synchronize the operative system (Windows) with the UTC in a regular basis, while the second, so called 'trigger mode', provide a periodic signal that can be used to trigger an image acquisition (only used with the Kite camera). Tests for the Kite+TimeBox and CMOS+TimeBox were done only with the computer mode.

The Merlin kits (that have been used in the previous year by the Paris occultation group) were also tested. This kit bases the time registration in a GPS antenna with a Pulse Per Second signal (PPS). The PPS is an accurate signal that repeats once per second with a fixed width in time and with sharp rising and falling edges. Then, a software application keeps a log with the operative system time against the UTC time from the GPS, which is used in turn to calibrate the timestamp of the images acquired during an occultation.

The three systems, Merlin+GPS, KITE+TimeBox and CMOS+TimeBox were tested to derive the time accuracy respect to an external comparison signal. The comparison signal used was a visible PPS with a constant width of 20 ms obtained from an independent GPS. The procedure consisted in taking images of a luminous signal taken directly from the PPS. Then, the difference between the time registered in the images and the UTC (given by the GPS) is obtained comparing the rise and falling instants of the PPS signal with the time-stamp of the images. The accuracy of this difference is limited by the duration of the PPS pulse and only departures from UTC greater than 20 ms can be detected, which is enough for the scope of the test.

As the PPS only provides the start of the current second, a luminous signal was connected to a DCF77 radio signal[2], and captured in each image This was used in order to identify the current UTC minute and to detect eventual larger departures from UTC.

[2] DCF77 is a longwave radio signal from Mainflingen in Germany, under the initiative of the Physikalisch-Technische Bundesanstalt, and providing an accurate timestamp synchronized with UTC.

Table 2.7 shows that the departures from UTC stay below ∼20 ms for all the tested kits. For a nominal shadow velocity of 20 km $s^{-1}$, this corresponds to 400 m in the shadow plane. This is currently unimportant, but may become significant if small scale effects are searched for, like distortions of Chariklo's rings due to normal oscillation modes, or a fine search for topographic features at the surface of some bodies.

A by-product of these tests was the detection of a one-image delay in the timestamp of the images acquired with the Merlin kits. That is, the timestamp registered with each image corresponds to the end of the exposure of the previously acquired image. This delay was unacknowledged in previous analysis introducing a systematic offset of one exposure time. This translates in a systematic error of several kilometers in the plane of the sky at the distance of the occulting object.

Table 2.7: Time difference respect to UTC.

| Exposure time (ms) | $\Delta t$ (ms) |
|---|---|
| CMOS+TimeBox | |
| 191 | 14±10 |
| 409 | 15±10 |
| Kite+TimeBox | |
| 45 | 15±7 |
| 199 | 12±24 |
| 299 | 17±35 |
| Merlin+GPS | |
| 41 | 15±7 |
| 190 | 5±10 |
| 490 | 12±10 |
| 950 | 18±15 |
| 1010 | 9±10 |

## 2.4 Test at the sky and SNR estimation

Both cameras were tested at the sky to assess the performances at typical conditions. To do so, images were taken with medium size telescopes (at Pic du Midi), covering an area of the sky with stars spanning a large range in magnitudes. Then, aperture photometry was performed in the images to obtain the throughput of the system and to measure the SNR as a function of star magnitude. The fluxes in ADUs were converted into $e^-$ using the conversion factors determined before (see Section 2.1). As the relative spectral response of both cameras and the Gaia G bandpass are similar (see Figure 2.5), the Gaia G-magnitudes were used to obtain the star fluxes as a function of their G-magnitudes.

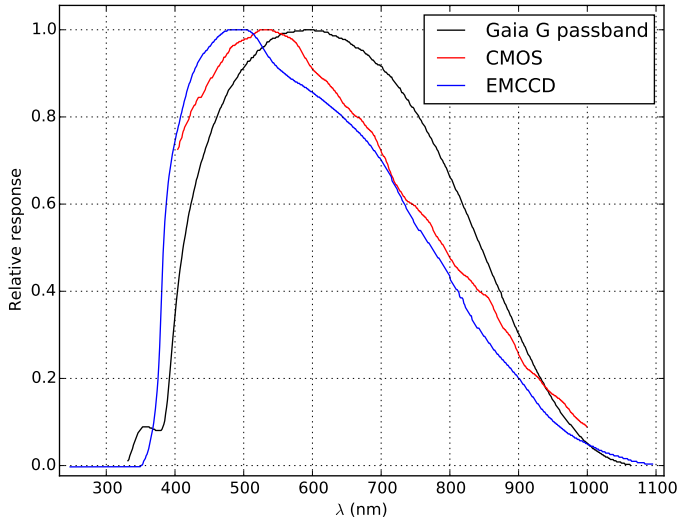


Figure 2.5: Spectral response of the Kite and CMOS cameras compared to the Gaia G bandpass. Given the similitudes, the G band star fluxes are used to estimate the SNR. The curves are normalized to the maximum value.

When both cameras are used at the minimum readout noise configurations, the Kite camera performances slightly surpass the CMOS camera. In the faint end, when the noise is dominated by readout noise, the detection limit is $\sim$ one magnitude fainter for the Kite respect to the CMOS camera. The increase of one magnitude roughly increase the number of observable stars by a factor of 2-3. So, under same conditions, with the Kite we are

able to observe 2-3 times more occultations than with the CMOS, which coincidentally is roughly speaking the total price ratio between the two kits: about 9000 euros for the former, and 2500 euros for the latter.

The figure 2.6 shows the SNR obtained from the tests at the sky compared with the expected SNR. As the tests were not in photometric conditions, the results of this figure must be understood in relative instead of absolute terms.

In summary, the tests that I have described here shows that the Kite camera should be used for faint stars that are observed under good conditions. In effect, the main limitation during an observation is often the sky quality, in particular the background sky level due to either twilight or Moon light. The seeing (not talking about cloud passages) is also an important constraint. Independently of photon and read noise, it degrades the signal, especially for small portable telescopes for which the location is imposed by the shadow path, and not by the quality of the observing site.

In a framework where the date, observing location and magnitude of the star are imposed by the event, the moto is “be at the right place and the right moment". So, it is important to be able to deploy several stations in order the reconstruct the 2D structure of the body under study.

In that context, my tests resulting in buying in the frame of the Lucky Star project two Kite kits and five cheaper Cmos kits. With the six already existing Merlin kits, this provides a good balance between state of the art cameras, and less performing ones, that are still important for dispatching as numerous as possible stations in the shadow paths.

My tests also allow other teams (in particular in the amateur community) to make their choice in a context where misleading numbers given by manufacturers sometimes overestimates the performances of a given equipment. Also, my protocol concerning the accuracy of time registration may be used as a guide line for other teams. This is a point of paramount important, as wrong timing mean wrong scientific conclusions, once various simultaneous observations of a given even are put together.

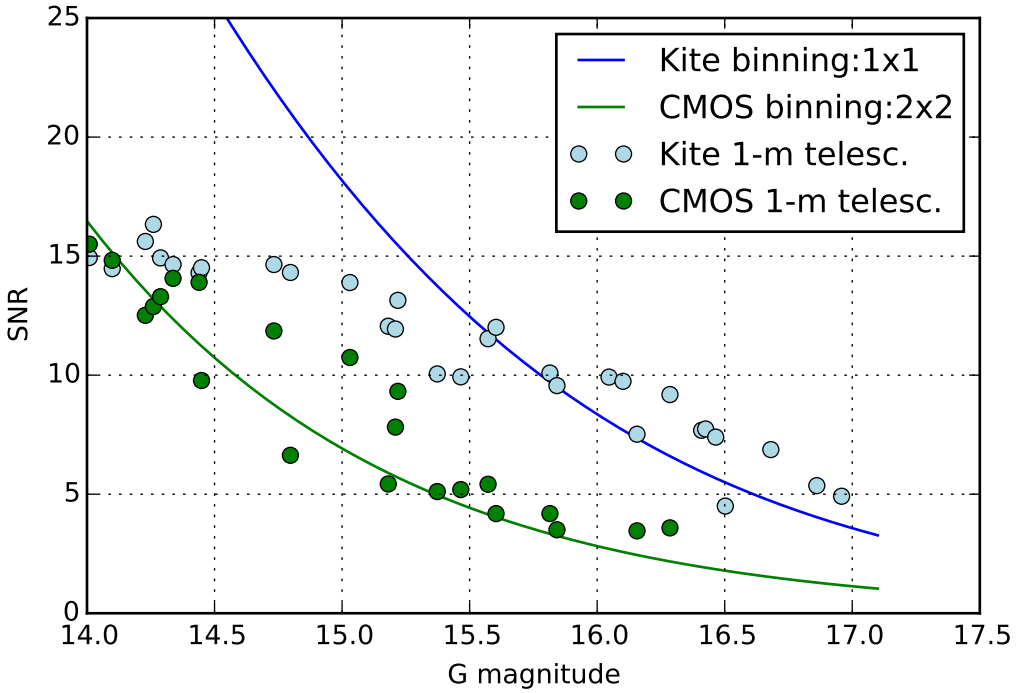


Figure 2.6: SNR measurement with the CMOS and Kite cameras at Pic du Midi 1-m telescope. Blue dots and green dots are the SNR measured in images taken with exposure times of 0.5 s. Blue and green lines are the expected SNR for each camera. The departure of the expected behavior for brighter stars for the Kite camera is evidence of saturation.

# Chapter 3

# Physical characterization by stellar occultations

Here I address the problem of the physical characterization of outer Solar System objects using stellar occultations. The chapter concentrates in the analysis of stellar occultations by the Centaur object Chariklo observed between 2013 and 2016 to provide constrains in its size, shape and density. I also include the analysis of stellar occultations by the TNO (229762) 2007 $UK_{126}$ providing constrains in its density and the plutino object (208996) 2003 $AZ_{84}$ providing constrains in its size, shape and density. Section 3.1 summarizes my work in those two cases whose results were published in (Benedetti-Rossi et al., 2016; Dias-Oliveira et al., 2017) (now-on referred as BR16 and DO17 respectively). Section 3.2.3 presents the approach used to analyze the occultation by Chariklo whose main results will be submitted for publication. The corresponding draft is included at the end of the chapter.

This chapter illustrates the different scenarios commented in the Introduction. For 2007 $UK_{126}$ and 2003 $AZ_{84}$ the procedure to analyze the occultation chords consisted in to fit elliptical limb profiles to one and two stellar occultations respectively. From there, and under some simplifications, constraints in the size, shape and density of the objects are derived. Instead, the five stellar occultations by Chariklo consist in single and double occultation chords, making the fit of elliptical limbs impractical, not to mention that the single-chord occultations would be of no use in this classical approach.

In this scenario, in the analysis of Chariklo's occultations I adopt a Bayesian approach to derive probability density functions (pdf) for the parameters of ellipsoidal models (triaxial ellipsoids, spheroid and sphere). The pdf's are evaluated using a Markov Chain Monte Carlo algorithm to draw samples from those distributions, in order to derive the most probable parameter values with their respective uncertainties. The presence of rings around Chariklo, the long term evolution of Chariklo's brightness, the evolution of amplitude of its rotational light curve and physical considerations (the stability of bodies in hydrostatic equilibrium) are all used as a priori information in the framework of Bayesian inference of the model parameters.

## 3.1 2007 $UK_{126}$ and 2003 $AZ_{84}$

### 3.1.1 Stellar occultation by 2007 $UK_{126}$

The TNO (229762) 2007 $UK_{126}$ is a scattered disc object (SDO) with a semi major axis of 73.8 au, orbital eccentricity of 0.492, orbital period of 634.13 yr, and an inclination of 23.34°. It possess a satellite but its orbit is not well determined to provide a mass value for the system (Santos-Sanz et al., 2012).

An occultation by this TNO was observed from North-America in 2014 November 15. There were seven positive detection and two negatives chords providing a well constrained elliptical fit. This is a good example of the most usual case where there is only one multi-chord occultation of an object. Given the size of the object of about 680 km, the reasonable assumption of a body in hydrostatic equilibrium was adopted (Tancredi & Favre, 2008). For an homogeneous body in hydrostatic equilibrium, the shape can be a Maclaurin spheroid or a Jacobi ellipsoid. In this case, with only one occultation observed, only the Maclaurin possibility was analyzed.

As there was no extra information of the pole position of the object, the object is assumed randomly orientated. Nonetheless, given the good constraint given by occultations chords (see Figure 3 and Table 4 in BR16), I adopted the simplification that the position angle of the pole axis was fixed and hence given by position angle of the semi minor axis of the elliptical fit. With the apparent center of the ellipse constrained by the elliptical fit, the remaining free parameter is the polar aspect angle $\xi$ (the angle between the polar axis and the line of sight). Then the approach is to use the apparent oblateness $\epsilon'$ to constrain the tridimensional shape and size under the assumption of an Maclaurin spheroid.

As stated in BR16, the apparent oblateness $\epsilon' = 1 - (b'/a')$ and true oblateness $\epsilon = 1 - (c/a)$ for an spheroid are related by:

$$\epsilon' = 1 - \sqrt{\cos^2(\xi) + (1-\epsilon)^2 \sin^2(\xi)}, \tag{3.1}$$

where $b'$ is the apparent semi-minor axis, $a = a'$ is the true equatorial radius, and $c$ is the real polar radius. A Maclaurin spheroid is stable for

$0 < \Omega < 0.374$, where

$$\Omega = \frac{\omega^2}{\pi G \rho} = \frac{2\sqrt{1-e^2}}{e^3}\left[\left(3-2e^2\right)\arcsin e - 3e\sqrt{1-e^2}\right], \qquad (3.2)$$

where $e^2 = 1-(c/a)^2$, G is the gravitational constant, $\omega = 2\pi/T$ (T being the rotation period of the body), and $\rho$ the (uniform) density. For a given rotation period, the lower limit $\Omega = 0$ corresponds to the spherical limit with $\rho \to \infty$, while the upper limit correspond to a body with the maximum oblateness and the minimum density. The stability condition provides a range of possible density for a given rotation period, which derives in a range of possible values for $e$, $\epsilon'$ and finally for $\xi$ with the Equations 3.1 and 3.2.

The approach is to estimate, inside this range in density, the probability distribution, $\Pr(\rho)$. This was performed numerically, assuming that the polar aspect angle $\xi$ is a random variable uniformly distributed in the interval determined by the stability conditions of the Maclaurin spheroid.

The rotation period of 2007 $UK_{126}$ is not well known, and the nominal and most probable rotation period is 11.05 hr, while the lowest possible value is $\sim 8$ hr. In the first case, the density lies in the range [320, 1740] kg m$^{-3}$, while for $T = 8$ hr the density lies in the range [600, 3300] kg m$^{-3}$. With no further constraints, it is found that the most probable values for the density are close to the upper limit of the respective density range (see Figure 3 in BR16).

In conclusion, this constitutes the first multi-chord stellar occultation by 2007 $UK_{126}$. Given the good coverage of the occultation shadow path, it provides a good fit to a elliptical fit from where an upper limit and most probable range of densities is derived. Other shapes are not explored given the lack of constraints in the orientation of the body.

### 3.1.2 Stellar occultation by 2003 $AZ_{84}$

The TNO 2003 $AZ_{84}$ is a large member of the plutinos, objects in 2:3 mean motion resonance with Neptune. It has an orbit with a semi major axis of 39.4 au, orbital eccentricity of 0.179, orbital period of 247.37 yr, and an inclination of 13.6°. It has a companion with an unknown orbit and hence no mass estimate has been derived for the system An equivalent radius of the main body $R = 364 \pm 30$ was derived from thermal measurements (Mommert et al., 2012).

2003 $AZ_{84}$ was observed with four stellar occultations between 2011 and 2014. Two of those were single-chord while the occultations of 2012 February 3 and 2014 November 15 were multi-chord. Elliptical fits to both multi-chord occultations gave substantially different projected oblateness of 0.340 and 0.054 for 2012 and 2014 respectively and a change in the orientation of the projected limb between those dates (see Table 5 in DO17 for details of the elliptical fits). This suggested that the body is elongated and the change in the apparent shape is product of change of aspect as observed from Earth.

The observations were separated in time by almost three years, so the first step was analyze the effect of the possible change in orientation respect to the Earth between 2012 and 2014. As the pole position is unknown, this was considered randomly oriented in the celestial sphere. The probability distribution of the planetocentric latitude of the Earth $B$ and the position angle of the pole axis $P$ was calculated for the dates of the occultations in 2012 and 2014. From this, it was determined that the change in $|B|$ is less than $\sim 5°$, while the change in $P$ is typically $\sim 7°$.

With this result, we simplify the problem assuming that the pole axis of the object has the same orientation in 2012 and 2014. In consequence, the change in apparent shape is attributed entirely to the rotation of an elongated the body. Given the size the critical diameter necessary to reach equilibrium for an icy body is in the range 200-900 km (Tancredi & Favre, 2008), a body of this size with homogeneous density can assume a Jacobi ellipsoid shape (Chandrasekhar, 1987).

The approach I adopted to constrain the size and shape of the object was to explore a grid of values for the size and shape (parametrized by the

semi-major axis $a$ and the object density $\rho$), and its orientation relative to the Earth given by the angles $B$, $P$ and rotation angle $\phi$. The rotation angle origin, $\phi = 0$, is arbitrarily defined when the longer axis (the prime meridian) of the ellipsoid points towards the observer and is counted positively following the right-hand rule around the pole axis. The apparent size, shape, and orientation of the projected ellipse are then computed and compared with the ones determined with the elliptical fits (see Table 5 in DO17). The Figure 8 in DO17 shows the region of $B$ vs $\rho$ compatible with the elliptical fits. It is found that $|B|$ is constrained between $\sim 25^\circ$ and $\sim 55^\circ$ while the object density is constrained between $\sim$870 kg m$^{-3}$ and 1000 kg m$^{-3}$. The amplitudes of the rotational light curve $\Delta m$ provided further constraints in the orientation and density (and hence shape) for the body, restricting the density to a narrow region around $\sim$870 kg m$^{-3}$ and opening angle $B \sim 48^\circ$.

This case exemplifies how occultations by the same object, separated by several months, can be combined to constrain its size and shape. The simplification assumed here can be adopted in general for other distant objects in the transneptunian region. In those cases, the change of object aspect is dominated by the Earth orbital motion in relatively short period of times (from months to a few years). It must be noticed that, while constraints in orientation and shape are found, no information is derived about the most probable values for those parameters. For that purpose, a more general approach can be used, as devised in the next Section, and applied to the analysis of stellar occultations by Chariklo.

## 3.2 Size and shape from multi-epoch stellar occultations

In this section I describe the determination of size, shape and size of topographic features derived from several stellar occultations by Chariklo between 2013 and 2016. For the analysis I adopt a Bayesian statistical approach which involves the computation of the probability distribution function (pdf) of the model parameters $\theta$ given the occultation data $D$. To compute the pdf, I adopt the use of a Markov chain Monte Carlo (MCMC) algorithm. With that I draw samples of the pdf from where I derive the most probable values for the parameters. The main results are included in a publication, whose draft is attached at the end of the present chapter.

### 3.2.1 Body models

Unlike the case of 2007 $UK_{126}$ and 2003 $AZ_{84}$ summarized above, here I do not make use of elliptical fits to the occultation chords. The occultations analyzed here consist of single chords and double chords only. This gives poor or no constraint at all in the size and orientation of the elliptical fits, making this approach impractical. Instead, the occultation chords are compared directly with the projected limb of a tridimensional model for the body.

For the body shapes I adopt ellipsoids with semi-axes $a > b > c$ rotating about the shorter axis. Among these ellipsoidal shapes, I consider the particular case of a spherical body with radius $R$ and the case of an homogeneous body in hydrostatic equilibrium. Under the last assumption, the body assumes the shape of either a Maclaurin spheroid or a Jacobi triaxial ellipsoid.

The parameters that define a triaxial ellipsoid in the plane of the sky are: the semi-axes $a$, $b$ and $c$, the center of the ellipsoid projected in the plane of the sky $(f_c, g_c)$, the position angle of the pole axis $P$ counted positively from the celestial north toward the east, the planetocentric latitude of the Earth $B$, the rotation angle $\phi$ counted positively from the central meridian in the sense of rotation of the body, and the sidereal rotation period $T$.

In practice, for some models the number of parameters is reduced. For

instance, for a Jacobi ellipsoid $a$, $b$ and $c$ are related to the rotation period $T$ and the (uniform) density $\rho$ by (Chandrasekhar, 1987):

$$\Omega = \frac{\omega^2}{\pi G\rho} = 2abc\int_0^\infty \frac{u}{(a^2+u)\,(b^2+u)\,\Delta}du \tag{3.3}$$
$$a^2b^2\int_0^\infty \frac{du}{(a^2+u)\,(b^2+u)} = c^2\int_0^\infty \frac{du}{(c^2+u)\,\Delta}$$
$$\Delta = \sqrt{(a^2+u)\,(b^2+u)\,(c^2+u)},$$

where $\omega = 2\pi/T$ ($T$ being the rotation period of the body) and $G$ is the gravitational constant. In this case I choose as parameters, the semi-major axis $a$, the density $\rho$ and the rotation period $T$ from where $b$ and $c$ is derived using Equation 3.3.

For the spheroidal solution we have $a = b$ ( the equatorial radius), and the rotation angle has no effect in the projected shape. For a Maclaurin spheroid, I use as parameters $a$, the rotation period $T$, and the (uniform) density $\rho$. From those, the polar semi-axis $c$ is derived using Equation 3.2.

Finally, for the spherical model the number of parameters are further reduced as the radius $R = a = b = c$, while the rotation period $T$ and the orientation angles $P$, $B$ and $\phi$ have no effect in the projected shape.

For each model considered, the projected shape in the plane of the sky are ellipses with semi-major axis $a_p$, semi-minor axis $b_p$, position angle of the semi-major axis $P_a$ (counted positively from celestial North toward celestial East), and center of the ellipse $(f_c, g_c)$. These ellipses are compared with the occultation chords extremities with coordinates (f,g) measured in the plane of the sky at the distance of the object. The pairs $(f, g)$ are the positions of the occulted star (at ingress and egress) respect to the expected position of Chariklo, as seen from the different stations. The coordinate $g$ is counted positively (in km) toward the celestial north, while $f$ is counted positively (in km) toward the celestial east.

As detailed in RL17, strong constraints in the apparent center of Chariklo $(f_c, g_c)$, and the angles $P$ and $B$ are given by the ring orientation, which has been deduced from thirteen stellar occultations by Chariklo's rings (see Table 5 in RL17 and (Bérard et al., 2017)).

### 3.2.2 Bayesian approach

For each model considered (a sphere, a generic triaxial ellipsoid, a Maclaurin spheroid and Jacobi ellipsoid), we are interested in to obtain the most probable values for the model parameters $\theta$ given the data $D$ As well, we want to quantify the uncertainty of those parameters, and to take into account the previous knowledge that we have about the parameters (so-called the 'priors' in Bayesian inference) .

Has explained in RL17, we define the "posterior" probability density $p(\theta|D)$ given by:

$$p(\theta|D) \propto \mathcal{L} \times p(\theta), \tag{3.4}$$

where $\mathcal{L}$ is the likelihood function, and $p(\theta)$ is the so-called "prior" distribution.

The likelihood $\mathcal{L}$ determines the probability to obtain the data $D$ given the physical model (ellipsoid, sphere, etc), and a model of the data uncertainties. On the other hand, the prior distribution $p(\theta)$ condense the previous knowledge we have about the parameters.

We adopt the likelihood $\mathcal{L}$ given by (see for example Equation 4.52 of Gregory, 2005)

$$\mathcal{L} = (2\pi)^{-N/2} \left\{ \prod_{i=1}^{N} \left(\sigma_{ri}^2 + \sigma_m^2\right)^{-\frac{1}{2}} \right\} \exp\left\{ -\sum_{i=1}^{N} \frac{\left(y_i - m\left(x_i \mid \theta\right)\right)^2)}{2\left(\sigma_{ri}^2 + \sigma_m^2\right)} \right\}, \tag{3.5}$$

where $N$ is the number of data points $y_i = (f_i, g_i)$, corresponding to the extremities of each occultation chord by the main body, $x_i$ represent the independent variable (the site and time of each occultation), $\sigma_{ri}$ are the uncertainties on the chord extremities $\sigma_{ch}$ projected along the radial direction counted from the center $(f_c, g_c)$ of the body (see Table 5 in RL17), $\theta$ is the vector representing the parameters of the model that describes the object, and $m\left(x_i \mid \theta\right)$ is the position of the chord extremity predicted by the model.

Notice that we introduced the parameter $\sigma_m$ to account for unmodeled topographic features on an otherwise smooth ellipsoidal model for the body. Due to this topography, the departure from the limb measured in the radial direction, is a normally distributed random variable with median zero and standard deviation $\sigma_m$ and independent from the measurements. Thus, $\sigma_m$

is estimated from the data and counted as an extra parameter for each physical model.

#### MCMC algorithm

As explained before, we are interested in to obtain the posterior pdf $p(\theta|Y)$ from were to derive the most probably parameter values and their uncertainties.

To do this, an approach is to draw samples from the posterior pdf $p(\theta|Y)$. From those samples we estimate the marginal distribution building histograms of the samples.

To generate the samples from $p(\theta|Y)$ I use a Markov Chain Monte Carlo (MCMC) algorithm. MCMC is a class of algorithms used to draw samples from a pdf using a Markov chain whose equilibrium distribution $\pi$ is the target pdf ($p(\theta|Y)$ in our case).

In this section I give a brief summary of the key concepts behind the MCMC methods in general as well as an explanation of the MCMC algorithm used in this work, in particular.

#### Markov chain

A key concept in MCMC methods are Markov chains and we give here some properties. A Markov chain is a sequence of random variables $\{X_t\} = X(1)$, ..., $X(t)$ where the state $x(t+1)$ has a probability distribution that depends only on the current state $x(t)$. This can be written

$$Prob(X(t+1) = x|X(1) = x_1, ..., X(t) = x_t) = Prob(X(t+1) = x|X(t) = x_t), \tag{3.6}$$

which means that a Markov chain is memoryless. In a time-homogeneous Markov chain, the probability of transition between two states $i$ and $j$ is independent of time $t$. In this case the chain can be defined by the probabilities of transition from one state to the other $p_{ij}$, and the chain has a stationary distribution $\pi$ which does not depend of time.

In a MCMC algorithm, a Markov chain must have some properties. The condition of detailed balance, given by

$$Prob(X(t), X(t+1)) = Prob(X(t+1), X(t)), \tag{3.7}$$

expresses that a chain having a stationary distribution is reversible and it looks the same when run forward or backward in time. This is an important condition as it guarantees the existence of a stationary distribution $\pi$. Another desirable property is that the convergence toward the stationary distribution do not depend of the initial position of the chain.

In general, a MCMC algorithm perform random walks to explore the parameter space. After each step of the random walk, the Markov chain acquires a new 'state'. Each state is no more that a position in the parameter space, that is, a vector with N dimensions, where N is the number of parameter of the model as detailed before. The goal is that the probability distribution $\pi$ of being in a particular position at any step $t$ must converge to the target pdf. If that is the case, after some number of steps we will obtain a set of independent samples from the probability density function $p(\theta|Y)$.

#### The 'stretch move' algorithm

The practical implementation to calculate the likelihood function and the priors is done in the *python* programming language. The MCMC sampling is done using the library *emcee* (Foreman-Mackey et al., 2013) which implements the affine-invariant ensemble sampler (so-called the "stretch move" algorithm) by Goodman & Weare (2010).

The stretch move algorithm use an ensemble of $K$ random walkers instead of one, all exploring the parameter space simultaneously.

A summary of the stretch algorithm is as follows. First, each walker is initialized at $t = 0$ in random positions in the parameter space. At a step $t$, for each walker $X_k(t)$ in the ensemble, a walker $X_j$ from the rest of the ensemble is pickup at random. A new position $Y$ is proposed, given by:

$$Y = X_j + Z \times (X_k(t) - X_j) \tag{3.8}$$

where $Z$ is a random variable drawn from a probability distribution $g(z)$(so-called, the proposal distribution) given by:

$$g(z) \propto \begin{cases} \frac{1}{\sqrt{z}} & \text{if } z \in [1/a, a] \\ 0 & \text{other cases,} \end{cases} \tag{3.9}$$

where $a$ has a default value of 2, but it is an adjustable parameter of the algorithm that can be adjusted (in rare occasions) to improve the performance. As the name of the algorithm suggests, each chain "stretch" between its current position and the position of another chain in the ensemble. The magnitude and sense of the stretch is random and given by the random variable $Z$.

After a new position $Y$ is proposed, this is then accepted with a probability:

$$q = min\left(1, Z^{N-1} \times \frac{p(Y|D)}{p(X_k(t)|D)}\right). \tag{3.10}$$

Notice that in this step an implementation of the posterior pdf must be called by the MCMC to evaluate $p(\theta = Y|D)$ and return the value back to the MCMC algorithm. In our case, the Equation 3.5 and the prior $p(\theta)$ are evaluated using the occultation data, its measurement errors and the parameter values proposed by the stretch algorithm. If the proposed position $Y$ is accepted, then the chain is updated and $X_k(t+1) = Y$, otherwise $X_k(t+1) = X_k(t)$, which means that the chain stays in the same position and the last state is repeated. Intuitively, we notice that given the factor $p(Y|D)/p(X_k(t)|D)$ in the Equation 3.10, the parameter values more probable will be accepted more often and is the general strategy used by other MCMC algorithms. The previous procedure is repeated for all the chains in the ensemble at each step $t$. The steps are repeated until reach the convergence of the ensemble of chains to the stationary state.

After reaching this steady state, the positions of the ensemble of chains are samples from the target pdf $p(\theta|D)$, and any subset of position taken after this point will be representative of the target pdf. In partice, the ensemble of chains is run for additional $n_{\rm sample}$ steps so to have a representative number of samples in enough quantity to reliably determine the most probable parameter values with their respective uncertainties (typically $10^4$ samples).

**Convergence** To determine how many $n_{\rm burn}$ steps are required to achieve the convergence of the Markov chain, I adopte the integrated autocorrelation

(IAC) time of the samples

$$\tau_f = 1 + 2 \sum_{T=1}^{\infty} \frac{C_f(T))}{C_f(0))}, \tag{3.11}$$

where $C_f(T)$ is the covariance between samples at a time lag T (T is measure in steps).

The IAC time measure how many steps are needed to obtain independent samples, so the chain is run for "several" IAC times (in the order of 10 times the IAC time). After this (the so-called burn stage), the chain is keep running only long enough to obtain the desired number of samples. In practice, the integrated autocorrelation time is implemented as part of the "emcee" library adopted in this work. For the models used in this thesis, the IAC time is typically below 100 steps, and in general the burn stage is run during $\sim 5000 - 10000$ steps when using an ensemble of $\sim 500$ random walkers. Some chains were run for longer number of step with no detectable difference in the results

### 3.2.3 Shape and size of the Centaur object (10199) Chariklo

Has been stressed before the difficulties in the prediction and observation of stellar occultations. As such, it is of great importance the adoption of appropriate methods to use the scarce data available in the best way possible. From the thirteen successful stellar occultations by Chariklo observed between 2013 and 2016, this work uses only five of those where there was simultaneous detection of the main body and the rings. Two of those involved one occultation chord by the main body, while the rest involved only two occultation chord by the body. Single chord occultations are usually neglected or provide only lower size limits. With the approach adopted in this thesis, all the chords provide some information which is reflected in the posterior pdf of the parameters.

#### Fits to light curve amplitudes

As detailed in RL17, the variations in the amplitude of the rotational light curve $\Delta m$ as well as the variation in the V absolute magnitude $H_V$, provide

hints of the shape of Chariklo's main body. $\Delta m$ and $H_V$ also depends on the albedo and variegations of the albedo of the main object as well on the geometry and reflectivity of the rings. Given that, the variation of these quantities in time are used to derive a priori estimates for the size and shape parameter. These are formally introduced in the Bayesian model as prior distribution for the parameters. Among the results presented in RL17, is that the probability distributions adopted for the priors (normal and uniform distributions) and their parameters (median, dispersion for the normal and boundaries for the uniforms) do not have a big influence in the results. In concrete, the more probable values for the semiaxes $a, b, c$ of the elliptical models, and/or the ratios $b/a$, $c/b$ are mainly dominated by the occultation data.

**Rotation period and rotation phase** If a rotation light curve is obtained close to a stellar occultation, in principle the rotation phase and the rotation angle $\phi$ can be derived for that occultation. In practice, and under the Bayesian approach adopted here, this translate to a very localized prior pdf for the rotation angle, improving the determination of the size and shape parameters. Unfortunately the only accurate light curve covering the full rotation of Chariklo is the one obtained in 2013 by Fornasier et al. (2014), from where was deduced a rotation period $T = 7.004 \pm 0.036$ hr. The lower panel of Figure 3.1 shows that after a few weeks is not possible to constrain the rotation phase given the current accuracy in the rotation period. Moreover, the rotation angle propagated back to the occultation of 2013 June 3 (JD=2456446.7677 and only eight days before the data in Fornasier et al. (2014) was taken) can be evaluated numerically as shown in the upper panel in Figure 3.1, from where we obtain $\phi(JD = 2456446.7677) = 356^\circ \pm 54^\circ$. This is compatible with the rotation angle found in RL17 for the ellipsoidal and Jacobi model, but it is not accurate enough to provide an independent constraint. This justify the approach adopted here, were the rotation angle $\phi_i$ at each occultation is considered random and the 'prior' for those angles uniformly distributed in the range 0-$180^{circ}$.

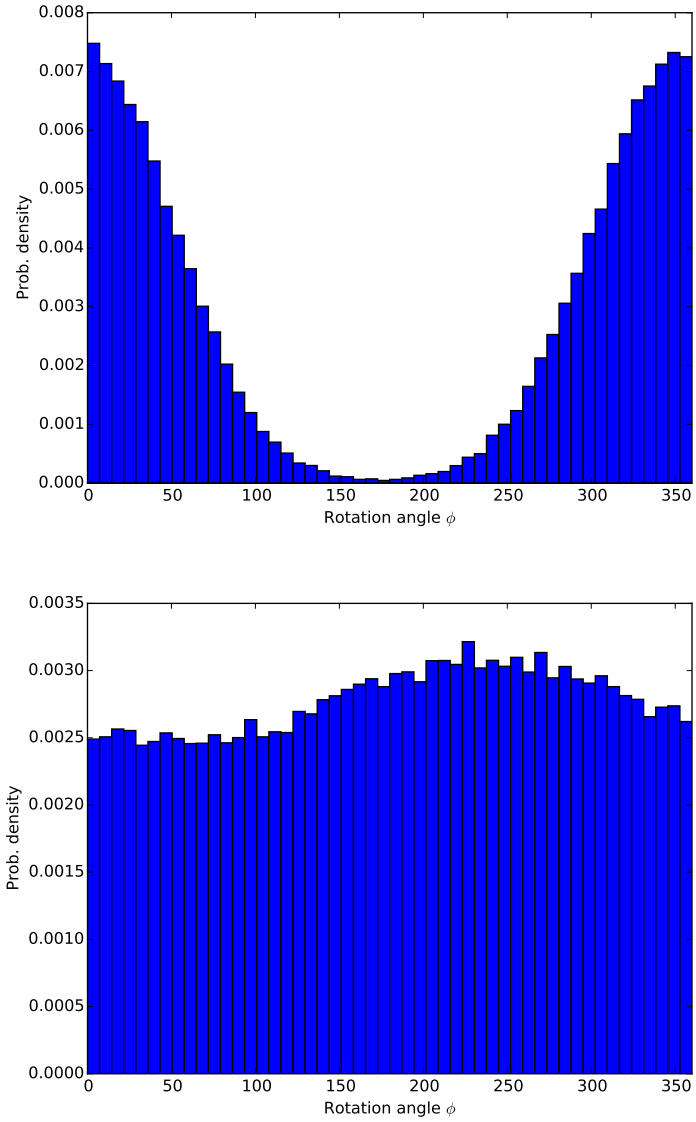


Figure 3.1: Rotation angle $\phi$ derived from rotational light curve by Fornasier et al. (2014). Left: during the stellar occultation in 2013 June 3 the rotation angle is $\phi$=356±54°. Right: three weeks after the rotational light curve measurement, the rotation angle $\phi$ is essentially unknown.

**Comparison with radiometric results**

The size of Chariklo has been determined from thermal measurements varying from 108 km to 151 km (Jewitt & Kalas, 1998; Altenhoff et al., 2001; Sekiguchi et al., 2012; Bauer et al., 2013; Fornasier et al., 2014). We define the equivalent radius $r_{\rm eq}$ given by $A=\pi r_{\rm eq}^2$. In Figure 3.2 we compare $r_{\rm eq}$ for each model (sphere, Maclaurin and Jacobi ) as a function of time with the equivalent radius from thermal measurements. These values are compatible at 2-$\sigma$ level the models following the same trend for the spheroidal and ellipsoidal models. While the similar trend is suggestive, this must be taken with caution as the results from thermal measurements are model dependent. The best approach is to reanalyze the thermal fluxes taken into account the shape and orientations given by stellar occultation results.

The main conclusions of this chapter are:

- The classical approach of using an elliptical fit to the occultation chord is simple and can be readily applied to multi-chord occultations providing strong constraints in the shape and size of the object. Under the assumption of hydrostatic equilibrium I contributed with the derivation of the probability distribution for the density of the TNO 2007 $UK_{126}$.

- The same method was used for the analysis of two multi-chord stellar occultations by the plutino 2003 $AZ_{84}$. In this case I contribute with a substantial part of the analysis to derive a region of possible body density and orientation compatible with both occultations under the assumption of hydrostatic equilibrium of an homogeneous body.

- I successfully apply a Bayesian-MCMC approach to analyze the occultation chords by the Centaur object (10199) Chariklo to constraint it size, shape, density and orientation.

- Chariklo's main body shows to be elongated (a Jacobi ellipsoid or a generic triaxial ellipsoid) as this is consistent with the stellar occultation data, the rotational light curve amplitudes and, in the case of the occultation of 2013, with the expected rotation phase. Nonetheless, the Jacobi model requires ring particles darker than those of Uranus.

- The method applied can be used as more occultation data is collected without the need of further modifications or the adoption of approximations as I adopted in the case of 2003 $AZ_{84}$.
- An aspect to be careful in the Bayesian approach, is the adequate definition of priors and its influence in the results. When the data is scarce, the results (the posterior pdf of the parameters) are influenced by the prior adopted. Nonetheless, as more data is collected the results are expected to be more and more dominated by the occultation data.This gradual transition is in the core of the Bayesian inference and I show that is suitable for the analysis of stellar occultations.
- The density found for the models in hydrostatic equilibrium indicate an icy body as expected for a Centaur object.
- The corresponding mass range (6-8$\times 10^{18}$ kg) implies that the ring particles are close to the 3:1 resonance between the mean motion of the particles and the rotation of the body.

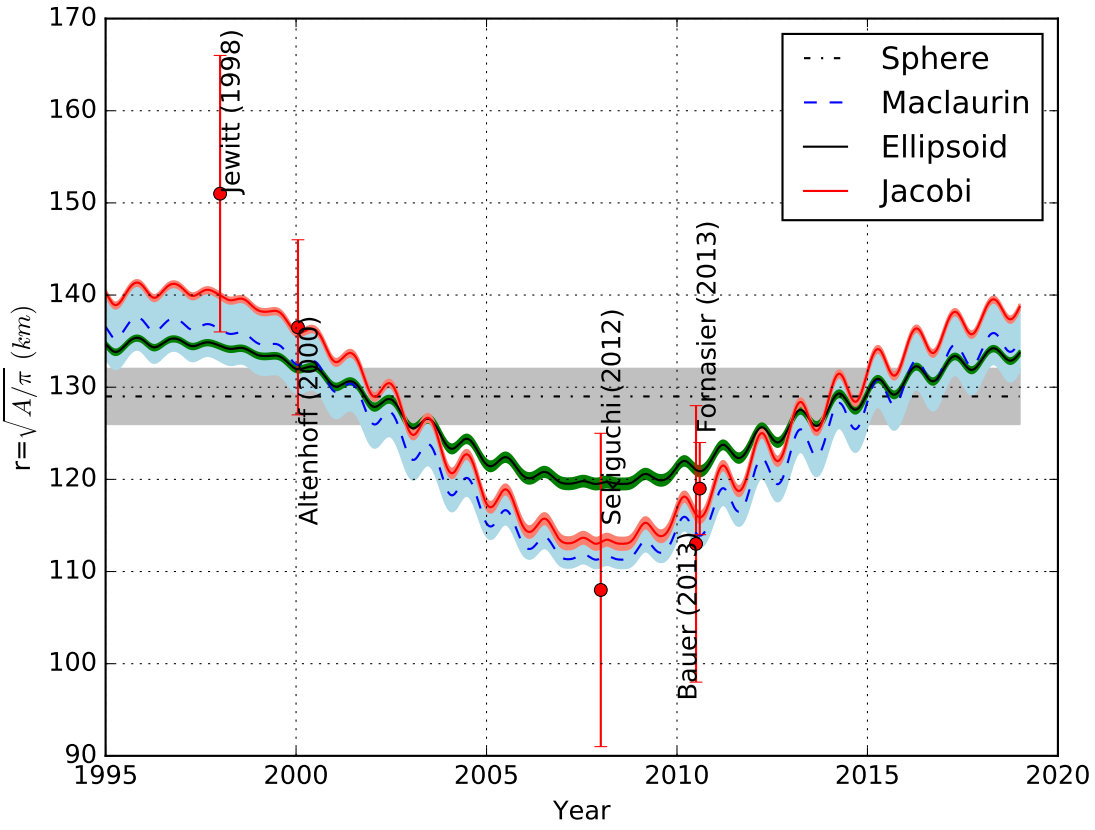


Figure 3.2: Equivalent radius $r_{\rm eq}$ as a function of time. Shaded areas indicate the formal uncertainties. Here $r_{\rm eq}$ is given by $A=\pi r_{\rm eq}^2$ where $A$ is the projected area of Chariklo as a function of time (not to be confused with the volumetric equivalent radius $R_{\rm eq}$). For the ellipsoid and Jacobi models, the average (on a full rotation) of projected area is projected as a function of time. Red dots indicate the radiometric determination of the radius of Chariklo from literature (Jewitt & Kalas, 1998; Altenhoff et al., 2001; Sekiguchi et al., 2012; Bauer et al., 2013; Fornasier et al., 2014). Radiometric values are compatible with the expected projected area of the models at the 2-$\sigma$ level.

Draft version July 4, 2017
Typeset using LaTeX **preprint** style in AASTeX61

# SIZE AND SHAPE OF CHARIKLO FROM MULTI-EPOCH STELLAR OCCULTATIONS *

R. Leiva,[1,2] B. Sicardy,[1] J. I. B. Camargo,[3,4] J. Desmars,[1] D. Bérard,[1] E. Meza,[1] P. Kervella,[1,5] C. Snodgrass,[6] J.-L. Ortiz,[7] R. Duffard,[7] N. Morales,[7] A. R. Gomes-Júnior,[8] G. Benedetti-Rossi,[3,4] R. Vieira-Martins,[8,3,4] F. Braga-Ribas,[9,3,4] M. Assafin,[8] F. Colas,[10] C. De Witt,[11] A. A. Sickafoose,[12,13] H. Breytenbach,[12,14] J.-L. Dauvergne,[15] P. Schoenau,[11] L. Maquet,[10] K.-L. Bath,[11,16] H.-J. Bode,[11,16] A. Cool,[17,18] B. Lade,[19,17,18] S. Kerr,[20,21] and D. Herald[20,22,23]

[1] *LESIA/Observatoire de Paris, CNRS UMR 8109, Université Pierre et Marie Curie, Université Paris-Diderot, 5 place Jules Janssen, F-92195 Meudon Cédex, France.*
[2] *Instituto de Astrofísica, Facultad de Física, Pontificia Universidad Católica de Chile, Av. Vicuña Mackenna 4860, Santiago, Chile*
[3] *Observatório Nacional/MCTIC, Rua General José Cristino 77, RJ 20921-400, Rio de Janeiro, Brazil*
[4] *Laboratório Interinstitucional de e-Astronomia - LIneA, Rua General José Cristino 77, RJ 20921-400, Rio de Janeiro, Brazil*
[5] *Unidad Mixta Internacional Franco-Chilena de Astronomía (CNRS UMI 3386), Departamento de Astronomía, Universidad de Chile, Camino El Observatorio 1515, Las Condes, Santiago, Chile*
[6] *School of Physical Sciences, The Open University, Milton Keynes, MK7 6AA, UK*
[7] *Instituto de Astrofísica de Andalucía, CSIC, Glorieta de la Astronomía s/n, E-18008, Granada, Spain*
[8] *Observatório do Valongo/UFRJ, Ladeira Pedro Antonio 43, RJ 20.080-090, Rio de Janeiro, Brazil*
[9] *Federal University of Technology- Paraná (UTFPR/DAFIS), Rua Sete de Setembro, 3165, CEP 80230-901, Curitiba, PR, Brazil*
[10] *IMCCE, Observatoire de Paris, PSL Research University, CNRS, Sorbonne Universités, UPMC Univ. Paris 06, 77 Av. Denfert-Rochereau, F-75014, Paris, France*
[11] *IOTA/ES, Barthold-Knaust-Strasse 8, D-30459 Hannover, Germany*
[12] *South African Astronomical Observatory, P.O. Box 9, 7935 Observatory, South Africa*
[13] *Department of Earth, Atmospheric, and Planetary Sciences, Massachusetts Institute of Technology Cambridge, MA 02139-4307, United States*
[14] *University of Cape Town, Department of Astronomy, Rondebosch, Cape Town, 7700, South Africa*
[15] *AFA/Ciel et Espace, 17 Emile Deutsch de la Meurthe, F-75014, Paris, France*
[16] *Internationale Amateursternwarte e. V. IAS, Hakos/Namibia and Bichler Str. 46, D-81479, Munich, Germany*
[17] *Defence Science & Technology Group, P.O. Box 1500, Edinburgh SA 5111, Australia*
[18] *The Heights Observatory, 12 Augustus St, Modbury Heights SA 5092, Australia*
[19] *Stockport Observatory, Astronomical Society of South Australia, Stockport, SA, Australia*
[20] *Occultation Section of the Royal Astronomical Society of New Zealand (RASNZ), P.O. Box 3181, Wellington, New Zealand*
[21] *Astronomical Association of Queensland, 5 Curtis Street, Pimpama QLD 4209, Australia*
[22] *International Occultation Timing Association (IOTA), P.O. Box 7152, Kent, WA 98042, USA*
[23] *Canberra Astronomical Society, Canberra, ACT, Australia*

## ABSTRACT

Corresponding author: R. Leiva
rnleiva@uc.cl

* Based on observations obtained at the Southern Astrophysical Research (SOAR) telescope, which is a joint project of the Ministério da Ciência, Tecnologia, e Inovação (MCTI) da República Federativa do Brasil, the U.S. National Optical Astronomy Observatory (NOAO), the University of North Carolina at Chapel Hill (UNC), and Michigan State University (MSU).

We use data from five stellar occultations observed between 2013 and 2016 to constrain Chariklo's size and shape, and the ring reflectivity. We consider four possible models for Chariklo (sphere, Maclaurin spheroid, tri-axial ellipsoid and Jacobi ellipsoid) and we use a Bayesian approach to estimate the probability distributions for the corresponding parameters. The spherical model has a radius $R = 129 \pm 3$ km. The Maclaurin model implies equatorial and polar radii of $a = b = 143^{+3}_{-6}$ km and $c = 96^{+14}_{-4}$ km, respectively, with corresponding density $970^{+300}_{-180}$ kg m$^{-3}$ and mass $(8 \pm 1) \times 10^{18}$ kg. The ellipsoidal model has semiaxes $a = 148^{+6}_{-4}$ km, $b = 132^{+6}_{-5}$ km and $c = 102^{+10}_{-8}$ km. Finally, the Jacobi model has semiaxes $a$=157±4 km, $b$=139± 4 km and $c$=86±1 km, density $796^{+2}_{-4}$ kg m$^{-3}$ and mass $(6 \pm 0.1) \times 10^{18}$ kg. Depending on the model, we obtain topographic features of 6-11 km, typical of Saturn icy satellites with similar size and density. We constrain Chariklo's geometric albedo between 3.1% (sphere) and 4.9% (ellipsoid), while the ring reflectivity $I/F$ is less constrained between 0.6% (Jacobi) and 8.9% (sphere). The ellipsoid model naturally explains the long-term photometry variation of the system between 1997 and 2015, giving plausible values for $I/F = 4.9 \pm 0.3\%$, and it is our preferred model. The derived Chariklo's mass places the rings close to the 3:1 resonance between the ring mean motion and Chariklo's rotation period.

*Keywords:* methods: statistical — minor planets, asteroids: individual (Chariklo) — occultations — planets and satellites: rings

## 1. INTRODUCTION

The Centaur object (10199) Chariklo is the only small object of the Solar System known so far to show the unambiguous presence of a ring system. It was discovered during a ground-based stellar occultation in 2013 (Braga-Ribas et al. 2014), and confirmed by several subsequent observations (Bérard et al. 2017).

Meanwhile, the basic physical characteristics of Chariklo remain fragmentary. Chariklo's radius estimations, taken from thermal measurements, vary from 108 km to 151 km, with geometric albedo in the range 4-8% (Jewitt & Kalas 1998; Altenhoff et al. 2001; Sekiguchi et al. 2012; Bauer et al. 2013; Fornasier et al. 2014). The 2013 stellar occultation had a poor coverage of the main body, providing a spheroidal shape with equatorial radius $a = 144.9$ km and polar radius $c = 114$ km.

Rotational light curves obtained in the visible between 1997 and 2013 exhibit a variable peak-to-peak amplitude from non detectable in 1997 and 1999 to amplitudes of 0.11-0.13 in 2006 and 2013 respectively (Davies et al. 1998; Peixinho et al. 2001; Fornasier et al. 2014; Galiazzo et al. 2016). This can be produced by an elongated body, longitudinal albedo variegations or more probably, a combination of both. The best measurements provide a rotation period of 7.004±0.036 hr (Fornasier et al. 2014). Spectroscopic measurements show the presence of water ice in the system (Guilbert-Lepoutre 2011; Duffard et al. 2014). Finally, no satellites have been detected around Chariklo, preventing any mass estimation.

The size, shape and density of Chariklo are important parameters to constrain the origins of both the main body and its rings. Moreover, topographic features and/or an ellipsoidal shape may have drastic influence in the ring dynamics through resonances between ring mean motion and body rotation.

Here we use several stellar occultations to put constraints on the size and shape of Chariklo's main body. This technique has been used on several TNOs and Centaur objects, including 2002 $TX_{300}$ (Elliot et al. 2010), Eris (Sicardy et al. 2011), Makemake (Ortiz et al. 2012), Varuna (Sicardy et al. 2010), Quaoar (Braga-Ribas et al. 2013), 2002 $KX_{14}$ (Alvarez-Candal et al. 2014), 2007 $UK_{126}$ (Benedetti-Rossi et al. 2016; Schindler et al. 2017) and 2003 $AZ_{84}$ (Dias-Oliveira et al. 2017).

Due to the very small angular size of Chariklo ($\sim$ 80 milliarcsecond, rings included), prediction of stellar occultations are difficult and coverage of the shadow path is poor with only a few chords on the body per event. In order to retrieve the full 3D structure of the body, we have to use some a priori hypotheses about the shape of the body (e.g. sphere, spheroid, ellipsoid). Moreover, to assess the more probable shape parameters given the sparse data, we have adopted a Bayesian approach to derive posterior probability distributions for the radius of the spherical model, size, shape and orientation for the Maclaurin, ellipsoidal and Jacobi models. The advantage of this method is that it can incorporate knowledge from complementary observations, in a quantitative way avoiding qualitative assumptions (Brown 2013).

In Section 2 we describe the prediction of occultations and the observations, resulting in a total of eight occultation chords observed during five stellar occultations between 2013 and 2016. In Section 3 we describe the rings, main body models and the implementation of the Markov Chain Monte Carlo (MCMC) to derive parameter values. In Section 4 we describe the main results, before discussions (Section 5) and concluding remarks (Section 6).

## 2. OBSERVATIONS

### 2.1. *Prediction of stellar occultations*

Stellar occultation predictions by (10199) Chariklo for the period 2012.5-2014 were based on local catalogs with astrometric positions of the stars around Chariklo's path on the sky. Moreover, improved ephemerides for Chariklo were obtained from those catalogs with typical uncertainties of 20-30 mas (Camargo et al. 2014). A similar approach was used for predictions after 2014 using the Wide Field Imager (WFI) at the MPG 2.2-m telescope (La Silla, Chile) and the IAG 0.6 m telescope at OPD/LNA (Pico dos Dias, Brazil). For the occultation of 2016 October 1, the star position was obtained from GAIA Data Release 1 (Gaia Collaboration et al. 2016a,b). A total of thirteen positive occultations were observed up to 2016 (see details in Bérard et al. 2017). Each event provided the position of Chariklo relative to the star with an accuracy of a few milliarcsecond (mas). Those positions were used in turn to improve Chariklo's ephemeris, providing updated orbital elements in the so-called Numerical Integration of the Motion of an Asteroid (NIMA) procedure (Desmars et al. 2015), and permitting better subsequent predictions.

### 2.2. *Observations and data reduction*

Among the thirteen stellar occultations observed between 2013 and 2016 (Braga-Ribas et al. 2014; Bérard et al. 2017), we use the five of those including simultaneous detections of the main body and rings. In those cases, the orientation and center of the system can be constrained as detailed in Section 3.1. The 2013 June 3, 2014 June 28 and 2016 October 1 events were double-chord while the 2014 April 29 and 2016 August 8 events were single-chord. Additionally, we consider the stations whose negative detections (that is, no occultation by the body) were close enough to the main body's limb such to constrain its extension. In consequence, from the occultation of 2013 June 3 we use the negative detections from Ponta Grossa and Cerro Burek (Braga-Ribas et al. 2014), from 2014 April 29 we use a negative detection from Springbok, and from 2014 June 28 we use the negative detection from Hakos. Table 1 gives the circumstances of the observations between 2014 and 2016 used in this work. Details of observations from other sites and stellar occultations not used in this work are given in Braga-Ribas et al. (2014) and Bérard et al. (2017).

For each observation the images were reduced in a standard way applying dark and flat frames. Then we performed aperture photometry for the occulted star and comparison stars in the same image. Finally we perform relative photometry between the occulted star and comparison star(s) to correct for variations in the sky transparency. The optimal aperture size was chosen in each case for the target and comparison star(s) to obtain the best signal-to-noise ratio (SNR) in each light curve. The background flux was estimated near the target and nearby reference stars, and then subtracted, so that the zero flux corresponds to the sky level. The total flux from the unocculted star and Chariklo was normalized to unity after fitting the light curve by a third or forth-degree polynomial before and after the event. Figures 1 and 2 show the light curves obtained with this procedure.

### 2.3. *Occultation timing analysis*

For each light curve involving the body detection, we determine the times of ingress $t_{\rm ing}$ and egress $t_{\rm egr}$ of the occulted star behind Chariklo by fitting a sharp-edge occultation profile. This profile is convolved by Fresnel diffraction produced by the sharp edge of the body, then convolved by the stellar diameters projected at Chariklo's distance, the integration time and the bandwidth of the optical system (product of the telescope, detector and filter responses) as described in Widemann et al. (2009). The profile takes into account the relative speed of the star with respect to Chariklo

in the sky plane $v_{ch}$, and the orientation angle $\alpha$ between the occultation chord and the normal to the local limb. For instance, for a local limb perpendicular to the occultation chord, we have $\alpha$=0.

The angle $\alpha$ and times $t_{\rm ing}$, $t_{\rm egr}$ are obtained by minimizing a classical $\chi^2$ function

$$\chi^2 = \sum_1^N \frac{(\phi_{i,o} - \phi_{i,m})^2}{\sigma_i^2}, \quad (1)$$

where $\phi_{i,o}$ is the normalized flux observed, $\phi_{i,m}$ is the synthetic flux from the diffraction model and $\sigma_i$ is the uncertainty in the measured photometry.

Except for the occultation of 2013 June 3 observed with the Danish telescope, the light curves are dominated by the long integration time instead of diffraction effects, so that the angle $\alpha$ is unconstrained and only the ingress and egress times are obtained.

Table 2 gives the adopted stellar diameters projected at Chariklo's distance, Chariklo's geocentric range and the predicted coordinates of the occulted stars and Chariklo at a reference time. For the occultations of 2014 June 28 and 2016, the apparent stellar diameters are estimated using the $V$ and $K$ apparent magnitudes provided by the NOMAD catalog (Zacharias et al. 2004) using the V-K relations from Kervella et al. (2004) and considering galactic reddening. For 2013 June 3 and 2014 April 29 we adopt the apparent stellar diameter derived in (Braga-Ribas et al. 2014; Bérard et al. 2017).

The occultations by the main inner ring (C1R) and the external fainter ring (C2R) show variable width and radial profiles and are described and analyzed in detail in Bérard et al. (2017). Here we take the midtimes $t_{\rm mid}$ of the rings detections from that work, that we use in turn to constrain the body apparent center as explained in 3.1.

The timings corresponding to the occultations by the main body and the rings provide a set of offsets $(f, g)$ of the star with respect to the expected body center as seen from each site. Those offsets are measured in the sky plane at Chariklo's distance and they are counted positive toward the east and north. Table 3 summarizes the timings and offsets for the body detections while Table 4 lists the ring detections. Figure 4 shows the occultation chords in the sky plane. Particular conditions during the occultations of 2013 June 3 and 2014 April 29 are discussed below.

*South America. 2013 June 3*—For this occultation we keep most of the timing analysis reported in (Braga-Ribas et al. 2014, extended data Table 5), but we re-analyzed the light curve obtained at the Danish telescope. This light curve has the highest SNR and a high acquisition rate of 10 Hz, allowing us to resolve diffraction effects fitting simultaneously the time of ingress/egress and the orientation angle $\alpha$.

Figure 1 shows the best fits, from where we derive $\alpha_{\rm ingress} = 60.2 \pm 0.9°$ at ingress and $\alpha_{\rm egress} = 73.0 \pm 0.8°$ at egress, while ingress and egress timings are given in Table 3. For illustration, the same figure indicate the modeled light curve for $\alpha$ departing $\pm 10°$ with respect to the best-fit showing a clear departure from the data.

From this we calculate the relative angle $\Phi_{\rm limb}$ between the local and global limb, the latter understood as the tangent to the projected limb. Depending on the main body model, we obtain $\Phi_{\rm limb}$=2-10° at ingress and $\Phi_{\rm limb}$=15-25° at egress. The angle $\Phi_{\rm limb}$ corresponds to what is known as the angle of internal friction, or maximum angle of repose. As illustration, Figure 3 shows a local view of the occultation geometry in the sky plane for the generic ellipsoidal model indicating the occultation chord, the local limb, the global limb and the angles $\alpha$ and $\Phi_{\rm limb}$.

Finally, the occultation timings by the main body obtained at the PROMPT telescope (as given by Braga-Ribas et al. (2014)), as well as the non-detection at Cerro Burek and Ponta Grossa are used as further constraints.

*South Africa. 2014 April 29*—This occultation revealed that the occulted star was in fact double. A stellar atmosphere fit was performed to determine the relative flux and apparent diameter of the stars as detailed in (Bérard et al. 2017) The separation between the main (A) and secondary (B) stars and the diameter of each component projected at the distance of Chariklo are given in Table 2.

The occultation of the primary star by the rings was detected at Springbok, while the occultation of the secondary was not detected due to the low SNR. There were two additional detections of the rings, one involving the C2R ring occulting the primary star at Gifberg and the other one involving C1R ring occulting the secondary star at SAAO. The panel b of Figure 4 shows the two sets of occultations of the primary and secondary stars in the plane of the sky. The panel c of Figure 4 shows the reconstructed geometry of the event after applying the offset between the components of the double star to the occultations of the secondary star.

## 3. BODY MODELS

### 3.1. *Ring model*

All the ring occultations observed so far are consistent with two concentric and circular rings with fixed pole position and fixed radius, within $\sim 1^\circ$ and within $\sim 3.3$ km of the discovery values, respectively (see Braga-Ribas et al. 2014; Bérard et al. 2017). For a particular date, the rings are projected on the sky plane as an ellipse centered with semimajor axis corresponding to the ring radius. The ring opening angle $B$ and the position angle of the semiminor axis $P$ are calculated from the pole position in Table 5 and Chariklo's position in the sky. The single-chord ring occultation of 2016 August 8 provides two possible ring centers while the other events give a unique center. The ring centers $(f_c, g_c)$ are listed in Table 4, with error bars that reflect the uncertainties on the ring midtimes given in Table 4. Occultations indicate that the radial width of the main ring varies between 5 and 7.5 km adding an additional bias in the determination of the center of $\sim 1$ km. This is in the order of the formal uncertainties for most of the events and it is not a dominant effect in the determination of the center of the projected ellipse. The best fitted ellipses for each event are displayed in Figure 4.

### 3.2. *Body model*

Here we adopt the assumption that the ring system lies in the equatorial plane of the object. This is because in doing so, a collisional dissipative ring reaches its minimum energy configuration, while conserving its angular momentum parallel to the body spin axis. With this assumption (plus the circularity described above) the body and the rings share the same pole position and the same center.

If Chariklo is completely irregular, a simple parametric model (e.g. sphere, ellipsoid) gives a poor estimation of dimensions of the body. A well sampled stellar occultation could indicate if Chariklo is irregular but, unfortunately, to date we have only a few occultations with one or two positive detections each (Table 3 and Figure 4). In that context, we test simple models that can be easily parametrized in order to give credible intervals for the corresponding parameters. In practice, we first assume a spherical body that is used to estimate a radius and the scale of topographic features. Next, we consider a generic triaxial ellipsoid to estimate the length of the semiaxes $a$, $b$ and $c$ and the

scale of topographic features. Finally, considering hydrostatic equilibrium of a homogeneous body, it assumes either a Maclaurin (spheroid) or a Jacobi (tri-axial ellipsoid) shape for which size, axes ratios, density and topographic features can be evaluated. The non-spherical models incorporate independent information as a priori estimates for the model parameters, like the amplitude of the rotational light curve or the long term photometric behavior of the system. The models mentioned above (sphere, triaxial ellipsoid, Maclaurin and Jacobi) are now discussed in turn.

#### 3.2.1. *Sphere model*

This is the simplest case as there is only one free parameter, the sphere radius $R$. The projection in the sky plane is a circle with the same radius $R$ for all occultations. The problem is then reduced to find a circle that best fits all the chords extremities $(f, g)$ provided in Table 3 with the center located at the $(f_c, g_c)$ values indicated in Table 5.

#### 3.2.2. *Triaxial ellipsoid*

Here we consider a generic triaxial ellipsoid with semiaxes $a > b > c$, rotating around the shortest axis. We define the rotation angle $\phi$ as the angle from the central meridian to the prime meridian counted positively along the equator of the object using the right hand rule. The prime meridian is the one passing through one of the two intersections between the equator and the longer axis of the ellipsoid. Given the current uncertainty in the rotation period, the rotation phase is lost after a few weeks and the rotation angle in each occultation is considered as independent.

The eight free parameters of this model are $a$ (which gives us the size of the object), the ratios $0 < b/a < 1$ and $0 < c/b < 1$, and the rotation angles $\phi_i$ at each of the five occultations.

#### 3.2.3. *Maclaurin spheroid*

A Maclaurin spheroid has an equatorial radius $a$ and polar radius $c$ related by (Chandrasekhar 1987)

$$\Omega = \frac{\omega^2}{\pi G \rho} = \frac{2\sqrt{1-e^2}}{e^3}\left[\left(3-2e^2\right)\arcsin e - 3e\sqrt{1-e^2}\right], \tag{2}$$

where $e^2 = 1-(c/a)^2$, $\omega = 2\pi/T$ ($T$ being the rotation period of the body), $G$ the gravitational constant and $\rho$ its (uniform) density. Note that $\Omega$ is basically the adimensional rotational parameter that compares the centrifugal acceleration at the equator of the body to its gravity. For stable Maclaurin shapes this parameter is between $\Omega = 0$ and $\Omega \simeq 0.374$. The lower limit corresponds to the spherical limit with $\rho \to \infty$ while the upper limit corresponds to the maximum oblateness and the minimum density. Here we adopt a rotation period of $T = 7.004$ hr (Fornasier et al. 2014) giving a minimum density

$$\rho_{\min} = 791 \text{ kg m}^{-3}. \tag{3}$$

In this case we have two free parameters, the equatorial radius $a$ and the density $\rho$ (that determine $c$, i.e. the shape).

#### 3.2.4. *Jacobi ellipsoid*

A Jacobi ellipsoid is tri-axial with semiaxes $a > b > c$, rotating around the shortest axis. The shape and size (given by $a$, $b$ and $c$), the rotation period $T$ and the (uniform) density $\rho$ are related

by (Chandrasekhar 1987):

$$\Omega = \frac{\omega^2}{\pi G\rho} = 2abc\int_0^\infty \frac{u}{(a^2+u)\,(b^2+u)\,\Delta}du \tag{4}$$
$$a^2b^2\int_0^\infty \frac{du}{(a^2+u)\,(b^2+u)} = c^2\int_0^\infty \frac{du}{(c^2+u)\,\Delta}$$
$$\Delta = \sqrt{(a^2+u)\,(b^2+u)\,(c^2+u)},$$

which can be solved numerically.

For a stable Jacobi ellipsoid, the shapes lie between the axi-symmetric spheroid limit with $\Omega = 0.374$ and the most elongated solution with $\Omega = 0.284$. For the adopted rotation period of 7.004 hr the density is in the range $791 < \rho < 1040$ kg m$^{-3}$.

We define the prime meridian and rotation angle $\phi$ as we did for the generic ellipsoid.

The seven free parameters of this model are $a$ (which give us the size of the object), the density $\rho$ (which gives us the shape with the Equation 4), and the rotation angles $\phi_i$ at each of the five occultations.

### 3.3. *Bayesian approach and MCMC implementation*

Here, we adopt a Bayesian approach to derive probability densities and credible intervals for the physical parameters $\theta$ of the models described above given the occultation data $D$. We are interested in the "posterior" probability density $p(\theta|D)$ given by:

$$p(\theta|D) \propto \mathcal{L} \times p(\theta), \tag{5}$$

where $\mathcal{L}$ is the likelihood function, and $p(\theta)$ is the so-called "prior" distribution.

The likelihood $\mathcal{L}$ determines the probability to obtain the data $D$ given the physical model, and a model of the data uncertainties. On the other hand, the prior distribution $p(\theta)$ condense the previous knowledge we have about the parameters. We define the likelihood function $\mathcal{L}$, assuming that the errors stemming from the fits described in 2.3 have normal distributions. Moreover, we formally consider statistical uncertainties in our model by introducing an extra Gaussian random variable with median zero and standard deviation $\sigma_m$, independent from the measurements. For instance, the parameter $\sigma_m$ may account for unmodeled topographic features on an otherwise smooth ellipsoidal model for the body. Thus, $\sigma_m$ is estimated from the data and counted as an extra parameter for each physical model. With these considerations $\mathcal{L}$ is given by (see for example Equation 4.52 of Gregory 2005)

$$\mathcal{L} = (2\pi)^{-N/2}\left\{\prod_{i=1}^{N}\left(\sigma_{ri}^2+\sigma_m^2\right)^{-\frac{1}{2}}\right\}\exp\left\{-\sum_{i=1}^{N}\frac{(y_i - m\,(x_i\mid\theta))^2)}{2\,(\sigma_{ri}^2+\sigma_m^2)}\right\}, \tag{6}$$

where $N$ is the number of data points $y_i = (f_i, g_i)$ derived in 2.3, corresponding to the extremities of each occultation chord by the main body, $x_i$ represent the independent variable (the site and time of each occultation), $\sigma_{ri}$ are the uncertainties on the chord extremities $\sigma_{ch}$ projected along the radial direction counted from the center $(f_c, g_c)$ of the body (see Table 5). Finally, $\theta$ is the vector representing the parameters of the model that describes the object. In that context, $m\,(x_i\mid\theta)$ is the position of the chord extremity predicted by each model. The prior $p(\theta)$ is derived from physical considerations (for instance, the stability criteria for Maclaurin and Jacobi models), and the observational evidence as explained below.

### 3.3.1. *Analysis of photometry*

Here we consider the rotational light curve amplitude $\Delta m$ and V absolute magnitude $H_V$ which is in turn used to derive a priori estimates for Chariklo's size, shape and/or density, depending on the model adopted. For this we model the long term variation (in period of years) of the rotational light curve amplitude $\Delta m$ and absolute magnitude $H_V$ as explained below. These a priori estimates are incorporated in the Bayesian modeling through the prior probability distribution $p(\theta)$.

*Rotational light curve amplitude*—Chariklo exhibits a rotational light curve amplitude that varies in time. There was no detection of the light curve amplitudes taken in 1997 and 1999 (Davies et al. 1998; Peixinho et al. 2001), when Chariklo was close to its maximum opening angle. Amplitudes of 0.13 mag and 0.11 mag were then measured in 2006 and 2013 respectively (Galiazzo et al. 2016; Fornasier et al. 2014). We estimate the limits for the amplitudes in 1997 and 1999 and the uncertainties in 2006 and 2013 from the uncertainties in the photometry given by the authors.

Here we add to this data set a partial light curve obtained in July 2015 with the SOAR Optical Imager (SOI). About 200 images were taken with the R Bessell filter using an exposure time of 80 s. A bias correction and flat-fielding was performed with the SOAR/SOI IRAF routines. The images were processed using difference image photometry implemented in the IDL code *DanDIA* (Bramich 2008). A light curve was obtained using aperture photometry with IRAF routines (Tody 1986). Figure 5 shows the light curve obtained covering ∼5 h from which we determined a peak-to-peak amplitude $\Delta m$=0.06±0.02.

Values from the literature and from this work are summarized in Table 6. Using the pole position from Table 5 we calculate the opening angle $B$ for each date that indicates a correlation between $\Delta m$ and $|B|$. The double-peaked light curve from Fornasier et al. (2014) with minimums separated by about half rotation phase suggest that the brightness variations are dominated by the projected area of an elongated body instead of albedo variegations.

With these considerations, we model the peak-to-peak rotational light curve amplitude with the contribution of the main body and rings given by (Fernandez-Valenzuela et al. 2016)

$$\Delta m = -2.5 \log \left( \frac{A_{\rm min} p_b + A_r (I/F)_r}{A_{\rm max} p_b + A_r (I/F)_r} \right), \tag{7}$$

where $A_{\rm min}$ and $A_{\rm max}$ are the maximum and minimum projected area of Chariklo's body respectively, $p_b$ is the geometric albedo of Chariklo's body, and $(I/F)_r$ is the ring reflectivity.

*Absolute magnitude*—Chariklo also exhibits an absolute V magnitude $H_V$ that varies in time (Belskaya et al. 2010; Fornasier et al. 2014; Duffard et al. 2014). Considering contributions from the changing aspect of Chariklo's main body and its rings, we model $H_V$ with the relation

$$H_V = H_\odot - 2.5 \log \left( \frac{A_b \; p_b + A_r \; (I/F)_r}{\pi \; au_{km}^2} \right), \tag{8}$$

where $H_\odot$=-26.74 is the absolute magnitude of the Sun in V, $A_b$ is the projected area of Chariklo's main body, $A_r$ is the projected area of the rings, and $au_{km}$ is an Astronomical Unit in km.

*Priors for the generic ellipsoid*—For the generic triaxial ellipsoid we use the $\Delta m$ and $H_V$ to derive estimates for the semimajor axis $a$ and the ratios $b/a$ and $c/a$.

To derive the ring contribution to the brightness variations, we consider a ring of radius $\sim$ 400 km and width $w_1$ $\sim$5.5 km (neglecting the contribution from the faint and narrow C2R ring), and a ring reflectivity $(I/F)_r$ varying between 0% (neglecting the ring contribution) up to 9%, considering previous estimations of this quantity (Braga-Ribas et al. 2014; Duffard et al. 2014). For the body contributions, we adopt a body geometric albedo $p_b = 4.2 \pm 0.5\%$ from Fornasier et al. (2014),

We fit the Equations 7 and 8 to the $\Delta m$ values in Table 6 and $H_V$ from the literature in a least-squares scheme, to obtain

$$a = 138 \pm 16\ km, \frac{b}{a} = 0.86 \pm 0.04, \frac{c}{b} = 0.89 \pm 0.30, \tag{9}$$

which are used in Section 4.2 to define normally distributed priors for those parameters.

*Priors for Maclaurin spheroid*—For the Maclaurin model we use $H_V$ values to derive estimates for the equatorial radius $a = b$ and the density $\rho$. Adopting the same ring dimensions, body geometric albedo and range of ring reflectivity as before, we fit the Equation 8 to the $H_V$ from the literature in a least-squares scheme to obtain

$$a = b = 135 \pm 25\ km, \tag{10}$$

while the density $\rho$ is unbounded and can take values in all the valid interval between $\rho = 791$ kg m$^{-3}$ and $\rho \to \infty$.

In practice, we consider a conservative upper limit for the density

$$\rho_{\max} = 5000\ kg\ m^{-3}, \tag{11}$$

after considering the known density distribution of asteroids and TNOs (Britt et al. 2002; Carry 2012).

These values are used in Section 4.3 to define normally and uniformly distributed priors for those parameters.

*Priors for Jacobi*—For the Jacobi ellipsoid we must impose the binding conditions from Equation 4 to $a$, $b$ and $c$. As done with the generic ellipsoid, we fit the Equations 7 and 8 to the $\Delta m$ and $H_V$ values to obtain

$$a = 151 \pm 13\ km, \rho = 804 \pm 6\ kg\ m^{-3}. \tag{12}$$

which is used to define normally distributed priors in Section 4.4.

*Rotation angle during occultations*—It is worth to mention here some words about the rotation angle during the stellar occultations. The rotation light curve from Fornasier et al. (2014) was obtained in 2013 between June 11 and June 12. Assuming that most of the variability is due to shape instead of albedo variegations, we define the rotation angle $\phi$=0° at one of the brightness minima of that light curve, for instance JD=2456455.23. This is used to determine the rotation angle $\phi(JD, T_{\rm sid})$ at any given date $JD$ for a given sidereal period $T_{\rm sid}$. For instance, for the stellar occultation of June 3, which is only eight days before this measurement, we find

$$\phi_{\rm 2013Jun03} = 356° \pm 54°, \tag{13}$$

adopting $T_{\rm sid} = 7.004 \pm 0.036$ hours. Unfortunately, given the current accuracy of the rotation period, the rotation angle is essentially lost after a few weeks, preventing us to derive a rotation angle for the occultations in 2014 and 2016 solely from the light curve in Fornasier et al. (2014). The rotation angle in the ellipsoidal and Jacobi models is then considered independent between occultations and explored between 0° and 180° due to the rotational symmetry.

#### 3.3.2. *MCMC scheme*

To estimate the posterior probability distribution $p(\theta|D)$, we adopt a Markov Chain Monte Carlo (MCMC) scheme to draw samples from it. The MCMC sampling is done using the library called *emcee* (Foreman-Mackey et al. 2013) which implements the affine-invariant ensemble sampler by Goodman & Weare (2010).

To generate the posterior samples we follow a standard procedure described below. For each model we run a MCMC with $n_{\rm walk}$ random "walkers", each of them exploring the parameter space. To determine the number of random steps $n_{\rm burn}$ necessary to ensure the chain convergence, we adopt $n_{\rm burn} > 10 \times \tau_f$, where $\tau_f$ is the integrated autocorrelation "time" of the chain measured in chain steps (Foreman-Mackey et al. 2013) (for this we use the implementation given in *emcee*). Once this is done, we continue the MCMC for $n_{\rm samp}$ steps from where we obtain the samples which are representative of the posterior probability of interest $p(\theta|D)$. Then, the marginal probability distribution for the parameters $\theta$ is estimated using the histograms of the samples. From the histograms, we finally derive the best-fit parameter values and credible intervals. For the credible intervals, we use the highest posterior density interval containing 68% of the samples. This is the smallest interval such that any point inside the interval has a higher density than any other point outside of the interval.

Additionally, and as an heuristic test for convergence, for each model we run several chains starting the $n_{\rm walk}$ walkers at different random positions well spread in the parameter space. We repeat this procedure several times to verify that we obtain the same results.

## 4. OCCULTATION RESULTS

### 4.1. *Sphere*

For the spherical model we use as prior a uniform distribution between $R = 100$ and $R = 150$ km, and for $\sigma_m$ we adopt a uniform distribution between 0 km and 50 km Using $n_{\rm walk}$=500, $n_{\rm burn} = 10^4$ steps and $n_{\rm samp} = 10^2$ steps, we obtain the posterior pdf shown in Figure 6, and eventually a sphere radius of $R = 129 \pm 3$ km (68% credible interval).

For the best-fit radius, we obtain a "topographic" parameter $\sigma_m$=11 km. That is, the radial departures from the best-fit limb can be modeled as normally distributed with standard deviation of 11 km, which is $\sim 9\%$ of the radius $R$.

In Figure 7 we compare all the occultation chords with the best fit limb using the spherical model. In Figure 8 we plot the radial difference of each chord extremity with respect to the best limb as a function of the position angle (counted positively from the north toward the east). There is a clear tendency for the chord extremities to be inside the sphere limb around the polar regions and outside the limb in the equatorial regions. As the departures are significantly larger than the uncertainties on the data points, this naturally motivates us to test the flattened models below.

### 4.2. *Tri-axial ellipsoid*

For the triaxial ellipsoid model, we use normally distributed priors for $a$, $b/a$ and $c/b$ with values from Equation 9. The normal distributions are truncated such that $a > 0$ and the ratios $b/a$ and $c/b$ stay in the open interval $]0, 1[$, keeping the condition $a > b > c$. For $\sigma_m$ we adopt a uniform distribution between 0 km and 50 km as with the previous model. Finally, for the rotation angles $\phi_i$ we adopt uniform distributions between 0° and 180°. We do not explore the range $180 - 360°$ due to the rotational symmetry of the ellipsoid.

Using $n_{\rm walk}$=500, $n_{\rm burn} = 10^4$ and $n_{\rm samp} = 10^2$, we obtain the posterior distribution for $a$, $b$ and $c$ shown in Figure 9, and the posterior for rotation angles shown in Figure 10, from which we determine the parameter values given in Table 7. Figure 11 shows the best fit ellipsoid models compared to the occultation chords.

From Figure 10 we obtain a rotation angle $\phi$=120°±45° for the occultation of 2013 June 3. Considering the ellipsoid rotational symmetry, this angle is equivalent to $\phi$=300°±45°, consistent with the one obtained from the rotational light curve in Section 3.3.1. This validates the assumption that the short term variability is dominated by the projected shape of a rotating elongated body rather than albedo features.

*Sensitivity to priors*—To test the sensitivity to priors, we repeat a MCMC run with uniform distribution between 100 km and 200 km for the semimajor axis $a$, and uniform distribution between 0.1 and 1 for the ratios $b/a$ and $c/b$. In this case we determine $a = 147^{+7}_{-3}$ km, $b = 139 \pm 6$ km, $c = 98^{+9}_{-8}$ km. This indicate that the priors have some influence in the results, particularly in the ratio $b/a = 0.95$ which is larger than above. Nonetheless, the parameters obtained are mainly dominated by the occultation data.

### 4.3. *Maclaurin spheroid*

For the prior in density, we use a uniform distribution with values from Equation 3 and 11. For the equatorial radius $a = b$ we use a normally distributed prior with values from Equation 10. Using $n_{\rm walk}$=500, $n_{\rm burn} = 10^4$ and $n_{\rm samp} = 10^2$, we obtain the posterior pdf for the density $\rho$ and equatorial radius $a$ shown in Figure 12. We take the maximum of the joint distribution of $\rho$ and $a$ as the most probable values, while the formal uncertainties are taken from the 68% credible intervals from which obtain the values given in Table 7.

From the joint posterior in the lower-left panel of Figure 12, we note that $\rho$ and $a$ are correlated. For lower densities the hydrostatic equilibrium figure is more flattened and a larger object is needed to match the occultation data.

The upper "wing" for larger densities in the posterior distribution is due to the relation between density and oblateness (Equation 2). As the density increases, the oblateness changes more slowly and the body approaches asymptotically a sphere for $\rho \to \infty$.

Figure 13 shows the nominal Maclaurin solution compared to the occultation chords. As with the ellipsoidal case, the parameter $\sigma_m = 7$ km is smaller than for the spherical model.

*Sensitivity to priors*—As done with the ellipsoidal model, we repeat a MCMC run using a uniformly distributed prior for the equatorial radius $a$ between 100 km and 150 km. From the posterior distribution of $\rho$ and $a$ we obtain $\rho = 950^{+300}_{-150}$ kg m$^{-3}$ and $a$=144±4 km, showing that the results are not strongly sensitive to the priors chosen and are dominated by the occultation data.

### 4.4. *Jacobi ellipsoid*

For the Jacobi ellipsoid model, we use normally distributed priors for the semimajor axis $a$ and density $\rho$ with values from Equation 12.

Additionally, the density must satisfy the condition of equilibrium as described in Section 3.2, that is 791< $\rho$ <1040 kg m$^{-3}$.

Using $n_{\rm walk}$=500, $n_{\rm burn}$ = $10^4$ and $n_{\rm samp}$ = $10^2$, we obtain the posterior pdf for density and semimajor axis shown in Figure 14, and the posterior for rotation angles shown in Figure 15. From this and Equation 4 we derive the parameter values given in Table 7.

Figure 16 shows the best fit Jacobi models compared to the occultation chords . The scattering of the data points with respect to the best-fit limb is given by $\sigma_m$=6 km, similar to the case of the Maclaurin model. From Figure 15 we obtain a rotation angle $\phi$=152°±20° for the occultation of 2013 June 3. Considering the ellipsoid rotational symmetry, this angle is consistent with the one obtained from the rotational light curve in Section 3.3.1.

*Sensitivity to priors*—As done with the ellipsoidal and Maclaurin models, we repeat a MCMC run using a uniformly distributed prior between 100 km and 150 km for the semimajor axis $a$, and between 791 and 1040 kg m$^{-3}$ for the density (the equilibrium condition from Section 3.2). We repeat this analysis removing the prior in the density given by the rotational light curves to evaluate the sensitivity of the results to the adopted priors. In this case we obtain a density $\rho$=$792^{+4}_{-1}$ kg m$^{-3}$ and semiaxes $a$ = 152±5 km, $b$ = $144^{+3}_{-4}$ km and $c$ = $86^{+2}_{-1}$ km. This is similar to the results above, with a slightly smaller object but with same elongation $a-b$ showing that, as with the other models, the results are dominated by the occultation data.

## 5. DISCUSSION

### 5.1. *Topographic features and hydrostatic equilibrium*

The "topographic" parameter $\sigma_m$ (ranging from 6 to 11 km depending on the model) indicates the degree of irregularity of the surface. Compared to the equivalent radius for each model, this irregularities are in the range 5-9%. Moreover, the limb slopes measured in 2013 at one station (Section 2.3 and Figure 3) may reach 25°.

Note that Iapetus, with typical density of 1100 kg m$^{-3}$, can sustain slopes greater than 30° (Castillo-Rogez et al. 2007) while being more massive than Chariklo. Similarly, Hyperion's limb profiles show local slopes of up to 20°, with respect to the fitted elliptical limb (Thomas 1989). More generally, Hyperion is irregular with topographic features of RMS∼ 12% with respect to the mean radius, while Phoebe is close to a spheroid in equilibrium with features of RMS∼ 5% (Castillo-Rogez et al. 2012).

In summary, the topographic features and slopes found for Chariklo are typical of small icy satellites with size and density in the same range than Chariklo.

### 5.2. *Body albedo and rings reflectivity*

We proceed to evaluate the geometric albedo $p_b$ of Chariklo and the ring reflectivity[1] $I/F$, considering the long-term brightness variations of Chariklo. We use the absolute V magnitude $H_V$ from the literature and the same considerations used in Section 3.3.1. Table 7 summarizes the $p_b$ and $I/F$ using least-squares fits to Equation 8. Figure 17 show the fits to the $H_V$ data for the four models,

[1] Here $I$ is the intensity emitted by the ring surface and $\pi F$ is the incident solar flux density. The quantity $I/F$ must not be confused with the geometric albedo of the ring particles $p_p$.

which are virtually indistinguishable to each other but given substantially different relative contribution to the brightness variation from the rings and the main body. The body geometric albedo $p_b$ does not depend strongly on the body model with values in the range 3.1% to 4.2%. In contrast, the ring reflectivity $I/F$ depends on the model adopted for the body. For instance, the spherical model attributes all the photometric variability to the ring resulting in $I/F$=8.9%, close to the previously found value for a spherical body (Braga-Ribas et al. 2014). However, the Jacobi model attribute most of the variability to the changing aspect of Chariklo, resulting in a significantly darker ring, $I/F = 0.6\%$. The Maclaurin and generic ellipsoidal model give intermediate results with $I/F = 3.4\%$ and $I/F = 4.9\%$ respectively but lower than previously estimated values for a non-spherical body (Braga-Ribas et al. 2014; Duffard et al. 2014).

The reflectivity $I/F$ can be related to the albedo of the ring particles $p_p$ in two extreme regimes: a monolayer ring where the ring thickness is comparable to the particle size and a polylayer ring where the ring thickness is large compared to the particles. Currently, there is not enough information to discriminate between these two regimes, but it is illustrative to consider them in turn here.

For a monolayer ring, the equivalent width is defined as $E_p = W(1 - f_n)$, where $W$ is the radial width and $f_n$ is the fractional transmission normal to the ring (Elliot et al. 1984). This gives the effective area covered by the ring particles, neglecting mutual shadowing. Taking the typical value of $E_p$=2.2 km for the main ring C1R (Bérard et al. 2017) and the average width W∼5.5 km considered here, the geometric albedo of the ring particles is $p_p = (5.5/2.2) \times I/F$. Depending on the model used here (from sphere to Jacobi), $p_p$ ranges from 22% to 1.5%, respectively.

In the polylayer regime, the ring reflectivity $I/F$ can be approximated by a single scattering model (Chandrasekhar 1960):

$$I/F = \frac{p_p}{2}\left[1 - \exp\left(\frac{-2\tau_N}{\mu}\right)\right], \tag{14}$$

where $\mu$=sin($B$) and $\tau_N$ is the ring normal optical depth. Using an approximate $\tau_N$=0.4 measured for the main ring C1R (Braga-Ribas et al. 2014), we see that $p_p$ is 2-3 times $I/F$, similar to the monolayer case.

The ring particles thus can be darker than those of Uranus (Karkoschka 2001), $p_p \sim 5\%$, but cannot be as bright as Saturn's ring particles (Cuzzi et al. 2009), $p_p \sim 50\%$.

### 5.3. *Comparison with radiometric results*

Chariklo's equivalent radius[2] $r_{\rm equiv}$ has been estimated from thermal measurements, with values ranging from 108 km to 151 km (Jewitt & Kalas 1998; Altenhoff et al. 2001; Sekiguchi et al. 2012; Bauer et al. 2013; Fornasier et al. 2014).

For the Maclaurin model, $r_{\rm equiv}$ only depends on the opening angle, while for the Jacobi models it depends on the rotation angle. Although observed values are compatible at the 2-$\sigma$ level with our models (with $r_{\rm equiv}$ ranging between 110 km and 140 km), they should be taken with caution because the published radius values have been estimated from simplified models (using NEATM, in some cases even assuming a particular value of the beaming factor) or from more elaborate thermophysical models but without knowledge of pole orientation, and in particular because all models assumed spherical shapes.

[2] Defined as $r_{\rm equiv} = \sqrt{A/\pi}$, where $A$ is the apparent surface area of the body, not be confounded with the volumetric equivalent radius $R_{\rm equiv}$ of each model, which does not depend on orientation.

For the comparison to be realistic, a reanalysis of the thermal data is thus necessary to take into account for different shape models, changes in orientation with time, and to estimate the possible ring contribution to the thermal emission. These aspects are explored in Lellouch et al. (2017).

## 6. CONCLUSIONS

The combination of results from stellar occultations with a quantitative statistical approach is a powerful tool to derive sizes and shapes of small and distant objects. In the case of the Centaur object Chariklo, this is of great importance for constraining the dynamics of its ring system.

In this work we have explored four models for Chariklo's main body shape: a sphere, a triaxial ellipsoid, a Maclaurin spheroid, and a Jacobi ellipsoid. Using a Bayesian approach, we combine five stellar occultations observed between 2013 and 2016 with rotation light curves to derive credible intervals for the size, shape, and density of Chariklo.

Using the spherical model, we find that topographic features with height of about 9% of Chariklo's radius can explain our observations. This is comparable to the values of small icy bodies of similar size and density as Hyperion and Phoebe. However, we observe a clear correlation of the radial residuals with the position angle along the limb, being positive near the equator and negative near the pole. This strongly suggests that Chariklo is flattened or elongated.

The ellipsoidal and Jacobi model are consistent with the stellar occultation data, the rotational light curve amplitude and, in the case of the occultation of 2013, with the expected rotation phase. This suggests that Chariklo is an elongated body.

Clearly, an improved value of Chariklo's rotational period will constrain the rotational angle at each occultation date, and thus reduce the number of free parameters of the models.

Accounting for the fact that Chariklo may have an oblate or ellipsoidal shape, we find that the ring reflectivity is much less constrained than previously considered. While a spherical shape for the body implies ring particles four times brighter than Uranus ring particles, the Jacobi model may result in ring particles twice darker. This large range of uncertainty is a strong incentive for improving our knowledge of Chariklo's size and shape, using better predicted events in the Gaia era, thus allowing well-sampled stellar occultations.

The density obtained in the cases of Jacobi and Maclaurin models is in the range 800-1250 kg $m^{-3}$, indicative of an icy body. This must be taken with caution, though, as this assumes a homogeneous body in hydrostatic equilibrium. The corresponding mass range is 6-8$\times 10^{18}$ kg. With that value, it is interesting to note that the 3:1 resonance between the mean motion of the particles and the rotation of the body[3] is located at radius 408$\pm$20 km, close to the radii of C1R and C2R, respectively 391 km and 405 km. The potential implications of this resonance will be considered in another work.

R. Leiva acknowledges support from CONICYT-PCHA/Doctorado Nacional/2014-21141198. The authors acknowledge support from the French grant "Beyond Neptune II" ANR-11-IS56-0002. Part of the research leading to these results has received funding from the European Research Council under the European Community's H2020 (2014-2020/ ERC Grant Agreement n° 669416 LUCKY STAR). The research leading to these results has received funding from the European Union's Horizon 2020 Research and Innovation Programme, under Grant Agreement N°. 687378, project SBNAF. E.M. acknowledges support from the Contrato de subvención 205-2014 Fondecyt - Concytec, Perú. J.I.B.C.

[3] At this resonance a ring particle undergoes one revolution while Chariklo completes three rotations.

acknowledges a CNPq grant n° 308150/2016-3. M.A. thanks the CNPq (Grants 473002/2013-2 and 308721/2011-0) and FAPERJ (Grant E-26/111.488/2013). G.B-R. acknowledges for the support of the CAPES (203.173/2016) and FAPERJ/PAPDRJ (E26/200.464/2015 - 227833) grants. R.V-M thanks grants: CNPq-306885/2013, Capes/Cofecub-2506/2015, Faperj: PAPDRJ-45/2013 and E-26/203.026/2015 This work is partly based on observations performed at the MPG 2.2 meter telescope, program CN2016A-87. Based on observations obtained at the SOAR telescope, program SO2015A-015. The 50 cm telescopes used for the Hakos observations belong to the IAS observatory at Hakos/Namibia. This work was partially supported by the National Research Foundation of South Africa and contains data taken at the South African Astronomical Observatory (SAAO). This work has made use of data from the European Space Agency (ESA) mission *Gaia* (https://www.cosmos.esa.int/gaia), processed by the *Gaia* Data Processing and Analysis Consortium (DPAC, https://www.cosmos.esa.int/web/gaia/dpac/consortium). Funding for the DPAC has been provided by national institutions, in particular the institutions participating in the *Gaia* Multilateral Agreement.

*Facilities:* SOAR (SOI), Max Planck:2.2m (WFI), LNA:BC0.6m

## REFERENCES

Altenhoff, W. J., Menten, K. M., & Bertoldi, F. 2001, Astronomy and Astrophysics, 366, L9. http://doi.org/10.1051/0004-6361:20000543

Alvarez-Candal, A., Ortiz, J. L., Morales, N., et al. 2014, Astronomy & Astrophysics, 571, A48. http://doi.org/10.1051/0004-6361/201424648

Bauer, J. M., Grav, T., Blauvelt, E., et al. 2013, The Astrophysical Journal, 773, 22. http://doi.org/10.1088/0004-637X/773/1/22

Belskaya, I., Bagnulo, S., Barucci, M., et al. 2010, Icarus, 210, 472. http://doi.org/10.1016/j.icarus.2010.06.005http://linkinghub.elsevier.com/retrieve/pii/S0019103510002277

Benedetti-Rossi, G., Sicardy, B., Buie, M. W., et al. 2016, The Astronomical Journal, 152, 156. http://doi.org/10.3847/0004-6256/152/6/156

Bérard, D., Sicardy, B., Camargo, J. I. B., et al. 2017, Astrophysical Journal (submitted), arXiv:1706.00207. http://arxiv.org/abs/1706.00207

Braga-Ribas, F., Sicardy, B., Ortiz, J. L. J., et al. 2013, The Astrophysical Journal, 773, 26. http://doi.org/10.1088/0004-637X/773/1/26

Braga-Ribas, F., Sicardy, B., Ortiz, J. L., et al. 2014, Nature, 508, 72. http://doi.org/10.1038/nature13155

Bramich, D. M. 2008, Monthly Notices of the Royal Astronomical Society: Letters, 386, L77. http://dx.doi.org/10.1111/j.1745-3933.2008.00464.x

Britt, D. T., Yeomans, D., Housen, K., & Consolmagno, G. 2002, in Asteroids III, ed. W. F. J. Bottke, A. Cellino, P. Paolicchi, & R. P. Binzel (Tucson: University of Arizona Press), 485–500. http://adsabs.harvard.edu/abs/2002aste.book..485B

Brown, M. E. 2013, The Astrophysical Journal, 767, L7. http://doi.org/10.1088/2041-8205/767/1/L7

Camargo, J. I. B., Vieira-Martins, R., Assafin, M., et al. 2014, Astronomy & Astrophysics, 561, A37. http://doi.org/10.1051/0004-6361/201322579

Carry, B. 2012, Planetary and Space Science, 73, 98. http://doi.org/10.1016/j.pss.2012.03.009

Castillo-Rogez, J., Matson, D., Sotin, C., et al. 2007, Icarus, 190, 179. http://doi.org/10.1016/j.icarus.2007.02.018

Castillo-Rogez, J. C., Johnson, T., Thomas, P., et al. 2012, Icarus, 219, 86. http://dx.doi.org/10.1016/j.icarus.2012.02.002

Chandrasekhar, S. 1960, Radiative Transfer (New York: Dover Publications), 393
—. 1987, Ellipsoidal figures of equilibrium (New York: Dover Publications), 264
Cuzzi, J., Clark, R., Filacchione, G., et al. 2009, Ring Particle Composition and Size Distribution, ed. M. Dougherty, L. Esposito, & S. Krimigis (Dordrecht: Springer Netherlands), 459–509. http://dx.doi.org/10.1007/978-1-4020-9217-6{_}15
Davies, J. K., McBride, N., Ellison, S. L., Green, S. F., & Ballantyne, D. R. 1998, Icarus, 134, 213. http://doi.org/10.1006/icar.1998.5931
Desmars, J., Camargo, J. I. B., Braga-Ribas, F., et al. 2015, Astronomy & Astrophysics, 584, A96. http://doi.org/10.1051/0004-6361/201526498http://www.aanda.org/10.1051/0004-6361/201526498
Dias-Oliveira, A., Sicardy, B., Ortiz, J. L., et al. 2017, The Astronomical Journal, 154, 22. https://doi.org/10.3847/1538-3881/aa74e9
Duffard, R., Pinilla-Alonso, N., Ortiz, J. L., et al. 2014, Astronomy & Astrophysics, 568, A79. http://doi.org/10.1051/0004-6361/201424208
Elliot, J. L., French, R. G., Meech, K. J., & Elias, J. H. 1984, The Astronomical Journal, 89, 1587. http://doi.org/10.1086/113662
Elliot, J. L., Person, M. J., Zuluaga, C. A., et al. 2010, Nature, 465, 897. http://www.nature.com/doifinder/10.1038/nature09109
Fernandez-Valenzuela, E., Ortiz, J. L., Duffard, R., Morales, N., & Santos-Sanz, P. 2016, Monthly Notices of the Royal Astronomical Society, 13, stw3264. http://dx.doi.org/10.1093/mnras/stw3264
Foreman-Mackey, D., Hogg, D. W., Lang, D., & Goodman, J. 2013, Publications of the Astronomical Society of the Pacific, 125, 306. http://doi.org/10.1086/670067
Fornasier, S., Lazzaro, D., Alvarez-Candal, A., et al. 2014, Astronomy & Astrophysics, 568, L11. http://doi.org/10.1051/0004-6361/201424439http://www.aanda.org/10.1051/0004-6361/201424439
Gaia Collaboration, Brown, A. G. A., Prusti, T., et al. 2016a, Astronomy & Astrophysics, 595, A1. http://dx.doi.org/10.1051/0004-6361/201629272
Gaia Collaboration, Lindegren, L., Lammers, U., et al. 2016b, Astronomy & Astrophysics, 595, A2. http://dx.doi.org/10.1051/0004-6361/201629512
Galiazzo, M., Marcos, C. d. l. F., Marcos, R. d. l. F., et al. 2016, Astrophysics and Space Science, 361, 212. http://doi.org/10.1007/s10509-016-2801-5
Goodman, J., & Weare, J. 2010, Communications in Applied Mathematics and Computational Science, 5, 65. http://doi.org/10.2140/camcos.2010.5.65
Gregory, P. 2005, Bayesian Logical Data Analysis for the Physical Sciences: A Comparative Approach with Mathematica Support, 1st edn. (Cambridge: Cambridge University Press), 488. http://www.cambridge.org/9780521841504
Guilbert-Lepoutre, a. 2011, The Astronomical Journal, 141, 103. http://doi.org/10.1088/0004-6256/141/3/103
Jewitt, D., & Kalas, P. 1998, The Astrophysical Journal, 499, L103. http://doi.org/10.1086/311356
Karkoschka, E. 2001, Icarus, 151, 51. http://doi.org/10.1006/icar.2001.6596
Kervella, P., Th?venin, F., Di Folco, E., & S?gransan, D. 2004, Astronomy & Astrophysics, 426, 297. http://doi.org/10.1051/0004-6361:20035930
Lellouch, E., Moreno, R., & Muller, T. 2017, in preparation
Ortiz, J. L., Sicardy, B., Braga-Ribas, F., et al. 2012, Nature, 491, 566. http://dx.doi.org/10.1038/nature11597
Peixinho, N., Lacerda, P., Ortiz, J. L., et al. 2001, Astronomy & Astrophysics, 371, 753. http://doi.org/10.1051/0004-6361:20010382
Schindler, K., Wolf, J., Bardecker, J., et al. 2017, Astronomy & Astrophysics, 600, A12. http://dx.doi.org/10.1051/0004-6361/201628620
Sekiguchi, T., Ootsubo, T., Hasegawa, S., et al. 2012, in LPI Contributions, Vol. 1667, Asteroids, Comets, Meteors 2012 (LPI), 6477. http://adsabs.harvard.edu/abs/2012LPICo1667.6477S

Sicardy, B., Colas, F., Maquet, L., et al. 2010, in Bulletin of the American Astronomical Society, Vol. 42, AAS/Division for Planetary Sciences Meeting Abstracts #42 (Washington, DC: American Astronomical Society), 993. http://adsabs.harvard.edu/abs/2010DPS....42.2311S

Sicardy, B., Ortiz, J. L., Assafin, M., et al. 2011, Nature, 478, 493. http://doi.org/10.1038/nature10550

Thomas, P. C. 1989, Icarus, 77, 248. http://doi.org/10.1016/0019-1035(89)90089-4

Tody, D. 1986, in IN Instrumentation in astronomy VI Proceedings of the Meeting, ed. D. Crawford, Vol. 627 (Bellingham: SPIE), 733–748. http://adsabs.harvard.edu/abs/1986SPIE..627..733T

Widemann, T., Sicardy, B., Dusser, R., et al. 2009, Icarus, 199, 458. http://doi.org/10.1016/j.icarus.2008.09.011

Zacharias, N., Monet, D., Levine, S., et al. 2004, in Bulletin of the American Astronomical Society, Vol. 36, American Astronomical Society Meeting Abstracts (Washington, DC: American Astronomical Society), 1418. http://adsabs.harvard.edu/abs/2004AAS...205.4815Z

**Table 1.** Observations used to constrain Chariklo's main body

| Site | Latitude<br>Longitude<br>Altitude (m) | Telescope aperture (m)<br>Camera,Filter<br>Exp. time, cycle (s) | Observers |
|---|---|---|---|
| **2014 April 29. South Africa.** | | | |
| Springbok | 29° 39' 40.2"S | 0.3 | F. Colas |
| South Africa | 17° 52' 58.8"W | Raptor Merlin 247,Clear | C. de Witt |
| | 951 | 0.06, 0.06 | |
| Gifberg | 31°48'34.6"S | 0.3 | J.-L. Dauvergne |
| South Africa | 18°46'59.4"E | Merlin,Clear | P. Schoenau |
| | 345 | 0.05, 0.05 | |
| South African Astronomical | 32°22'46.0"S | 1.9 | H. Breytenbach |
| Observatory, Sutherland (SAAO) | 20°48'38.5"E | SHOC,Clear | A. A. Sickafoose |
| South Africa | 1760 | 0.0334,0.04 | |
| **2014 June 28. South Africa and Namibia.** | | | |
| Kalahari Trails | 26° 46' 27"S | 0.3 | L. Maquet |
| South Africa | 20° 37' 55"E | Merlin, Clear | |
| | 860 | 0.4, 0.4 | |
| Twee Rivieren | 26°28'14"S | 0.3 | J.-L. Dauvergne |
| South Africa | 20°36'42"E | Merlin,Clear | |
| | 885 | 0.4, 0.4 | |
| IAS-Observatory | 23°14'10"S | 0.51 | K.-L. Bath |
| Hakos | 16°21'42"E | Merlin,Clear | |
| Namibia | 1695 | 0.2, 0.2 | |
| **2016 August 8. Namibia.** | | | |
| Windhoek | 22° 41' 54.9"S | 0.35 | H.-J. Bode |
| Namibia | 17° 6' 32.4"E | ZWO ASI120MM,Clear | |
| | 1900 m | 1, 1 | |
| **2016 October 1. Australia.** | | | |
| The Heights Observatory | 34° 48' 44.7"S | 0.3 | A. Cool |
| Adelaide | 138° 40' 56.9"E | QHY5L-II, Clear | B. Lade |
| Australia | 100 m | 1, 1 | |
| Rockhampton | 23° 16' 9.6"S | 0.3 | S. Kerr |
| Australia | 150° 30' 0.7"E | Watec 910BD,Clear | |
| | 50 m | 0.32, 0.32 | |

Note— The stations considered here involve occultation by Chariklo's main body where Chariklo's rings were simultaneously detected. In those cases, the general geometry of the system can be constrained including the apparent center and orientation of the pole axis. The Springbok and Hakos stations provided negative results (that is, no occultation by the body) but which occultation chords are sufficiently close to Chariklo's main body giving strong constrains in the extension of it (see Figure 4). For the same reasons, we consider in this analysis the observations from Danish and PROMPT telescopes (body detections) as well as Ponta Grossa and Cerro Burek (no occultation by the body) of the occultation of 2013 June 3. Circumstances of the these observations are given in Braga-Ribas et al. (2014).

**Table 2.** Coordinates of Chariklo and the occulted star.

| | 2014 Apr 29 | | 2014 Jun 28 | 2016 Aug 8 | 2016 Oct 1 |
|---|---|---|---|---|---|
| $\alpha$ | [a] $17^h39^m2.1336^s$ | -10.1 mas [b] | $17^h24^m50.3800^s$ | $18^h18^m3.6927^s$ | $18^h16^m20.0796^s$ |
| $\delta$ | [a] -38°52'48.802" | -17.8 mas [b] | -38°41'5.618" | -33°52'28.3920" | -33° 1' 10.756" |
| V | ... | ... | 15.20 | 14.06 | 14.33 |
| K | ... | ... | 12.47 | 12.1 | 13.253 |
| $\theta_{LD}$ (mas) | ... | ... | 0.011±0.005 | 0.015±0.003 | 0.007±0.002 |
| $D_{star}$ (km) | 0.2±0.02 [c] | 0.09± 0.02 [c] | 0.11±0.05 | 0.16±0.03 | 0.08±0.02 |
| $t_{ref}$ UTC | 23:10:00 | | 22:24:00 | 19:57:00 | 10:10:00 |
| $\alpha_{Ch}$ | $17^h39^m2.1566^s$ | | $17^h24^m50.3991^s$ | $18^h18^m3.6908^s$ | $18^h16^m20.0982^s$ |
| $\delta_{Ch}$ | -38°52'48.739" | | -38°41'5.628" | -33°52'28.241" | -33°1'10.8424" |
| $d_{Ch}$ (km) | $2.109\times10^9$ | | $2.075\times10^9$ | $2.193\times10^9$ | $2.319\times10^9$ |

NOTE— $(\alpha,\delta)$ are the right ascension and declination of the occulted star, while $d_{Ch}$ is Chariklo's geocentric range and $(\alpha_{Ch},\delta_{Ch})$ the predicted Chariklo's right ascension and declination at the reference time $t_{ref}$. V, K are the star magnitudes from NOMAD catalog (Zacharias et al. 2004). $\theta_{LD}$ is stellar angular diameter, while $D_{star}$ is the stellar diameter projected at the distance of Chariklo, from V-K relations in Kervella et al. (2004) after considering galactic reddening. For the stellar occultation of 2013 June 3 we adopted values from (Braga-Ribas et al. 2014, Supplementary information)

[a] Primary component of double star.

[b] Offset of the secondary component with respect to primary.

[c] Fitting atmospheric models to primary and secondary stars, for details see Bérard et al. 2017.

**Table 3.** Occultation data used to constrains Chariklo's size and shape.

| Site | ing/egr | UTC time | f (km) | g (km) | $\sigma_{ch}$(km) [d] |
|---|---|---|---|---|---|
| 2013 June 3. South America. | | | | | |
| Pta. Grossa [a] | No body detection | | | | |
| Danish | ing | 6:25:27.893±0.014 s | -2750.6 | 920.2 | 0.3 |
| Danish | egr | 6:25:33.188±0.014 s | -2635.3 | 898.2 | 0.3 |
| PROMPT[a] | ing | 6:25:24.835±0.009 s | -2842.0 | 837.7 | 0.2 |
| PROMPT | egr | 6:25:35.402±0.015 s | -2613.3 | 794.2 | 0.3 |
| Cerro Burek [a] | No body detection | | | | |
| 2014 April 29. South Africa. | | | | | |
| Springbok [b] | No body detection | | | | |
| Springbok [c] | ing | 23:14:30.04±0.07 s | -2887.6(-2782.6) | 321.0(503.0) | 0.9 |
| Springbok [c] | egr | 23:14:48.05±0.07 s | -2651.3(-2546.3) | 373.2(555.2) | 0.9 |
| 2014 June 28 South Africa and Namibia | | | | | |
| Hakos | No body detection | | | | |
| Kalahari | ing | 22:24:07.48±0.20 s | -878.6 | 1306.6 | 4.4 |
| Kalahari | egr | 22:24:14.86±0.07 s | -723.2 | 1264.2 | 1.5 |
| Twee Rivieren | ing | 22:24:06.73±0.10 s | -892.6 | 1343.7 | 2.2 |
| Twee Rivieren | egr | 22:24:16.54±0.10 s | -686.3 | 1287.4 | 2.2 |
| 2016 August 8. Namibia. | | | | | |
| Windhoek | ing | 19:57:28.460±0.13 s | 631.1 | -520.5 | 2.1 |
| Windhoek | egr | 19:57:41.870±0.14 s | 831.1 | -599.6 | 2.2 |
| 2016 October 1. Australia. | | | | | |
| Rockhampton | ing | 10:12:44.66±0.04 s | -497.8 | 0.4 | 0.5 |
| Rockhampton | egr | 10:13:03.20±0.06 s | -676.7 | -149.2 | 0.8 |
| Adelaide | ing | 10:10:41.82±0.10 s | -607.9 | 124.1 | 1.3 |
| Adelaide | egr | 10:10:54.16±0.08 s | -726.8 | 25.1 | 1.0 |

NOTE— Here we list only the positive occultations by Chariklo's body and the negative occultations close enough to the body used to constrain Chariklo's size and shape. The second column indicate the detection of the ingress and egress in Chariklo's occultation shadow at each site. The values $(f, g)$ are offset of the star with respect to the expected body center $(f, g) = (0, 0)$ as seen from each site at ingress and egress. Those offsets are measured in the sky plane at Chariklo's distance and are counted respectively positive toward the east and north.

[a] From (Braga-Ribas et al. 2014, extended data table 5).

[b] Occultation of primary star (see text).

[c] Occultation of secondary star (see text).

[d] $\sigma_{ch}$ is the uncertainty in the direction of the occultation chord derived from timing uncertainties.

**Table 4.** Midtime of the occultations by Chariklo's rings.

| Site | ing/egr | $t_{\rm mid}$ UTC | f (km) | g (km) | $v_{ch}$ (km s$^{-1}$) | $\sigma_{ch}$ (km) |
|---|---|---|---|---|---|---|
| 2014 April 29. South Africa. | | | | | | |
| C1R | | | | | | |
| Springbok [a] | ing | 23:14:25.884 ± 0.007 s | -2942.16 | 308.95 | 13.4 | 0.1 |
| Springbok [a] | egr | 23:15:04.362 ± 0.006 s | -2437.27 | 420.48 | 13.4 | 0.1 |
| SAAO [b] | ing | 23:13:56.191 ± 0.007 s | -3017.66 | 56.58 | 13.4 | 0.1 |
| SAAO [b] | egr | 23:14:28.964 ± 0.008 s | -2587.52 | 151.12 | 13.4 | 0.1 |
| C2R | | | | | | |
| Springbok [a] | ing | 23:14:24.990 ± 0.020 s | -2953.89 | 306.36 | 13.4 | 0.3 |
| Springbok [a] | egr | 23:15:05.324 ± 0.019 s | -2424.65 | 423.27 | 13.4 | 0.3 |
| Gifberg [a] | ing | $23{:}14{:}30.109^{+0.015}_{-0.008}$ s | -2742.39 | 137.87 | 13.4 | $^{+0.2}_{-0.1}$ |
| Gifberg [a] | egr | 23:14:33.750 ± 0.008 s | -2694.62 | 148.40 | 13.4 | 0.1 |
| 2014 June 28. Namibia. | | | | | | |
| C1R+C2R unresolved | | | | | | |
| Hakos | ing | 22:24:25.796 ± 0.041 s | -886.44 | 1629.24 | 21.8 | 0.9 |
| Hakos | egr | 22:24:44.218 ± 0.035 s | -498.24 | 1523.61 | 21.8 | 0.8 |
| 2016 August 08. Namibia. | | | | | | |
| C1R+C2R unresolved | | | | | | |
| Windhoek | ing | 19:57:18.209 ± 0.249 s | 478.18 | -459.92 | 16.0 | 4.0 |
| Windhoek | egr | 19:57:51.892 ± 0.109 s | 980.60 | -658.82 | 16.0 | 1.8 |
| 2016 October 1. Australia. | | | | | | |
| C1R+C2R unresolved | | | | | | |
| Rockhampton | ing | 10:12:26.284 ± 0.072 s | -320.56 | 148.77 | 12.6 | 0.91 |
| Rockhampton | egr | 10:13:22.928 ± 0.049 s | -876.01 | -308.47 | 12.6 | 0.62 |
| Adelaide | ing | 10:10:19.826 ± 0.186 s | -396.05 | 300.41 | 12.5 | 2.3 |
| Adelaide | egr | 10:11:14.558 ± 0.218 s | -923.38 | -138.48 | 12.5 | 2.7 |

NOTE— C1R is the internal and wider ring while C2R is the external ring. $t_{\rm mid}$ are the midtimes of the occultations by the rings, from Bérard et al. 2017. Ingress/egress indicates the first and second detection of the respective ring. The values $(f, g)$ are offset of the star with respect to the expected body center $(f, g) = (0, 0)$ as seen from each site derived from the midtimes $t_{\rm mid}$. Those offsets are measured in the sky plane at Chariklo's distance and are counted respectively positive toward the east and north. $v_{ch}$ is the speed of the star relative to Chariklo, projected in the sky plane and $\sigma_{ch}$ is the position uncertainty along the chord direction given by the timing uncertainty.

[a] Occultation of primary star (see text).

[b] Occultation of secondary star (see text).

**Table 5.** Adopted ring geometry.

| | | | | |
|---|---|---|---|---|
| Pole position [a] | $\alpha_P = 151.30° \pm 0.5°$ and $\delta_P = 41.48° \pm 0.2°$ | | | |
| C1R radius[a] (km) | 390.6 ± 3.3 | | | |
| C2R radius [a] (km) | 404.8 ± 3.3 | | | |
| Date | Opening angle - $B$ (°) | Position angle - $P$ (°) | $f_c$ (km) | $g_c$ (km) |
| 2013 Jun 3 [a] | 33.8 ± 0.4 | -61.6 ± 0.1 | -2734.7± 0.5 | 793.8 ± 1.4 |
| 2014 Apr 29 | 40.4 ± 0.4 | -64.5 ± 0.4 | -2669.4± 0.2 | 519.0± 0.1 |
| 2014 Jun 28 | 37.8 ± 0.4 | -63.1 ± 0.4 | -775.3± 0.5 | 1375.8± 0.5 |
| 2016 Aug 8 [b] | 45.2 ± 0.4 | -62.9 ± 0.4 | 767.1(691.7) ± 4.0 | -475.95(-642.8) ± 7.0 |
| 2016 Oct 1 | 44.5 ± 0.4 | -62.0 ± 0.4 | -619.3 ± 1.0 | -17.8 ± 3.4 |

NOTE— Opening angle $B$ is the the elevation of the observer above the ring plane. $P$ is the position angle of the semiminor axis of the ring projected in the sky plane, counted positively from celestial north towards east. With the assumptions used here, $B$ and $P$ corresponds to the planetocentric declination of the Earth and the position angle of the pole axis respectively (see Section 3). $f_c$ and $g_c$ are the coordinates of the center of the ring in the sky plane measured with respect to the expected body center $(f, g) = (0, 0)$.

[a] From Braga-Ribas et al. 2014, ED Table 4

[b] For the occultation of 2016 August 8 there are two possible solutions for the center of the system.

**Table 6.** Rotational light curve amplitudes.

| Date | $\Delta m$ (mag) | B (°) | Reference |
|---|---|---|---|
| 1997 May | <0.02 | -56 | (Davies et al. 1998) |
| 1999 Mar | <0.05 | -53 | (Peixinho et al. 2001) |
| 2006 Jun | 0.13±0.03 | -13 | (Galiazzo et al. 2016) |
| 2013 Jun | 0.11±0.02 | 34 | (Fornasier et al. 2014) |
| 2015 Jul | 0.06±0.02 | 42 | This work |

NOTE— Rotational peak-to-peak amplitude $\Delta_m$ measured for Chariklo at different opening angles $B$. Upper limits for the amplitude in 1997 and 1999, and uncertainties in 2006 and 2013 are estimated from uncertainties in the photometry given by the authors. The amplitude in 2015 is the one obtained from data taken with the SOI camera at SOAR telescope.

**Table 7.** Physical parameters of Chariklo from stellar occultations.

| Parameter | Sphere | Maclaurin | Ellipsoid | Jacobi |
|---|---|---|---|---|
| $\rho$ (kg m$^{-3}$) | ... | $970^{+300}_{-180}$ | ... | $796^{+2}_{-4}$ |
| a (km) | $129 \pm 3$ | $143^{+3}_{-6}$ | $148^{+6}_{-4}$ | $157 \pm 4$ |
| b (km) | $129 \pm 3$ | $143^{+3}_{-6}$ | $132^{+6}_{-5}$ | $139 \pm 4$ |
| c (km) | $129 \pm 3$ | $96^{+14}_{-4}$ | $102^{+10}_{-8}$ | $86 \pm 1$ |
| $R_{\rm equiv}$ (km) | $129 \pm 3$ | $126 \pm 2$ | $126 \pm 2$ | $123^{+3}_{-1}$ |
| $\sigma_m$ (km) | 11 | 7 | 6 | 6 |
| $d_{\rm RMS}$ (km) | 10 | 7 | 5 | 5 |
| $d_{\rm max}$ (km) | +15 | +11 | +12 | +9 |
| Mass (kg) | ... | $8 \pm 1 \times 10^{18}$ | ... | $6.1 \pm 0.1 \times 10^{18}$ |
| $p_b$ (%) | $3.1 \pm 0.1$ | $3.8 \pm 0.1$ | 3.7±0.1 | $4.2 \pm 0.1$ |
| $I/F$ (%) | $8.9 \pm 0.3$ | $3.4 \pm 0.3$ | 4.9±0.3 | $0.6 \pm 0.4$ |

NOTE— Best parameter values and formal uncertainties from 68% credible intervals obtained with prior as defined in Section 3.3.1. See Section 4 for the sensitivity of results to the priors chosen. $d_{\rm RMS}$ is the RMS dispersion in the radial direction with respect to the nominal body limb. $d_{\rm max}$ is the maximum distance in the radial direction with respect to the nominal body limb. $p_b$ is the geometric albedo of the body while $I/F$ is the ring reflectivity considering only the main ring with a width $W$=5.5 km (not to be confused with the geometric albedo of the ring particles $p_p$) as determined in Section 5.2. $R_{\rm equiv}=(a \times b \times c)^{1/3}$ is the volumetric equivalent radius.

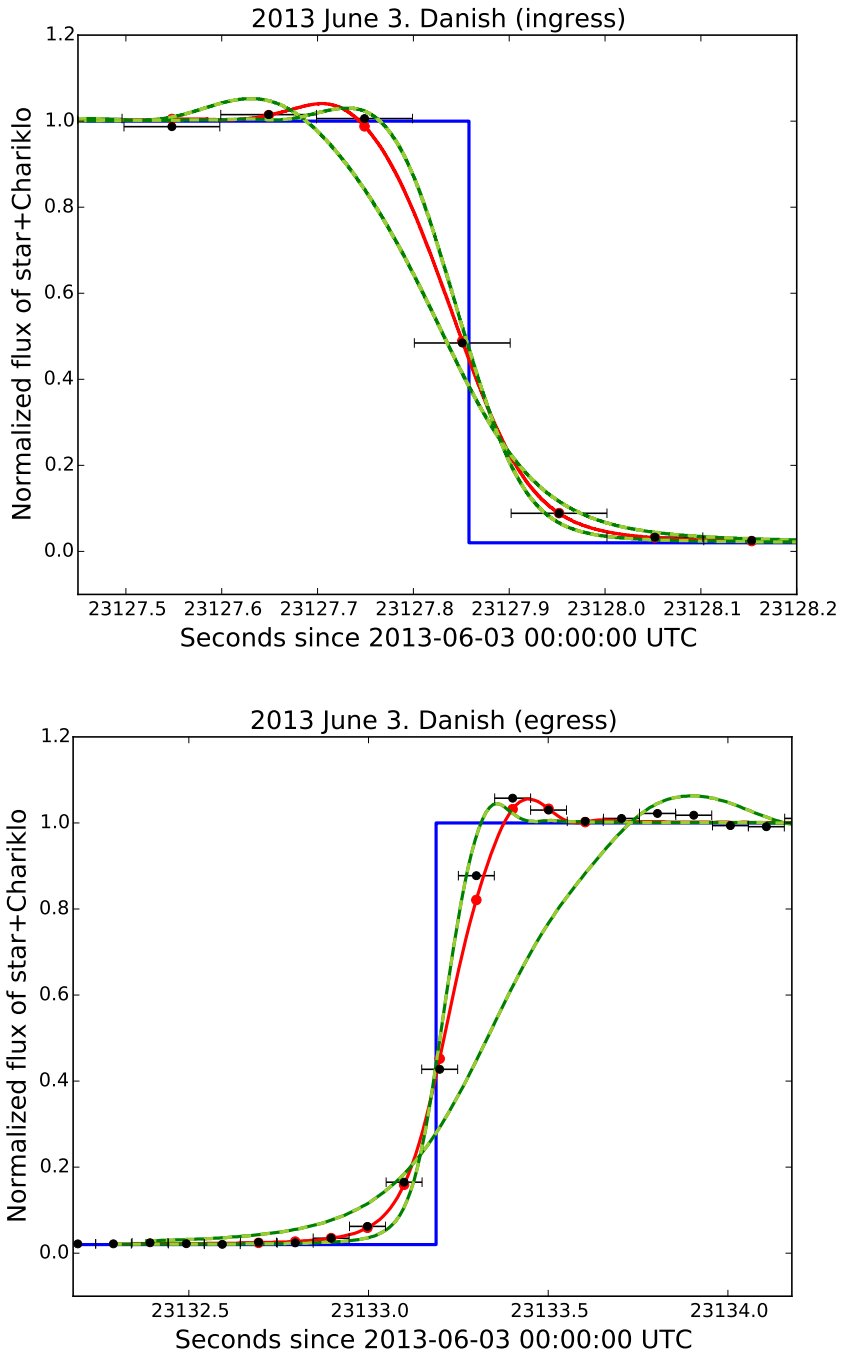


**Figure 1.** Occultation light curve of 2013 June 3 at Danish telescope. Black dots are the data points with horizontal bars indicating the time interval of acquisition (the exposure time). Blue continuous line is the geometric best solution indicating the limb of the object, from where we obtain the occultation times given in Table 3. Red continuous line is the best solution after applying the limb diffraction model. The high SNR and cadence of the light curve from Danish telescope allows to determine the orientation between the occultation chord and the normal to the local limb, given by the angles $\alpha_{\rm ing} = 60^\circ$ and $\alpha_{\rm egr} = 73^\circ$ at ingress and egress respectively (see Figure 3). The red line show the best fitted limb profile model. For illustration, the green lines show the limb profiles for $\pm 10^\circ$ with respect to the best-fit values $\alpha_{\rm ing}$ and $\alpha_{\rm egr}$, showing a clear departure from the data (see Section 2.3 for details).

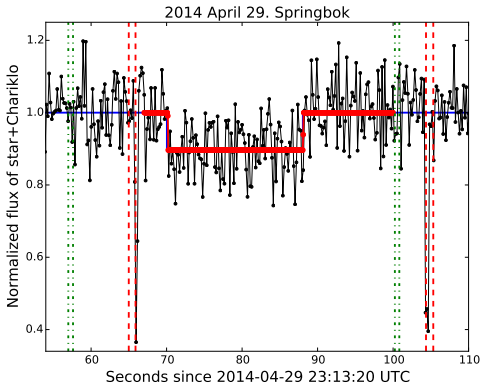


(c)

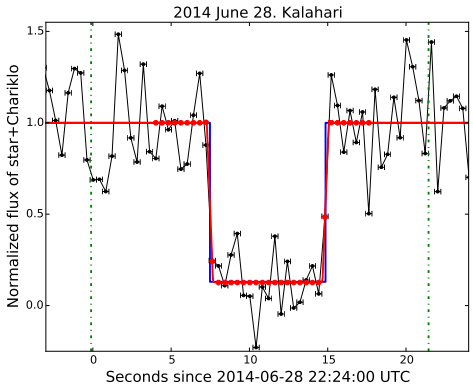


(d)

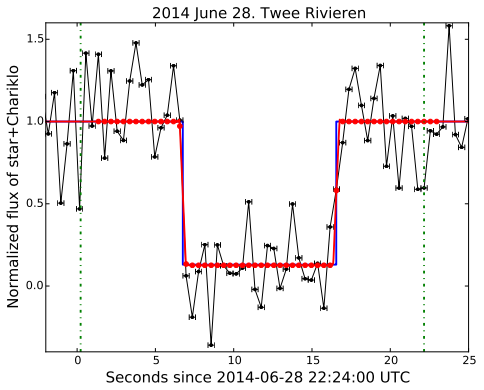


(e)

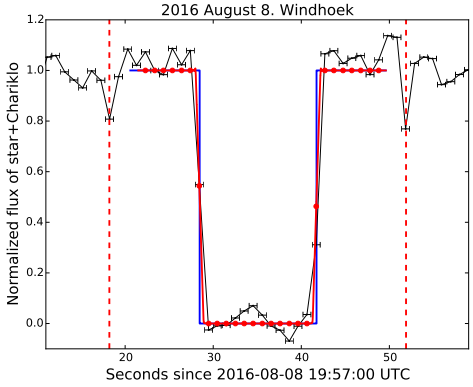


(f)

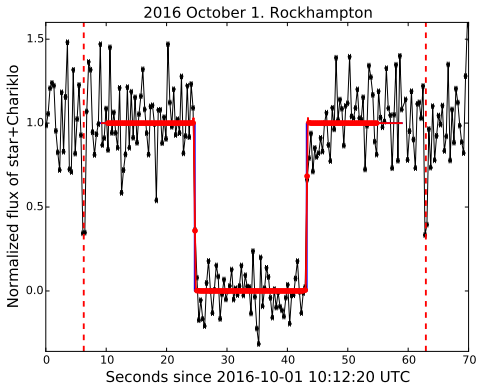


(g)

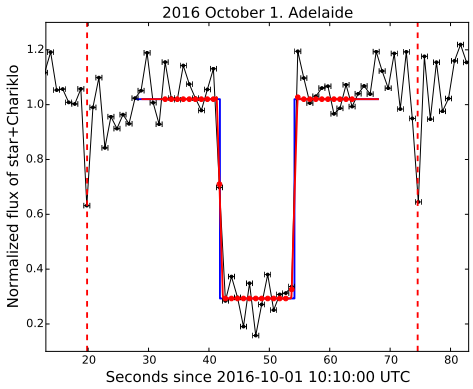


(h)

**Figure 2.** Occultation light curves used in this paper. Black dots are the data points with horizontal bars indicating the time interval of acquisition (the exposure time). Blue continuous lines are the geometric best solution indicating the limb of the object. Red continuous lines are the best solution after applying the limb diffraction model. Red dashed lines show the central times of occultations by C1R and C2R rings. Notice that only the C1R position is indicated for events with unresolved rings. Green dot-dashed lines indicate the ring position expected after reconstruction of the geometry of the event in cases if the rings are undetected.

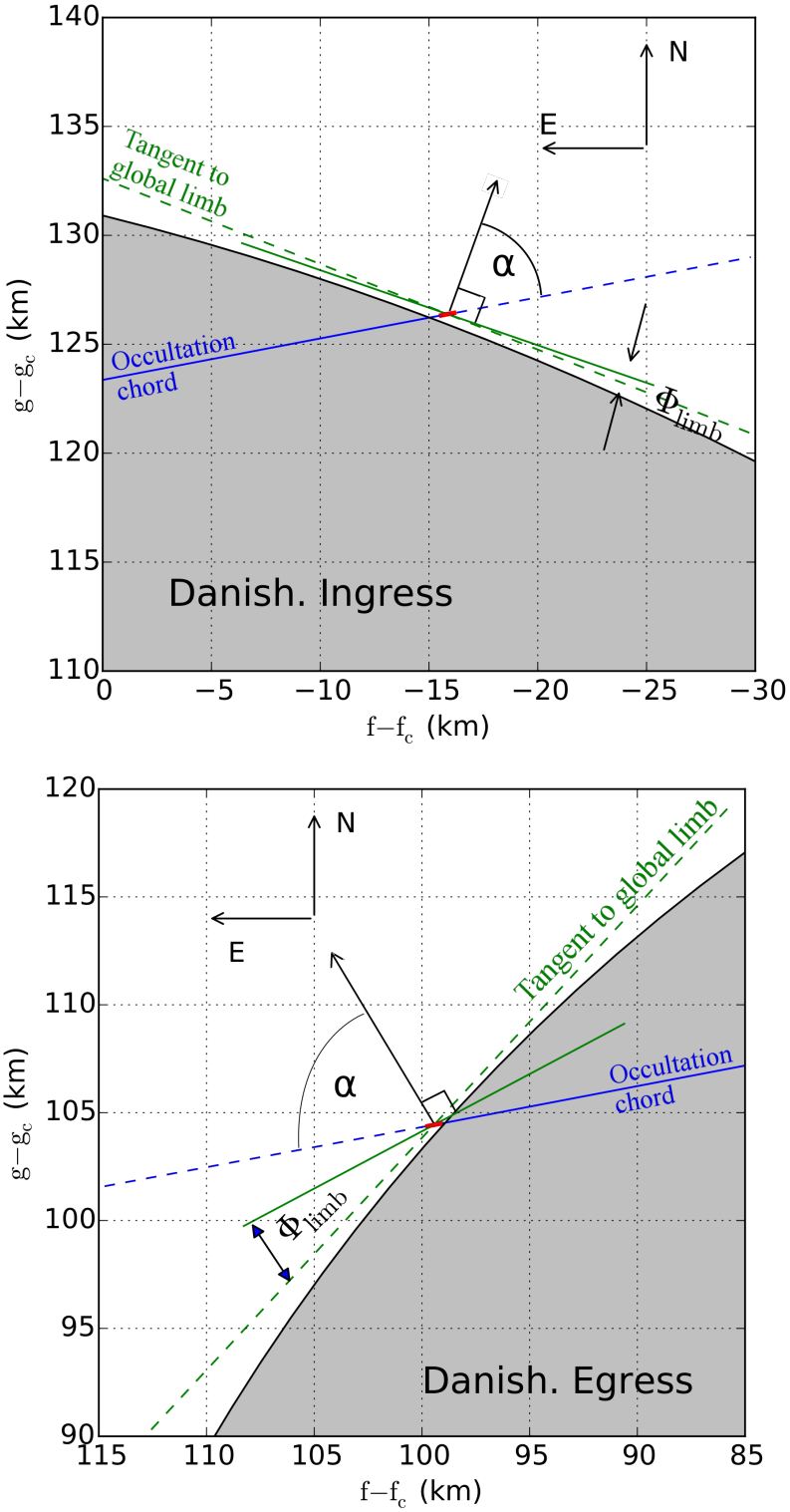


**Figure 3.** Local limb slopes with respect to the generic ellipsoid model as measured at the Danish telescope for the occultation of 2013 June 3. The tangent to local limb (solid green line) is derived from fitting the angle $\alpha$ in the limb diffraction model to the occultation light curves (Figure 1). The blue-solid lines are the occultation chords with their extremities uncertainty in red. Depending on Chariklo's main body model, the slopes with respect to the tangent to the global limb of up to $\Phi_{\rm limb} = 25°$ are observed. As illustration, this figure shows the local limb orientation for the generic ellipsoidal model.

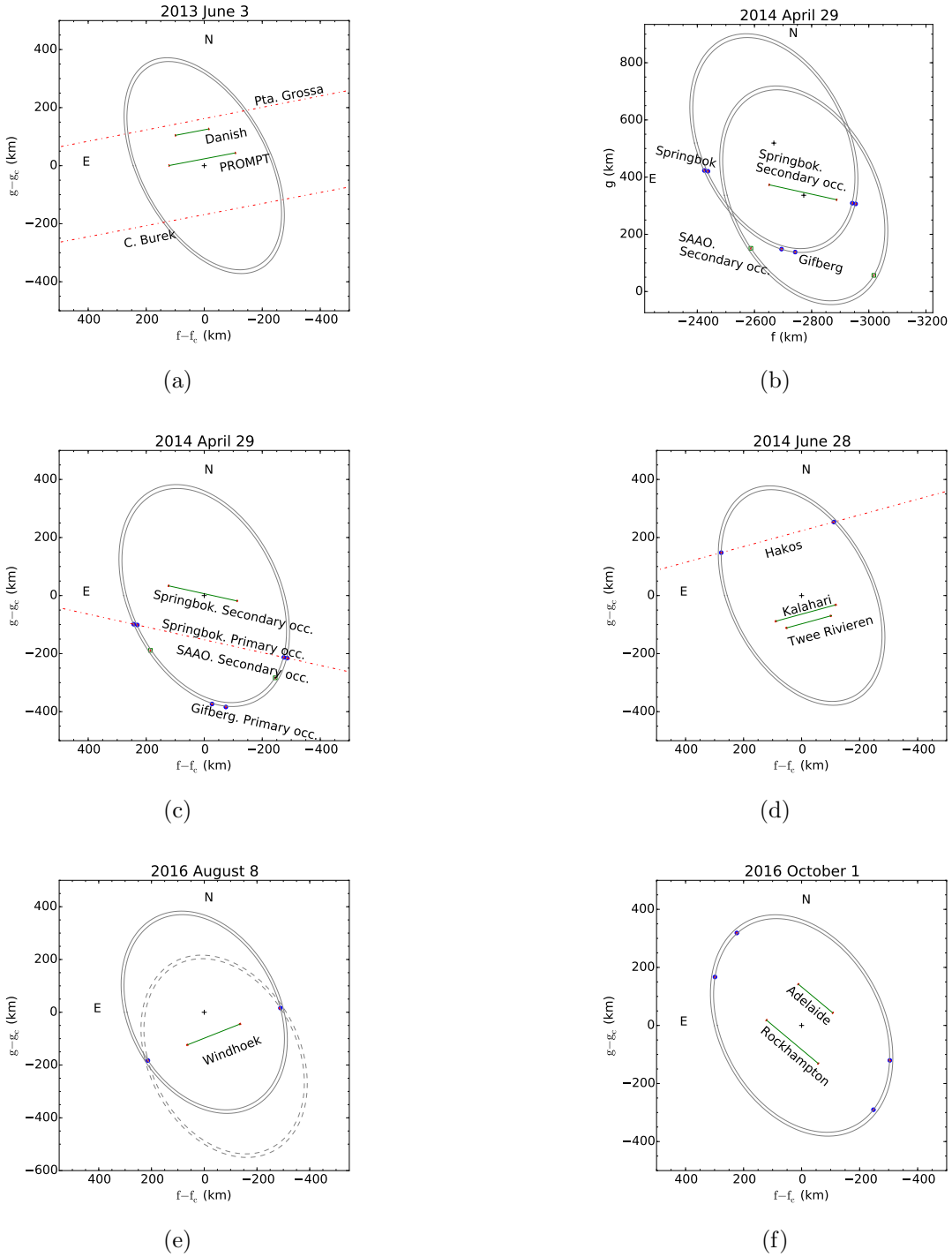


**Figure 4. Geometry for the five occultations by Chariklo's main body between 2013 and 2016.** Positions are given in the sky plane at Chariklo's distance with respect to the center of the system $(f_c, g_c)$ determined in Table 5. The ellipses represent the C1R and C2R orbits adopting the diameter and pole position of Braga-Ribas et al. (2014). Dots indicate the rings detections used to fit the center of the system (black crosses). The continuous green lines are the occultation chords by the main body with uncertainties in red. For clarity we only indicate the closest negative detections in red dot-dashed lines used as constraints. (a) 2013 June 3, South America. (b) 2014 April 29, South Africa. Occultation of a double star. Solid dots and cross are the ring occultation of the primary star and the adopted center of the system. Open dots correspond to occultations of the secondary star. (c) 2014 April 29, South Africa. Geometry after applying an offset of $\Delta f$=103 km and $\Delta g$=182.5 km to the secondary events. (d) 2014 June 28, South Africa - Namibia. (e) 2016 August 8, Namibia. Rings solution 1 in continuous line and solution 2 in dashed lines. (f) 2016 October 1, Australia.

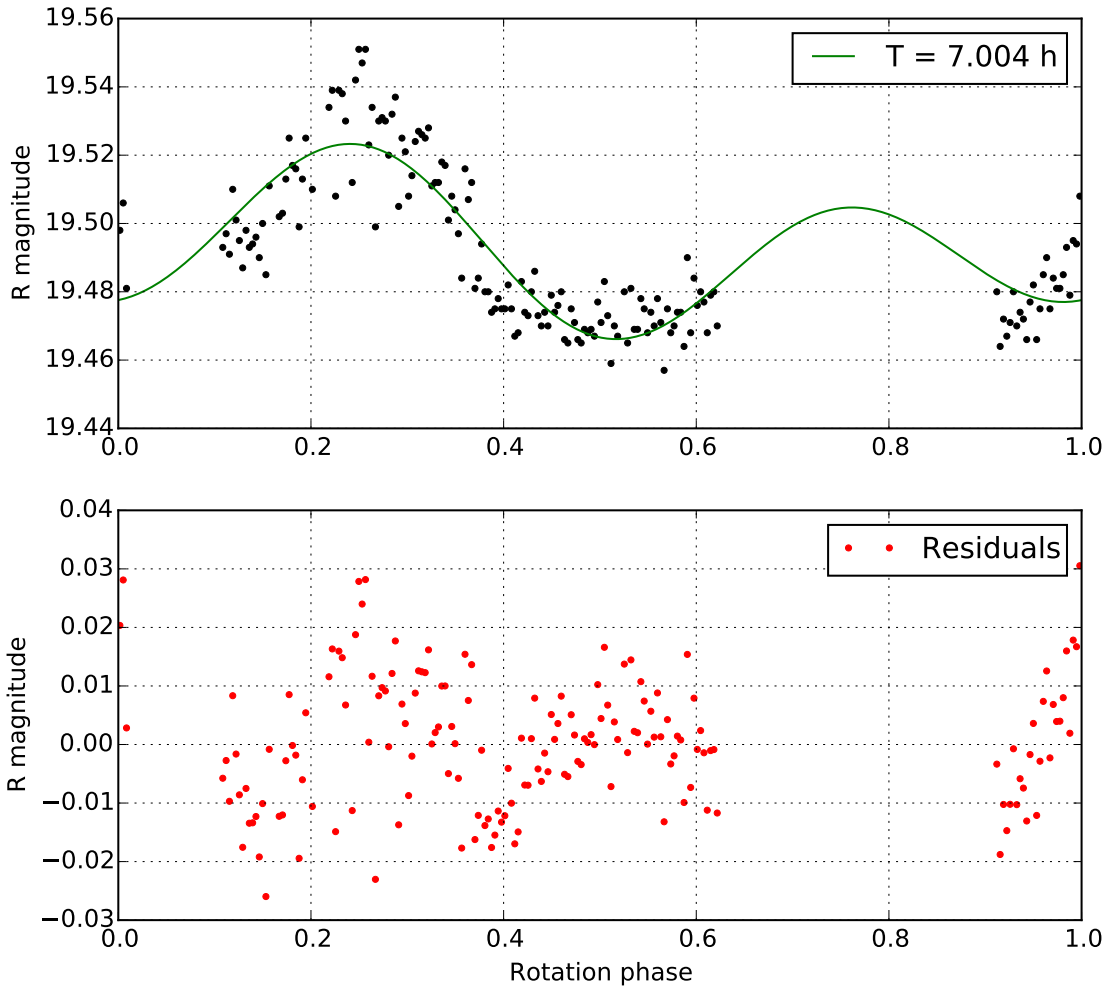


**Figure 5.** Chariklo's rotational light curve obtained on 2015 July 20 with the SOI camera at SOAR telescope. The light curve covers about 5 hours of Chariklo's rotation. The green-solid line is a fit with a second order polynomial after folding the data with a period $T$=7.004 hr from Fornasier et al. (2014). The peak-to-peak amplitude from this light curve is $\Delta m = 0.06 \pm 0.02$ mag. Using the pole position from Table 5, the opening angle of Chariklo's system at this date is $B = 42°$. Together with $\Delta m$ and $H_V$ values from the literature, this is used to derive a prior for the size and shape of the models.

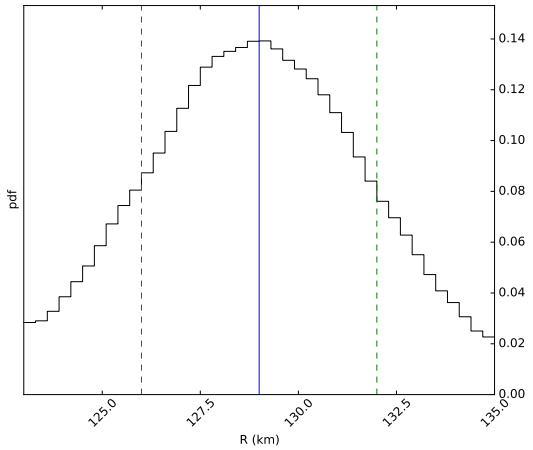


**Figure 6.** Posterior probability function (pdf) for the sphere radius $R$. The blue-continuous line is the best value and the green-dashed lines indicate the 68% credible interval from where we determine the value for $R = 129 \pm 3$ km.

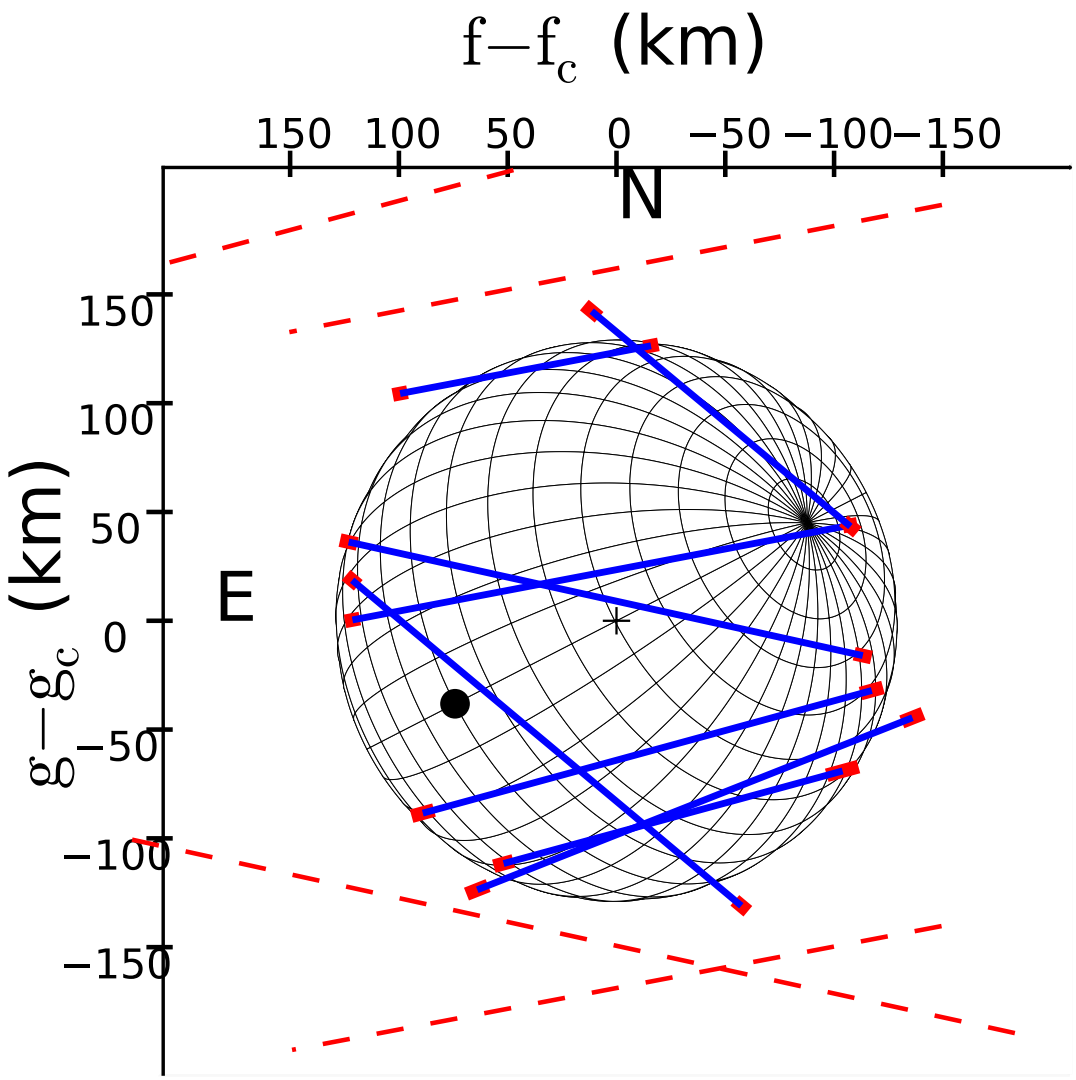


**Figure 7.** The best fit for the sphere model with radius $R = 129 \pm 3$ km compared to all the occultation chords projected in the sky plane. The sphere model is plotted with the average orientation of $B = 40°$ and $P = -63°$. Measurement uncertainties are indicated in red. Red dashed lines outside the body are the multiple negatives detections used to constraint the model. Black dot indicate the sphere's equator.

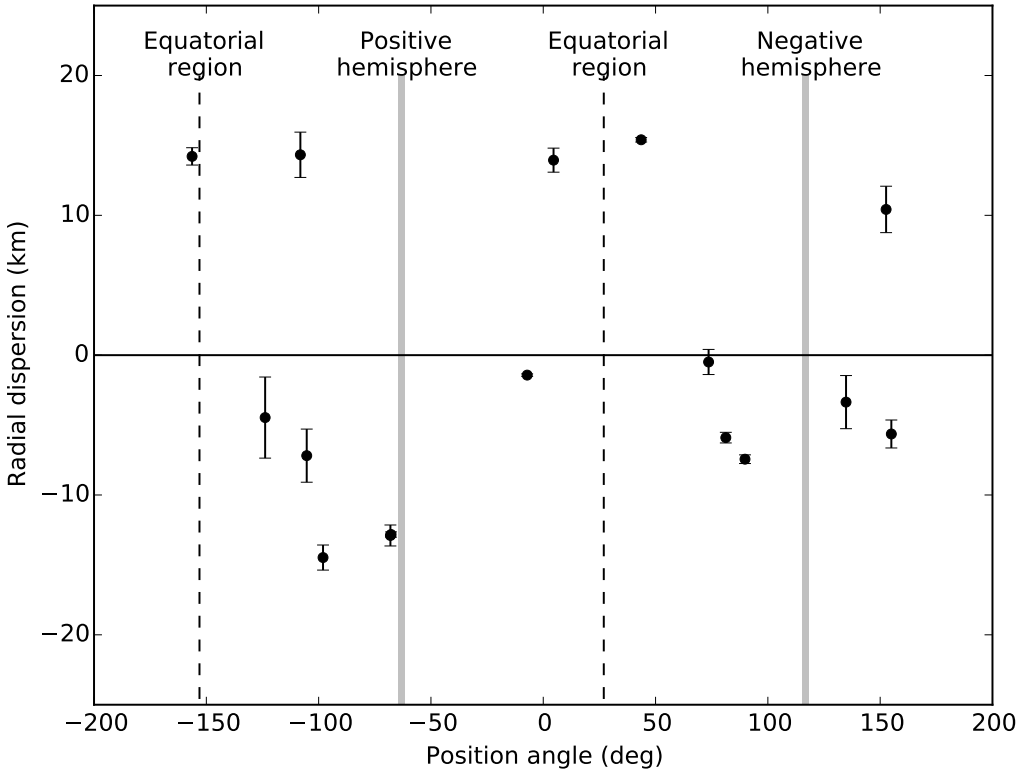


**Figure 8.** Radial residual as a function of position angle (counted positively from celestial north towards east) for the spherical model of Figure 7. Error bars are the uncertainties in the position of the occultation chord extremities projected in the radial direction. Dashed lines indicate the equatorial region while the solid lines indicate the polar region. Positive and negative hemispheres are defined according to the choice of the pole position given in Table 5. A clear correlation between the residual and sub-occultation point latitude is observed (see text for details).

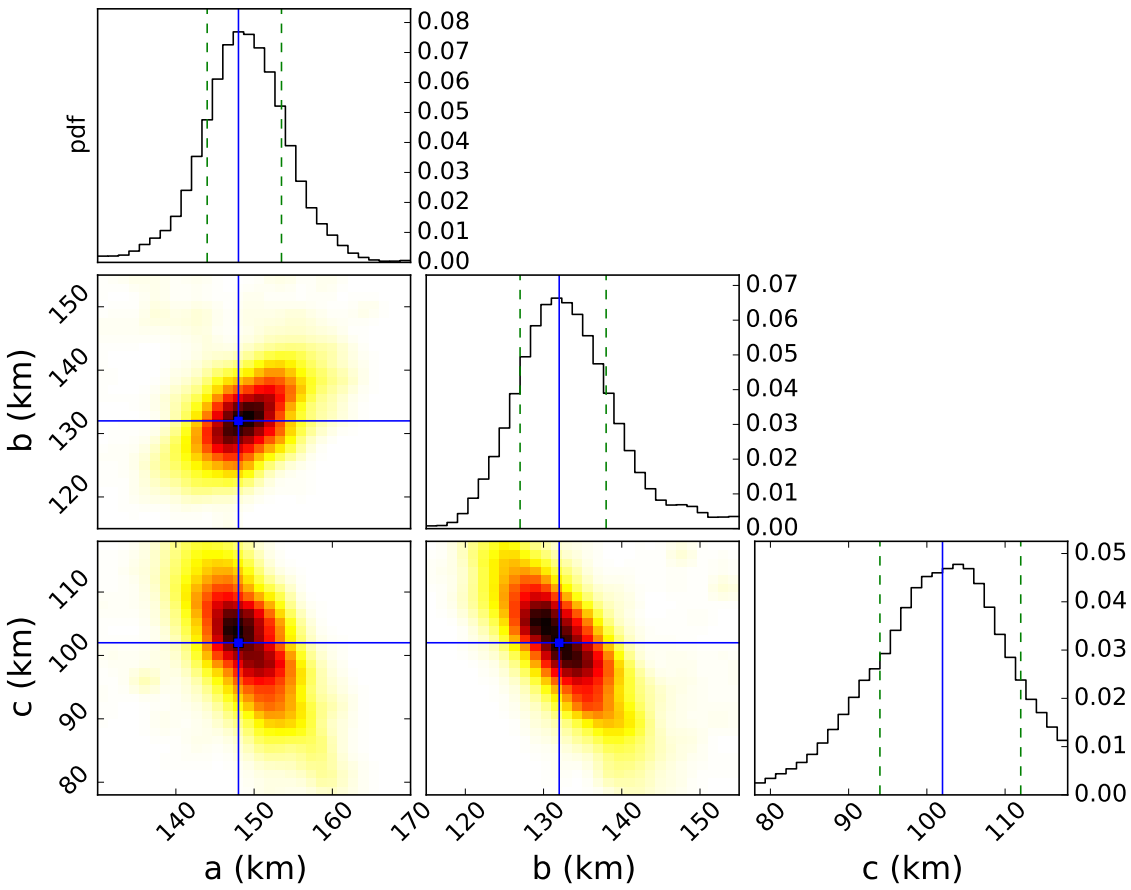


**Figure 9.** Results for the generic triaxial ellipsoid. The plots in the diagonals show the marginal posterior pdf $p(\theta|D)$ (Equation 5) for the semiaxes $a$, $b$ and $c$. The rest of the plots are the joint posterior pdf for $a$ vs $b$ (left-center), $a$ vs $c$ (bottom-left), and $b$ vs $c$ (bottom-center). The blue-continuous lines indicate the best fit values adopted and the green-dashed lines indicate the 68% credible intervals given in Table 7.

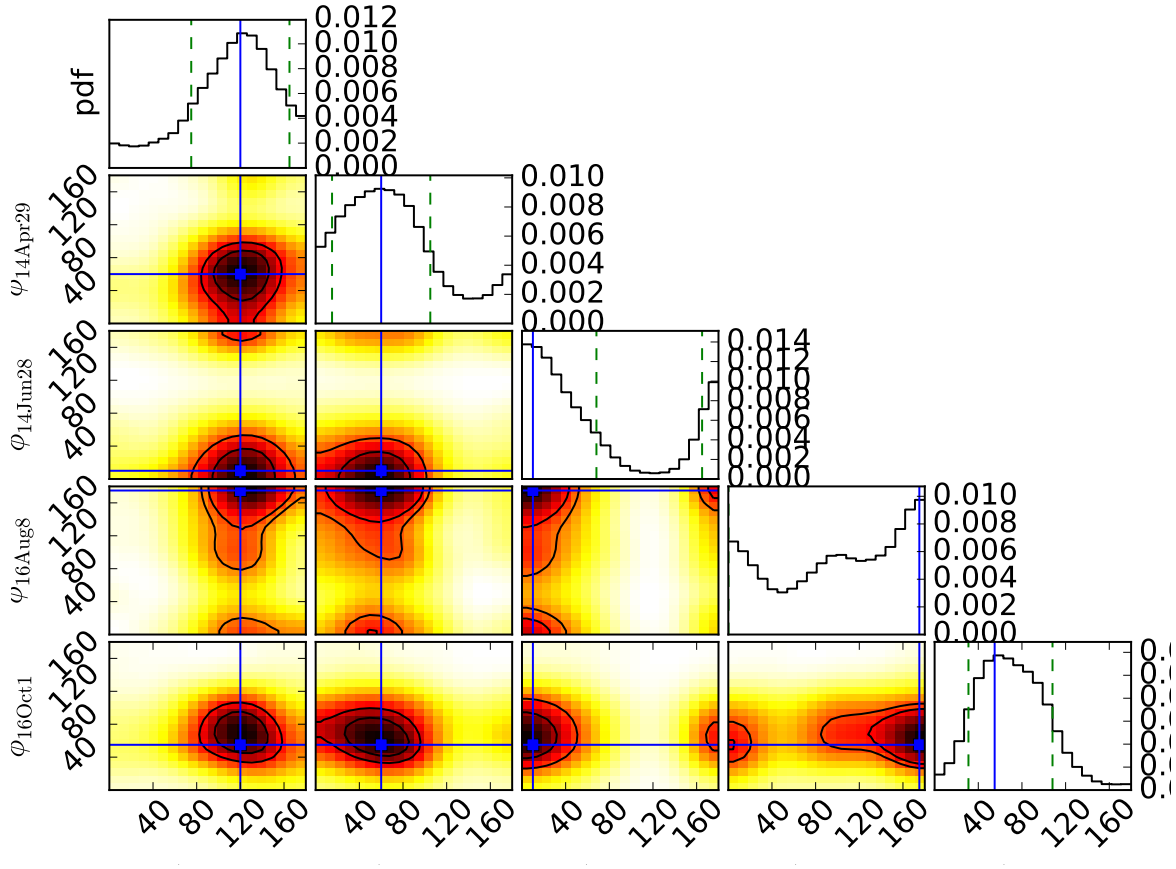


**Figure 10.** Posterior pdf of the rotation angle $\phi$ for each occultation for the generic ellipsoid model. The best fit values used in Figure 11 are indicated by blue dots and lines. Green-dashed lines indicate the 68% credible intervals, except for the occultation of 2016 August 8 where the rotation angle pdf is multimodal.

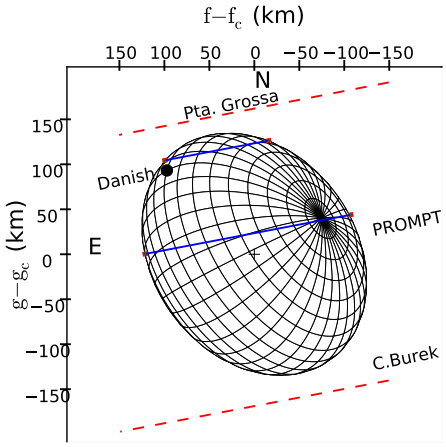


(a) 2013 June 3

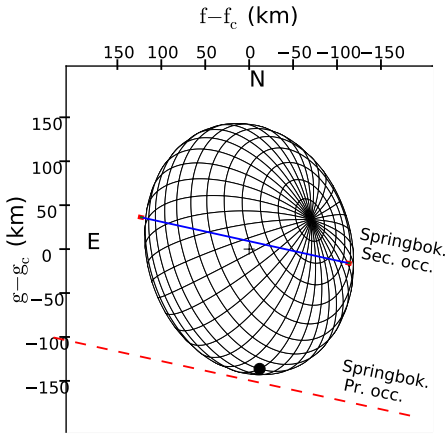


(b) 2014 April 29

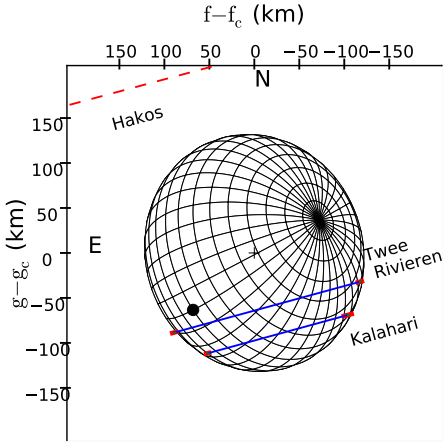


(c) 2014 June 28

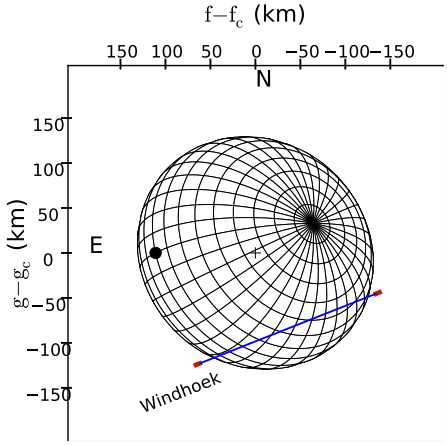


(d) 2016 August 8

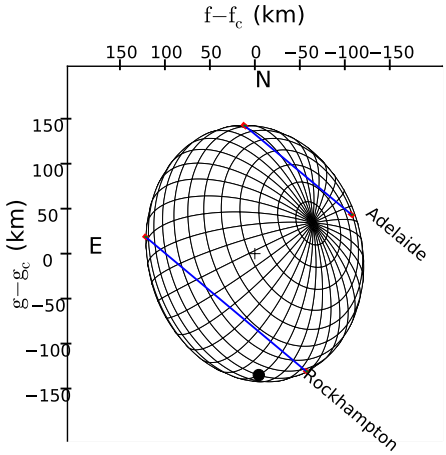


(e) 2016 October 1

**Figure 11.** Results of the triaxial model using the best-fit values in Table 7. At each panel, the body has the same pole position $(\alpha_P, \delta_P)$ and apparent center $(f_c, g_c)$ than the rings (not shown) as given in Table 5. Blue lines are the detections of the main body with uncertainties in red. Red dashed lines are the negative chords closest to the object used as constraints for the body model. The black dot indicates the intersection between the equator and the prime meridian, which is used as reference to define the rotation angle $\phi$.

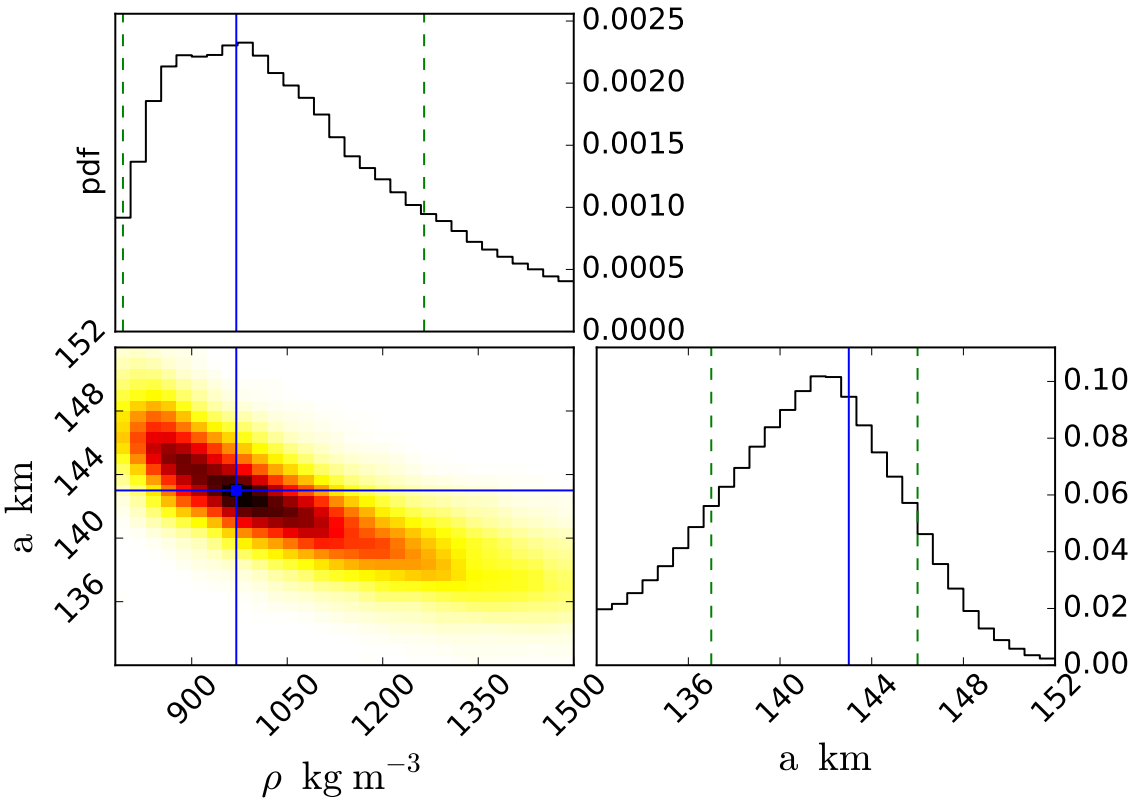


**Figure 12.** Results for the Maclaurin spheroid model. Bottom-left: the joint posterior probability $p(\theta|D)$ (Equation 5) for the density $\rho$ and equatorial radius $a$. Top-left: the marginal posterior probability for the density $\rho$. Bottom-right: the marginal posterior probability for the equatorial radius $a$. The blue-continuous lines indicate the best parameter values and the dashed vertical lines indicate the 68% credible intervals given in Table 7.

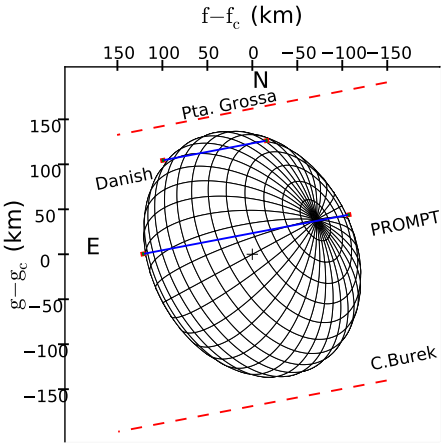


(a) 2013 June 3

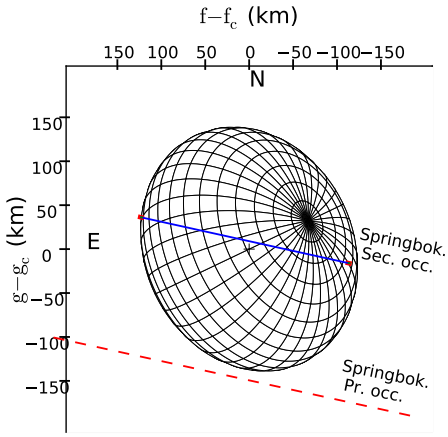


(b) 2014 April 29

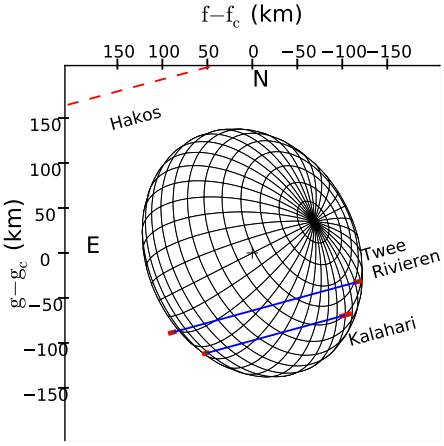


(c) 2014 June 28

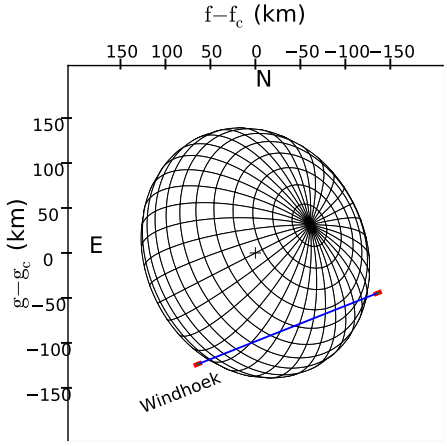


(d) 2016 August 8

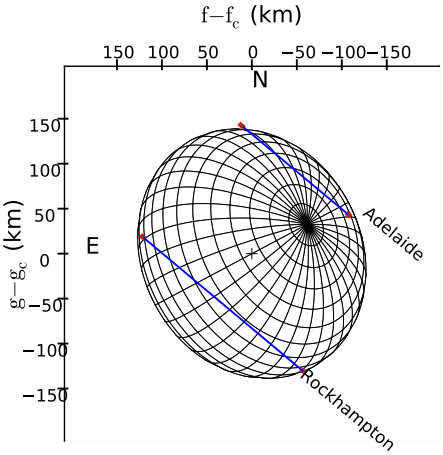


(e) 2016 October 1

**Figure 13.** Same as Figure 11 for the Maclaurin model using the best-fit values in Table 7.

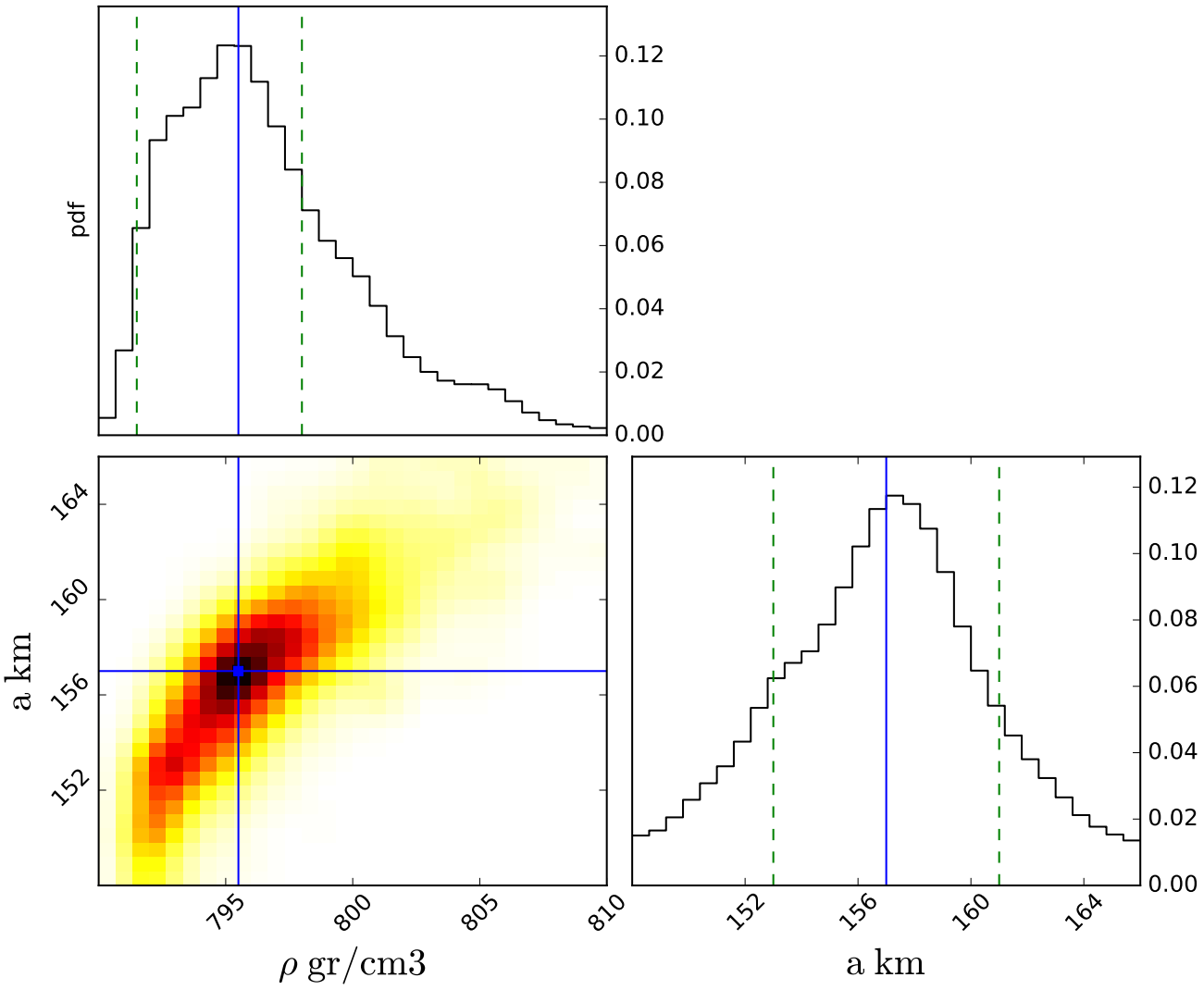


(b)

**Figure 14.** Same as Figure 12 for the Jacobi ellipsoid model, from where we obtain the parameter values given in Table 7.

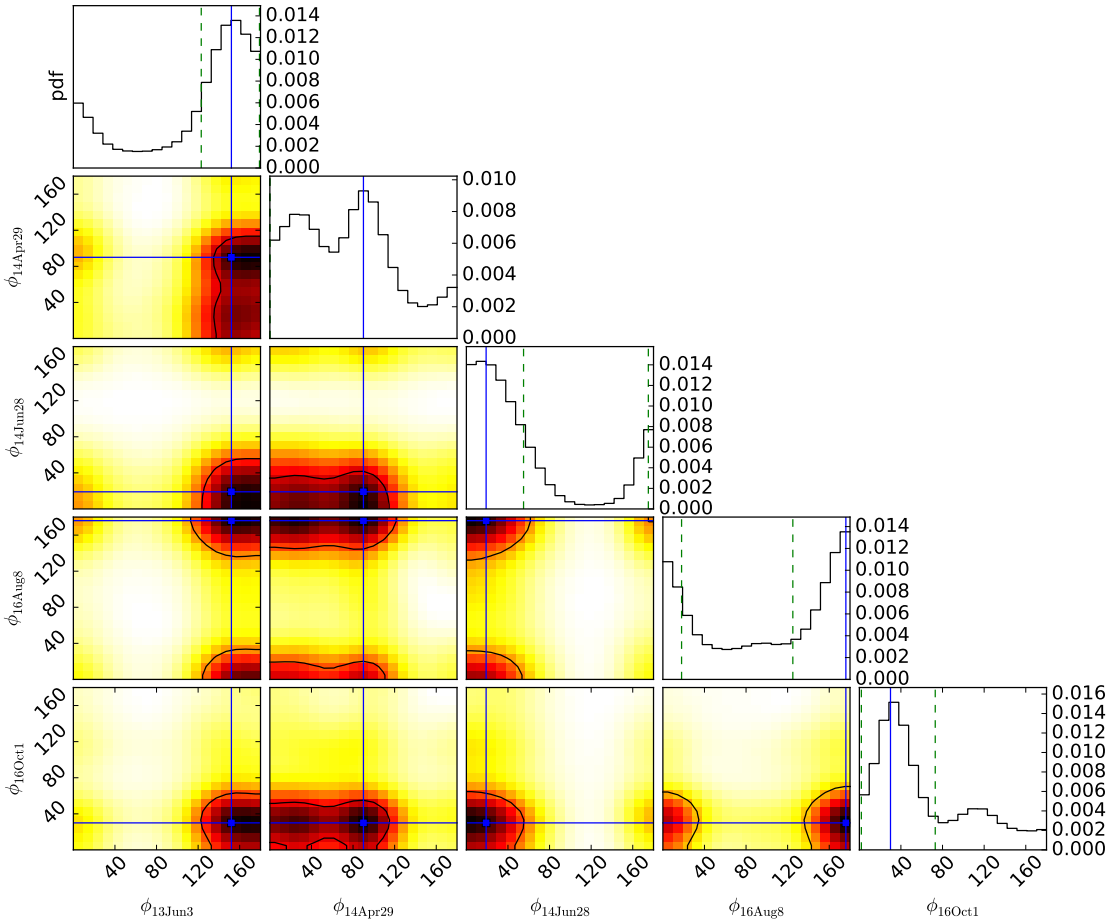


**Figure 15.** Posterior probability of relative rotation angle $\phi$ for each occultation. The best fit values used in Figure 16 are indicated by blue dots and lines.

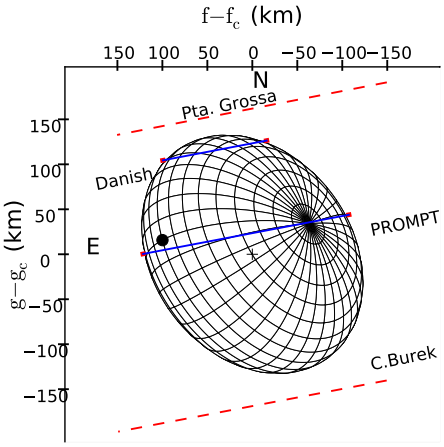


(a) 2013 June 3

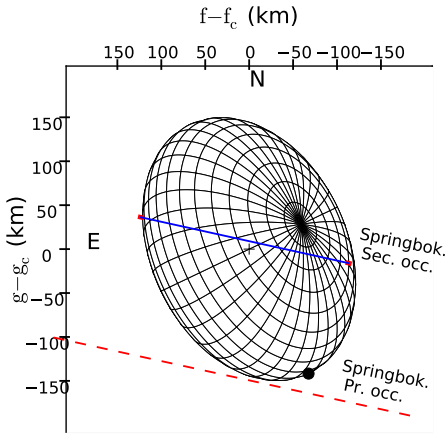


(b) 2014 April 29

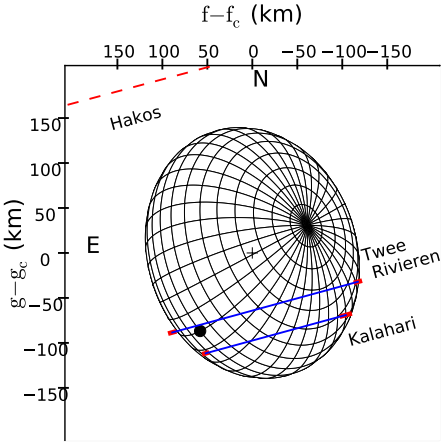


(c) 2014 June 28

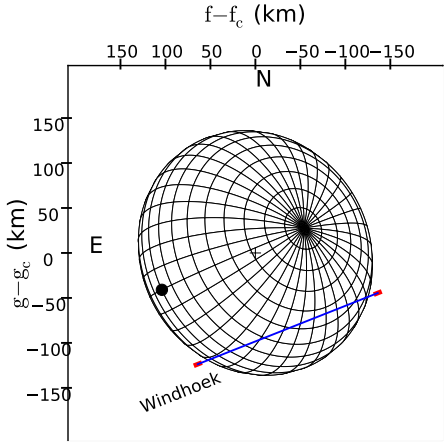


(d) 2016 August 8

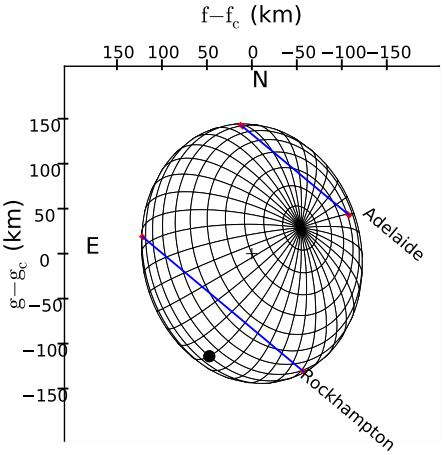


(e) 2016 October 1

**Figure 16.** Same as Figure 11 for the Jacobi model with the best fit values from Table 7.

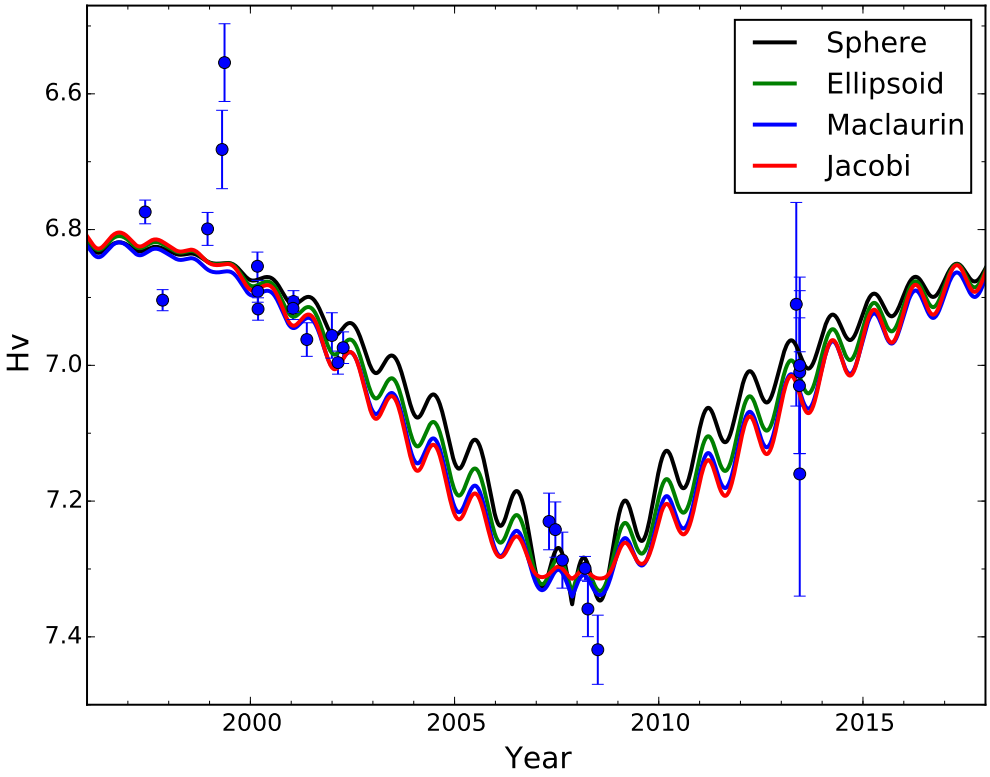


**Figure 17.** Best fit to the V absolute magnitude $H_V$ of Chariklo's system. The main body geometric albedo $p_b$ and ring reflectivity $I/F$ are fitted with a least-squares to the $H_V$ values from the literature (Belskaya et al. 2010; Fornasier et al. 2014; Duffard et al. 2014). In the extreme case of the spherical model, all the brightness variation is due to the change in the rings aspect angle, with $I/F$=8.9%. On the other hand, the change in the projected area of the Jacobi model explains most of the long-term brightness variations, resulting in very dark rings with $I/F$=0.6%. The Maclaurin and generic triaxial ellipsoid models give intermediate results (Table 7). With both contributions, from the main body and rings considered, all the models fit equally well the $H_V$ values.

# Chapter 4

# The dynamics of rings around a non-spherical body

In the Introduction, we presented an overview of Chariklo's system, mentioning the existence of two dense and narrow rings around that Centaur object. Detecting such features around a small body probably means that they are more common than previously thought. This means that Chariklo could be an example – among others – of a small body surrounded by rings.

A striking characteristic of Chariklo's rings (in particular the main one, C1R, see Bérard et al. 2017) is the resemblance they bear with the Uranian rings (French et al., 1991): they are narrow (a few kilometers to a few tens kilometers of in width), dense (almost opaque in some parts), and sharply confined (their edges are well defined to within a kilometer or less). This calls for common dynamics, for instance the presence of nearby confining shepherding moonlets yet to be discovered around Chariklo, or near some of the Uranian rings.

However, there is an important difference between giant planets and asteroid-like bodies. While the formers exhibit a high degree of axisymmetry, the latters may exhibit a significant, non-axisymmetric structure due to topographic features (mountains, craters, etc...) or large elongation (triaxial ellipsoid).

Here we show that topographic features and/or elongations typical of small bodies induce resonant effects that are much more drastic than around giant planets. For instance, a mountain of height $z$ at the surface of a body of characteristic radius $R$ represents a mass anomaly of $\mu = (z/R)^3$ relative

to the body, i.e. $\mu \sim 10^{-4}$ using $z \sim 5$ km and $R \sim 130$ km typical of Chariklo. The value of $\mu$ becomes even larger considering an triaxial elongated body of semiaxes $A > B > C$. In effect, the mass contained in the two bulges along $A$, compared to the mass contained in the inner sphere of radius $C$, is $\mu = (ABC - C^3)/C^3 \sim 2(\sqrt{AC} - C)/C$. With $A \times B \times C \sim 160 \times 140 \times 100$ km typical of Chariklo (Chapter 3), this yields $\mu \sim 0.2$.

Those values of $\mu$ are crude estimations, but they are orders of magnitude larger than the mass of Mimas (the satellite responsible for the confinement of the inner edge of the Cassini Division) compared to Saturn, $\mu \sim 7 \times 10^{-8}$, and much larger than any mass anomaly that may be present in Saturn, $\mu \sim 10^{-13}-10^{-12}$ (Hedman & Nicholson, 2014). Since the torques associated with the resonances goes like $\mu^2$ (see below), it is expected that they have effects vastly larger than in the context of giant planets.

## 4.1 Two simple cases of non axisymmetric potential

We consider a non-axially symmetric body rotating at a spin rate $\Omega$. We restrict ourselves to two simple cases: (1) a spherical body with a mass anomaly $m_A$ placed at its equator (Fig. 4.1, left panel) and (2) a triaxial ellipsoid with principal axes $A > B > C$ rotating around its shortest axis $C$ (Fig. 4.1, right panel).

Both models create non-axisymmetric terms in the potential acting on a test particle, that revolve at a pattern angular speed $\Omega$. We assume that $m_A \ll M$ and $A-B$, $A-C \ll A$. Consequently, the particle motion is close to Keplerian, while being perturbed by the non-axisymmetric terms from the body. At specific locations, calculated below, tesseral-type resonances appear between the spin of the body and the mean motion of the ring particle.

Note that due to dissipative collisions, a debris cloud initially surrounding a sphere with an equatorial mass anomaly, or a triaxial ellipsoid, rapidly settles into the equatorial plane of the primary. This is because such body creates an azimuthally-averaged potential that conserves the angular momentum $H_C$ of the cloud along the $C$-axis. As collisions also conserve

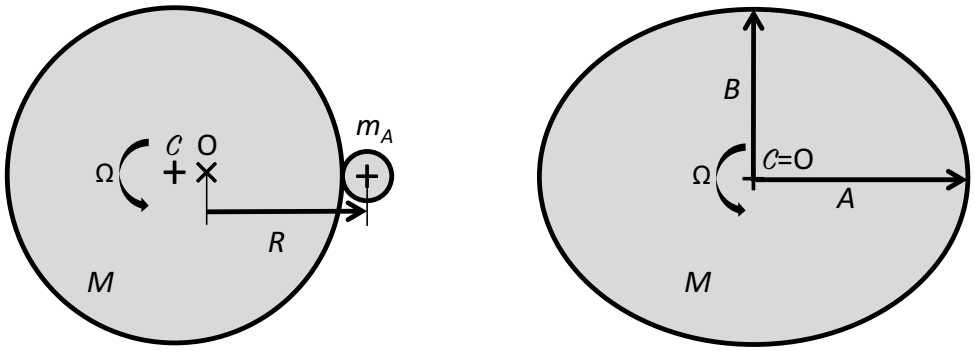


Figure 4.1: Left- A model of a homogeneous spherical body of mass $M$, radius $R$ and center $\mathcal{C}$, attached to a mass anomaly $m_A$ that lies on its equator. The entire system rotates around the center of mass $O$. Right- the same with an triaxial ellipsoid of prinpipal axes $A > B > C$. In both panels, the body is represented pole-on, i.e. it rotates at angular velocity $\Omega$ around an axis perpendicular to the plane of the figure (the equatorial plane of the body) and passing through $O$.

angular momentum, the state of minimum energy for the cloud at constant $H_C$ is a disk resting in the equatorial plane $AB$. Time scales for flattening are very short, typical the collisional time, i.e. a few weeks for a dense ring surrounding Chariklo.

The motion of a particle in the equatorial plane $AB$ has two fundamental frequencies: $\kappa$, the radial epicyclic frequency, and $n$, the mean motion around the primary. Thus $2\pi/\kappa$ and $2\pi/n$ are respectively the period taken by the particle to go from one pericenter to the next pericenter, and the period taken to complete one revolution around the body in inertial space.

Moreover, $a$, $e$, $\lambda$ and $\varpi$ will denote the semi-major axis, orbital eccentricity, mean longitude and longitude of periapsis of the particle, respectively. Finally, the true longitude of the particle will be denoted as $L$. The quantities $\lambda$ and $L$ differ if the orbit is eccentric, $\lambda$ varying linearly with time at rate $n$ (for an unperturbed orbit), while $L$ is modulated during one period, varying more rapidly at pericenter than at apocenter.

This being posed, two kinds of resonances arise. The first kind are the *Lindblad Eccentric Resonances* (LERs) which occur for:

$$\kappa = m(n - \Omega), \tag{4.1}$$

where $m$ is an integer (positive or negative). This equation states that the

natural oscillation frequency of the particle, $\kappa$, matches one of the harmonics of the synodic perturbing frequency felt by the particle, $n - \Omega$. For small perturbations, the particle essentially behaves as a harmonic oscillator, and the LER excites the particle's orbital eccentricity, hence its name.

We define the LER critical resonant angle as:

$$\phi_m = m\lambda_A - (m-1)\lambda - \varpi, \tag{4.2}$$

where $\lambda_A = \Omega t$ describes the orientation of the topographic feature (or the longer axis $A$) in inertial space at time $t$. Since $\kappa = n - \dot{\varpi}$, where the dot denotes time derivatives, $\kappa = m(n - \Omega)$ is equivalent to stating $\phi_m$ *is stationary*. As the motion is usually close to Keplerian, $\kappa \approx n$, Eq. 4.1 reduces to:

$$\frac{\Omega}{n} \sim \frac{m-1}{m}, \tag{4.3}$$

usually referred to as a "$(m-1)/m$ LER".

The second kind of resonance is the *corotation resonance*, which occurs when $\phi = \lambda - \lambda_A$ is stationary, i.e. for

$$n = \Omega, \tag{4.4}$$

meaning that the particle mean motion matches the spin of the primary (corresponding to the so-called geostationary orbit for a satellite around the Earth). Contrarily to the LER, the corotation resonance leaves the particle's orbital eccentricity unchanged, while forcing pendulum-like librations around Lagrange-type points that appear on the corotation orbit, see below. A detailed discussion of Lindblad vs. corotation resonances is provided by El Moutamid et al. (2014).

Using Kepler's third law, the $(m-1)/m$ LER occurs at semimajor axis:

$$a_m \sim \frac{R}{q^{1/3}} \left(\frac{m-1}{m}\right)^{2/3}, \tag{4.5}$$

while the corotation occurs at:

$$a_c \sim \frac{R}{q^{1/3}}. \tag{4.6}$$

Here, $q$ is the dimensionless rotational parameter of the body:

$$q = \frac{\Omega^2 R^3}{GM}, \tag{4.7}$$

where $G$ is the gravitational constant. Since $q$ is the ratio of the centrifugal acceleration at equator of the body to its surface gravity, rotational stability requires $q < 1$.

Eq. 4.5 shows $m > 0$ corresponds to *inner* Lindblad resonances ($\Omega/n = 1/2,\ 2/3,\ 3/4$, etc...), in the sense that they occur inside the corotation radius $a_c$, and $m < 0$ corresponds to *outer* Lindblad resonances ($\Omega/n = 2/1,\ 3/2,\ 4/3$, etc...), i.e. for orbital radii larger than $a_c$. Inner (resp. outer) Lindblad resonances are often noted as ILR (resp. OLR).

We now turn to the calculation of the strengths of the Lindblad and corotation resonance, once the physical parameters of the central body are given.

## 4.2 Lindblad resonances

The position vector $\mathbf{r}$ of a particle relative to the center $\mathcal{C}$ is given in polar coordinates by the true longitude $L$ and radius $r$. Without loss of generality, we assume that at $t = 0$ the mass anomaly $m_A$ or the $A$-axis points towards the origin of longitudes, so that its longitude at any time is $\lambda_A = \Omega t$ (Fig. 4.1). Because of the symmetry of the problem, the potential $U(\mathbf{r})$ acting on the particle can be generically expanded in terms containing cosine functions only:

$$U(\mathbf{r}) = \sum_{l=-\infty}^{+\infty} U_l(r) \cdot \cos\left[l(L - \lambda_A)\right]. \tag{4.8}$$

Restricting ourselves to *first order in eccentricity*, we can expand $r$ and $L$ as $r \approx a - ae\cos(\lambda - \varpi)$ and $L \approx \lambda + 2e\sin(\lambda - \varpi)$. Inserting those expressions in $U_l(r)$ and $\cos\left[l(L - \lambda_A)\right]$, keeping only first order terms in $e$, using the classical linearization formulae $2\sin\alpha\sin\beta = \cos(\alpha - \beta) - \cos(\alpha + \beta)$ and $2\cos\alpha\cos\beta = \cos(\alpha - \beta) + \cos(\alpha + \beta)$, and re-shuffling the terms in the

summation, we obtain $U(\mathbf{r})$ in terms of the orbital elements $a$, $e$, $\lambda$ and $\varpi$:

$$U(\mathbf{r}) = \sum_{m'=-\infty}^{+\infty} U_{m'}(a) \cdot \cos\left[m'(\lambda - \lambda_A)\right] - e \sum_{m=-\infty}^{+\infty} A_m(a) \cdot \cos(\phi_m) + \mathcal{O}(e^2) \tag{4.9}$$

where

$$A_m(a) = \left[2m + a\mathcal{D}\right] U_m(a), \tag{4.10}$$

with $\mathcal{D} = d/da$, and where we recall that $\phi_m = m\lambda_A - (m-1)\lambda - \varpi$ (Eq. 4.2).

The advantage of expressing $U(\mathbf{r})$ as a function of the orbital elements is that the latters are in turns expressible in terms of angle-action variables (e.g. the Delaunay elements or their avatars), allowing the powerful use of Hamiltonian formalism.

As anticipated in the previous section, a LER occurs when a given $\phi_m$ is nearly stationary, and more precisely, librating around a fixed value (usually $0°$ or $180°$). At the corresponding location, the other, rapidly varying terms of the potential can be averaged to zero, except the term with $m' = 0$ in the first summation displayed above. In summary, near a given $(m-1)/m$ LER, we are left with an azimuthally-averaged (axisymmetric) term $U_0(a)$, plus the resonant term containing $\phi_m$, so that the potential felt by the particle reads:

$$U_m^{\mathrm{LER}}(\mathbf{r}) = U_0(a) - eA_m(a) \cdot \cos(\phi_m). \tag{4.11}$$

Although the term $U_0(a)$ does not contribute to the resonant excitation of the particle orbital eccentricity, it does define its radial location $a_m$. In effect, it provides mean motion $n$ and the epicyclic frequency $\kappa$ through

$$n^2(a) = \frac{1}{a}\frac{dU_0(a)}{da} \quad \text{and} \quad \kappa^2(a) = \frac{1}{a^3}\frac{d[(a^2 n)^2]}{da}, \tag{4.12}$$

see Shu (1984). This eventually determines the location of the resonance using Eq. 4.1. As long as only estimations are required, we can take $U_0(a) \sim -GM/a$, so that the motion is Keplerian, and $a_m$ is approximately given by Eq. 4.5. When a more accurate knowledge of the parameters of the central body is known (e.g. its shape), the equations 4.12 above can be used for a better estimation of $a_m$.

Note that equations 4.10 and 4.11 are generic. We now turn to the two specific cases described before to determine the coefficients $A_m$ that appears in Eq. 4.11.

### 4.2.1 Single-mass anomaly

We consider the particle motion in a frame fixed at the center $\mathcal{C}$ of the body $M$, in the case of a single-mass anomaly $m_A$ (left panel of Fig. 4.1). We denote $\mathbf{R}$ the vector connecting the center of mass $O$ to $m_A$ and $\mathbf{\Delta} = \mathbf{r} - \mathbf{R}$ the vector connecting the mass anomaly $m_A$ to the particle at $\mathbf{r}$. The potential acting on the particle is:

$$U(\mathbf{r}) = -\frac{GM}{r} - \frac{Gm_A}{\Delta} + \Omega^2(\mathcal{C}\mathbf{O}\cdot\mathbf{r}) \tag{4.13}$$

The term containing $\mathcal{C}\mathbf{O}$ is the indirect part of the perturbing potential. It can can be written $\Omega^2(m_A/M)\mathbf{r}\cdot\mathbf{R}$, since $\mathcal{C}\mathbf{O} = (m_A/M)\mathbf{R}$. Thus

$$U(\mathbf{r}) = -\frac{GM}{r} - Gm_A\left[\frac{1}{\Delta} - q\frac{\mathbf{R}\cdot\mathbf{r}}{r_s^3}\right]. \tag{4.14}$$

The term $1/\Delta$ can be classically expanded as:

$$\frac{1}{\Delta} = \frac{1}{2R}\sum_{-\infty}^{+\infty} b_{1/2}^{(m)}(r/R)\cos[m(L-\lambda_A)], \tag{4.15}$$

which is actually the mere definition of the Laplace coefficients $b_{1/2}^{(m)}$:

$$b_\gamma^{(m)}(\alpha) = \frac{2}{\pi}\int_0^\pi \frac{\cos(m\theta)}{[1+\alpha^2-2\alpha\cos(\theta)]^\gamma}d\theta. \tag{4.16}$$

Denoting $\alpha = a/R$ and using Eq. 4.11, we obtain near an isolated $(m-1)/m$ LER:

$$U_m^{\mathrm{LER}}(\mathbf{r}) = -\frac{GM}{a} - \frac{Gm_A}{2R}b_{1/2}^{(0)}(\alpha) + e\frac{Gm_A}{2R}\left\{\left[2m + \alpha\frac{d}{d\alpha}\right]b_{1/2}^{(m)}(\alpha) + \delta_{(m,-1)}q\alpha\right\}\cos(\phi_m) \tag{4.17}$$

a classical result, see e.g. Goldreich & Tremaine (1980) or Ellis & Murray (2000). Note that the extra Kronecker delta term $\delta_{(m,-1)}$ stems from the

indirect part of the disturbing potential, and only applies to the case $m = -1$ (outer 2/1 LER).

Eq. 4.14 shows that the effect of a mass anomaly is very similar to that of a satellite, except for two important differences: (1) the indirect term in Eq. 4.14 is multiplied by $q$. This displaces the Lagrange points $L_4$ and $L_4$ away from the triangular configuration (see Fig. 4.2), and (2) the corotation radius now corresponds to $\alpha_c = a_c/R > 1$, meaning that in this case the particle and the satellite do not share anymore the same orbit.

As a consequence, rather than diverging to infinity as $|m|$ tends to infinity, the terms $A^{(m)}(\alpha)$ tend to zero. This can be seen in Eq. 4.16, since the numerator of the term inside the integral oscillates more and more rapidly as $|m|$ increases, while the denominator remains finite since $\alpha_m = a_m/R$ tends to $q^{-1/3} > 1$ (Eq. 4.5).

### 4.2.2 Triaxial ellipsoid

By symmetry, the gravitational potential outside a homogeneous triaxial ellipsoid with principal axes $A > B > C$ is invariant under a rotation of $\pi$ radians around the $C$-axis. As a consequence, only even values of $m$ appear in Eq. 4.8. They have the form $\cos[2p(L - \lambda_A)]$, where $p = m/2$, $p$ integer. The associated critical arguments in Eq. 4.11 now reads:

$$\phi_{2p} = 2p\lambda_A - (2p-1)\lambda - \varpi, \tag{4.18}$$

so that the LERs occur for

$$\frac{\Omega}{n} \sim \frac{2p-1}{2p},$$

i.e. 1/2, 3/4, 5/6, etc... (inner LERs) and 3/2, 5/4, 7/6, etc... (outer LERs). Consequently, this eliminates every other resonance compared to the previous case of a mass anomaly.

The expansion of $U(\mathbf{r})$ in terms containing $\cos(\phi_{2p})$ is detailed in the last section of this chapter. In particular, we now define the reference radius $R$ as $3/R^2 = 1/A^2 + 1/B^2 + 1/C^2$, the elongation $\epsilon$ and oblateness $f$ as:

$$\epsilon = \frac{A-B}{R} \quad \text{and} \quad f = \frac{A'-C}{R}, \tag{4.19}$$

where $A' = \sqrt{(A^2 + B^2)/2}$.

Each term $A_m$ defined in Eq. 4.8 contains a mixture of terms $\epsilon$ and $f$ of various orders. For sake of estimations, it is enough to keep only the lowest orders, which contains only $\epsilon$, see Eq. A.21, where we can substitute $m = 2p$, so that:

$$U_m^{\rm LER}(\mathbf{r}) = U_0(a) + e\frac{GM}{a}\left\{\left[2m - (|m|+1)\right] S_{|m/2|}\epsilon^{|m/2|}\left(\frac{R}{a}\right)^{|m|}\right\}\cdot\cos(\phi_m), \tag{4.20}$$

where $S_{|m/2|}$ is displayed in Fig. A.1, using Eq. A.22.

As shown in the last section, the axisymmetric part of the potential is given by

$$U_0(a) = -\frac{GM}{a}\sum_{l=0}^{+\infty} Q_{2l,0}\left(\frac{R}{a}\right)^{2l} \tag{4.21}$$

where again the terms $Q_{2l,0}$ contain a mixture of $\epsilon$ and $f$ of various orders. To lowest order, only terms in $f$ appear, see Eq. A.16:

$$Q_{2l,0} = \frac{3}{2^l(2l+1)(2l+3)}\frac{(2l)!}{(l!)^2}f^l.$$

This can be injected into Eqs. 4.12 to calculate $\kappa$ and $n$, and then into Eq. 4.1 to finally derive the resonant radius $a_m$.

### 4.2.3 Summary of the section

Eqs. 4.17 and 4.20 provide the expressions of the potential acting on a particle near a $(m-1)/m$ LER. At this stage, it is useful to note that the terms $A_m$ have the dimension of an energy. Thus, it is convenient to write them as:

$$A_m = -\frac{GM}{R}\mathcal{A}_m = -\frac{\Omega^2R^2}{q}\mathcal{A}_m, \tag{4.22}$$

where the *dimensionless* coefficients $\mathcal{A}_m$ are given in Table 4.1, using Eqs. 4.17 and 4.20. This encapsulates the expression of $U_m^{\rm LER}(\mathbf{r})$ in a single expression

$$U_m^{\rm LER}(\mathbf{r}) = U_0(a) + e\frac{\Omega^2R^2}{q}\mathcal{A}_m(a)\cdot\cos(\phi_m), \tag{4.23}$$

and has the advantage to provide an easy comparison between the two cases, using Table 4.1. From the form of the Laplace coefficients (Eq. 4.16) and due to the presence of the term $\epsilon^{|m/2|}$ in Eq. 4.20, it is easy to see that $\mathcal{A}_m$ tends to zero in both cases examined here. This will be confirmed later in the case of Chariklo.

Table 4.1: Strength of Lindblad and corotation resonances

| | |
|---|---|
| Coefficient $\mathcal{A}_m$ of $(m-1)/m$ LER appearing in Eq. 4.23 | |
| Mass anomaly | $\mathcal{A}_m = \left\{ \left[ m + \frac{\alpha}{2} \frac{d}{d\alpha} \right] b_{1/2}^{(m)}(\alpha) + q \frac{\alpha}{2} \delta_{(m,-1)} \right\} \times \mu$ |
| Triaxial ellipsoid ($m$ even) | $\mathcal{A}_m = \left[ 2m - (\lvert m \rvert + 1) \right] S_{\lvert m/2 \rvert} \epsilon^{\lvert m/2 \rvert} \left( \frac{R}{a} \right)^{\lvert m \rvert + 1}$ |
| Azimuthal dependence $f(\phi)$ of corotation potential appearing in Eq. 4.24 | |
| Mass anomaly | $f(\phi) = q^{1/6} \left( \frac{1}{\sqrt{q^{1/3} + q^{-1/3} - 2\cos\phi}} - q^{1/2} \cos\phi \right) \times \mu$ |
| Triaxial ellipsoid | $f(\phi) = 2 \sum_{l=1}^{+\infty} \left( \frac{R}{a_c} \right)^{2l} \left[ \sum_{p=1}^{l} Q_{2l,2p} \cos(2p\phi) \right]$ |

Notes: the dimensionless coefficient $\mathcal{A}_m$ describes the amplitude of the LER term associated with $\cos(\phi_m)$ in Eq. 4.23. Here $\mu = m_A/M$ is the ratio of the mass anomaly to that of the body while $\epsilon = (A-B)/R$ is the elongation of the body (Eq. 4.19). The Laplace coefficient $b_{1/2}^{(m)}(\alpha)$ is given by Eq. 4.16 with $\alpha = a/R$, while $S_{|m/2|}$ is given through Eq. A.22. The dimensionless function $f(\phi)$ describes the azimuthal dependence of the corotation potential, $-(GM/a_c)f(\phi)$, see Eq. 4.24. The coefficient $Q_{2l,2p}$ is given by Eq. A.10.

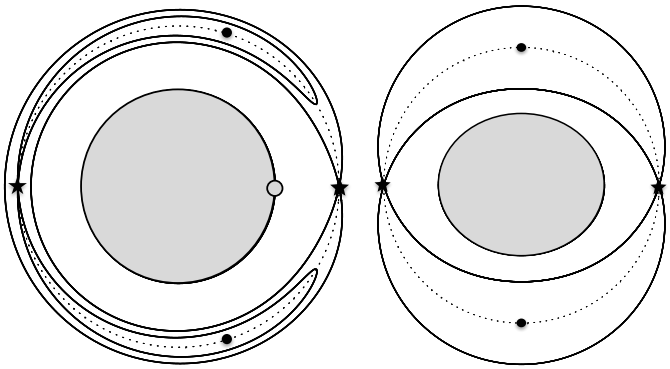

Figure 4.2: Left - The two separatrix trajectories of a particle in case of a mass anomaly, shown in a frame corotation with the central body. They are calculated using Eq. 4.26, using $q = 0.22$, $R = 130$ km, $\mu = (z/R)^{1/3}$ with $z = 5$ km. For a better viewing, the trajectories have been radially expanded by a factor of ten with respect to the corotation radius (dotted circle). Each separatrix goes through a saddle point (star symbol) corresponding to a local maximum of the function $f(\phi)$ (Table 4.1). The inner separatrix encloses the stable elliptical points (dots). Note that they are not located at 60 degrees away from the saddle point at the right, as would be the case for the classical $L_4$ and $L_5$ Lagrange points corresponding to $q = 1$, see text. Right - Same as left panel, but in the case of a traxial ellipsoid with $A = 130$ km and $A - B = 20$ km. Contrarily to the left panel, the separatrix has not been radially stretched here. Note that there is only one separatrix now. Comparing the widths of the corotation zone, we see that a modest elongation $\epsilon = (A - B)/A$ is much more efficient than a topographic feature for creating corotation sites.

## 4.3 Corotation resonance

### 4.3.1 Azimuthal dependence of the corotation potential

Near the corotation radius $a_c$ ($n \sim \Omega$), the potential $U(\mathbf{r})$ (Eq. 4.8) can be written

$$U(\mathbf{r}) \sim U_0(r) - \frac{GM}{a_c} f(\phi), \tag{4.24}$$

where Eq. 4.12 provides the corotation radius, corresponding to $n = \Omega$. Here, $f(\phi)$ is a dimensionless function that describes the azimuthal variation of the potential caused by the corotation resonance, see Table 4.1.

As described in Murray & Dermott (2000), for $f(\phi) \ll 1$, the motion of the particle near corotation stationary points can be split into a fast radial motion frequency $\omega_1$ (along which the eccentricity is conserved), and a slow

pendulum-type motion frequency $\omega_2$, where:

$$\omega_1 \sim \Omega \quad \text{and} \quad \omega_2 \sim \Omega\sqrt{3f"(\phi)}, \tag{4.25}$$

where $f$" denotes the second derivative with respect to $\phi$. The slow motion occurs along trajectories – in the space $(a, \phi)$ – is then (Sicardy & Dubois, 2003):

$$\frac{3}{8}\left(\frac{\Delta a}{a_c}\right)^2 + f(\phi) = \text{constant}, \tag{4.26}$$

where $\Delta a = a - a_c$. It is easy to see that local maxima of $f(\phi)$ correspond to hyperbolic unstable points of the trajectory, while local minima correspond to elliptic-type stable libration centers. If $f$"$(\phi)$ is too large, however, even the elliptic-type points become linearly unstable, see below.

Note that because of the minus sign in Eq. 4.24, the (usually) stable elliptic points correspond to local *maxima* of energy. As such, there are unstable in the presence of dissipative collisions, even if they are dynamically stable for single test particles. This will be discussed later.

For the mass anomaly case, Eq. 4.14 provides the expression of $f(\phi)$ displayed in Table 4.1 (using $a_c \sim R/q^{1/3}$). Note that for $q = 1$, we retrieve the classical Lagrange points $L_3$, $L_4$ and $L_5$ as the local extrema of $f(\phi)$ at $\phi = \pi$, $\phi = \pi/3$ and $\phi = 5\pi/3$, respectively.

In the case of the ellipsoid, the potential in Eq. 4.8 can be re-written

$$U(\mathbf{r}) = U_0(a_c) + 2\sum_{p=1}^{+\infty} U_{2p}(a_c)\cos(2p\phi).$$

The coefficient $U_{2p}(r)$ is given by Eq. A.7, where only the case $p > 0$ is considered. Reshuffling the terms in decreasing orders in $R/a_c$, we obtain:

$$U(\mathbf{r}) = U_0(a_c) + 2\sum_{p=1}^{+\infty} U_{2p}(a_c)\cos(2p\phi) = U_0(a_c) - \frac{2GM}{a_c}\sum_{l=1}^{+\infty}\left(\frac{R}{a_c}\right)^{2l}\left[\sum_{p=1}^{l} Q_{2l,2p}\cos(2p\phi)\right] \tag{4.27}$$

Identification with Eq. 4.24 finally provides the function $f(\phi)$ listed in Table 4.1.

Examples of trajectories in the case of a mass anomaly and ellipsoid potential are given in Fig. 4.2.

### 4.3.2 Stability of the corotation fixed points

As mentioned above, the local minima of $f(\phi)$, usually stable, become linearly unstable if the local curvature of $f$ is too large. When this critical value is reached, the two (real) frequencies $\omega_1$ and $\omega_2$ merge and two new branches appear, where $\omega_1$ and $\omega_2$ have non-zero imaginary parts. This causes a linear instability of the libration center. Let us denote $V(\mathbf{r}) = U(\mathbf{r}) - \Omega^2 r^2/2$ the potential felt by the particle in the frame rotating at angular velocity $\Omega$ ($-\Omega^2 r^2/2$ being the centrifugal potential). this bifurcation occurs, leading to linear instabilities as soon as (Murray & Dermott 2000):

$$\left(4\Omega^2 + V_{xx} + V_{yy}\right)^2 \leq V_{xx}V_{yy} - V_{xy}^2, \tag{4.28}$$

where the indices $x$ and $y$ are short-hand notations for partial derivatives[1].

For the classical $L_4$ and $L_5$ points (mass anomaly case with $q = 1$), this condition leads to the critical Gascheau-Routh value:

$$\mu_{GR} = (1 - \sqrt{23/27})/2 = 0.0385... \tag{4.29}$$

For $q < 1$, the local minima of $f(\phi)$ are less pronounced, i.e. with smaller values of $f$", which requires critical values of $\mu$ larger than $\mu_{GR}$.

In the case of the ellipsoid, the libration centers are at $x = 0$ and $y = \pm a_c$ (Fig. 4.2). It is easy to show that $V_{xx} = -\Omega^2 f"(\phi)$, $V_{yy} = -3\Omega^2$ and $V_{xy} = 0$, where $\phi = \pm\pi/2$. Then Eq. 4.28 reduces to $(1 - f")^2 = 12f"$. The smallest root of this equation, $f" = 7 - \sqrt{48}$, defines the critical value at which the libration centers becomes linearly unstable. Dealing with order of magnitude only, we can simplifiy the expression of $f(\phi)$ by reducing the sum in Table 4.1 to $p = 1$ and $l = 1$ and by using $S_1 = 0.15$, so that:

$$f(\phi) \sim \frac{3}{10} q^{2/3} \epsilon \cos(2\phi) \tag{4.30}$$

and $f"(\pm\pi/2) = -(6/5)q^{2/3}\epsilon$. This yields the critical value of the elongation at which the libration centers becomes linearly unstable:

$$\epsilon_{\text{crit}} \sim \frac{5(7 - \sqrt{48})}{6q^{2/3}} \sim \frac{0.06}{q^{2/3}}, \tag{4.31}$$

the counterpart of Eq. 4.29 for the ellipsoid case.

[1]Note that we use a different sign convention for the potential $V$ compared to Murray & Dermott (2000).

## 4.4 Evolution of a debris disk: Lindblad resonances

A vast amount of literature has been dedicated to the structure of the orbits near Lindblad and corotation resonances, see Henrard & Lemaitre (1983); Sessin & Ferraz-Mello (1984); Ferraz-Mello (1985), the overview by Murray & Dermott (2000), and El Moutamid et al. (2014) for a detailed description of the effect of each kind resonance (and their possible complex coupling).

The dynamics of rings near a LER is a priori even more complex, as it implies a detailed description of collisions between innumerable particles and largely unknown collective effects stemming from self-gravity, pressure and/or viscosity. Fortunately, the problem can be greatly simplified as those effects usually damp the free eccentricity of the particles, limiting their response to the simpler, forced linear regime. Another simplification stems from the fact that the torque exerted at the LER onto the disk is largely independent of the physical processed at work in the ring, as examined now.

### 4.4.1 Torques at Lindblad resonances

We consider a disk of surface density $\Sigma_0$ surrounding the body. If it is dense enough so that collective effects can be sustained (through self-gravity, pressure or viscosity), then each $(m-1)/m$ LER excites spiral waves around the resonant radius $a_m$. This wave then couples with the resonant term $-eA_m(a)\cdot\cos(\phi_m)$ of the potential (Eq. 4.11), resulting in a torque:

$$\Gamma_m = -\text{sign}(n-\Omega)\frac{4\pi^2\Sigma_0}{3\Omega n}A_m^2 = -\frac{4\pi^2 s}{3q^2}\left(\frac{m-1}{m}\right)\Omega^2 R^4 \mathcal{A}_m^2(a_m)\Sigma_0, \quad (4.32)$$

using the short-hand notation[2] $s = \text{sign}(n-\Omega)$. As shown by Meyer-Vernet & Sicardy (1987), the value of $\Gamma_m$ is independent on the detailed physical processes at work in the disk, provided that the disk response remains linear.

Note that in this context, the response of the disk is linear in $\mathcal{A}_m$ (the response in the disk is proportional to the perturbation), while the torque is itself proportional to the response of the disk times the perturbation. Hence, from this general argument, we find that $\Gamma_m \propto \mathcal{A}_m^2$. For instance $\Gamma_m \propto \mu^2$ in the case of a mass anomaly.

[2]With this convention, $s$ is the sign of $m$.

Table 4.2: Torque densities near a Lindblad Eccentric Resonance (LER)

| Physical process | Dimensionless width of LER | Normalized torque density $(a_m/\Gamma_m)d\Gamma/da$ |
|---|---|---|
| Stoke friction | $\alpha_\eta = +\dfrac{2\eta}{3\|m\|\Omega}$ | $\dfrac{\alpha_\eta}{\pi(\alpha_\eta^2 + x^2)}$ |
| Pressure | $\alpha_P^3 = -\dfrac{c^2}{3ma_m^2 n\Omega}$ | $\dfrac{1}{\|\alpha_P\|} A_i\left(\dfrac{sx}{\|\alpha_P\|}\right)$ |
| Viscosity | $\alpha_\nu^3 = +\dfrac{\nu' + 7\nu/3}{3\|m\|a_m^2\Omega}$ | $\dfrac{1}{\alpha_\nu} H_i\left(\dfrac{jx}{\alpha_\nu}\right)$ |
| Self-gravity | $\alpha_G^2 = +\dfrac{2\pi G\Sigma_0}{3ma_m n\Omega}$ | $\dfrac{1}{\sqrt{\pi}\|\alpha_G\|} g\left(\dfrac{-sx}{\sqrt{\pi}\|\alpha_G\|}\right)$ |

Notes: Stoke friction assumes that the particle is submitted to an acceleration $-\eta\mathbf{\Delta v}$, where $\mathbf{\Delta v}$ is the difference between the particle velocity and the local Keplerian velocity field. The quantity $x = (a - a_m)/a_m$ measures the normalized distance to resonance radius $a_m$, $\nu$ and $\nu'$ are the shear and bulk kinematic viscosities, respectively, while $c$ is the typical velocity dispersion in the disk. The functions $A_i$ and $H_i$ are Airy-type functions (with $j = \sqrt{-1}$) and $g$ is a Fresnel-type function, see Abramowitz & Stegun (1968). Adapted from Meyer-Vernet & Sicardy (1987).

Note also that the presence of the sign factor $s$ implies that outer (resp. inner) LERs exert a positive (resp. negative) torque on the disk. This is a generic behavior that does not depends upon the physical process involved. Consequently, the LERs push the disk material away from the corotation zone, i.e. towards the central body inside the corotation radius $a_c$, and outwards outside $a_c$.

This is the core of this chapter: the disk-body interaction depletes the corotation region, with the inner disk region collapsing onto the body and the outer region being pushed outside the outermost LER (2/1 LER in the case of a mass anomaly and 3/2 LER in the case of an ellipsoidal body).

### 4.4.2 Angular momentum deposition

The standard torque 4.32 is actually the *total* value integrated over the resonant zone. The disk behavior can be described more finely through

the normalized torque density function $(a_m/\Gamma_m)d\Gamma/da$, where $d\Gamma/da$ is the torque exerted by unit interval of semi-major axis $a$. In general, we have (Meyer-Vernet & Sicardy, 1987):

$$\frac{a_m}{\Gamma_m}\frac{d\Gamma}{da} = \Re\left[\frac{1}{\pi}\int_0^{+\infty}\exp\left(jkx - j\alpha_G^2\frac{k^2}{2} - j\alpha_P^3\frac{k^3}{3} - \alpha_\nu^3\frac{k^3}{3}\right)\cdot dk\right], \quad (4.33)$$

where $\Re$ is the real part, $j = \sqrt{-1}$, while the coefficients $\alpha_G$, $\alpha_P$ and $\alpha_\nu$ (listed in Table 4.2) describe the effects of self-gravity, pressure and viscosity, respectively. The calculation of $(a_m/\Gamma_m)d\Gamma/da$ can then proceed forward through a classical Fourier transform, using Eq. 4.33.

Explicit solutions can be given in the particular cases where only one coefficient $\alpha$ is present in Eq. 4.33, yielding the behavior of purely self-gravity, acoustic or viscous waves, see Table 4.2 and Fig. 4.3. We have also added the simpler case of a Stokes-like friction, where the particle suffers a drag

$$\gamma_{\rm Stokes} = -\eta\mathbf{\Delta v}, \quad (4.34)$$

where $\mathbf{\Delta v}$ is the offset between the particle velocity and the local Keplerian velocity field. This simple case is used for numerical integrations to illustrate the resonance effects at low computational cost.

Fig. 4.3 indicates how the torque is deposited around the resonant region in various contexts. Note that various processes can be combined, for instance self-gravity and viscosity, as it is the case in the upper right panel of Fig. 4.3. The largest coefficient $\alpha$ imposes the general shape of the solution, but as mentioned above, all the functions shown in Fig. 4.3 possess the same integral, providing the same integrated standard torque $\Gamma_m$ exerted on the disk (Eq. 4.32).

Moreover, the calculation of the coefficients $\alpha$'s in Table 4.2 has also the advantage of providing the typical width $W_{\rm LER}$ associated with the LER:

$$W_{\rm LER} \sim (\text{a few times the largest } \alpha) \times a_m. \quad (4.35)$$

### 4.4.3 Truncation of the disk

A dense debris disk will be truncated at a LER if the resonant torque 4.32 is larger than the viscous torque due to particle interactions (Lynden-Bell

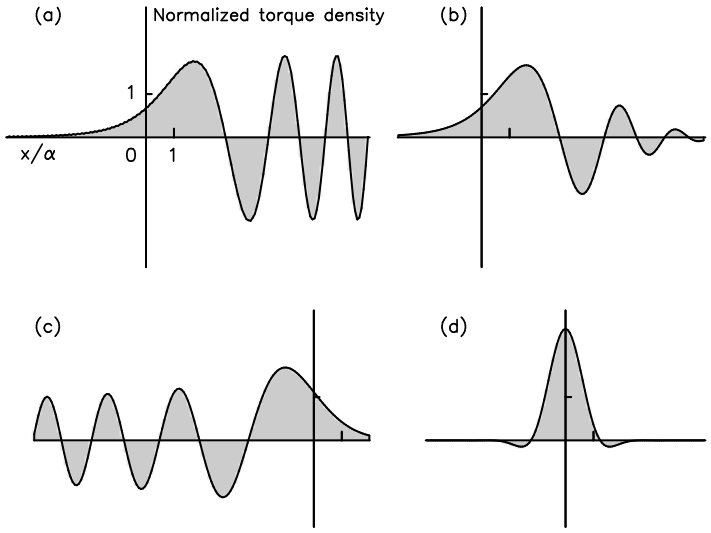


Figure 4.3: Examples of normalized torque density functions $(a_m/\Gamma_m)d\Gamma/da$, calculated from Eq. 4.33. Panel (a): pure inviscid self-gravity wave profile (function $g$ of Table 4.2); panel (b): self-gravity wave mixed with viscosity $\nu$. Note the damping of the wave as $x$ increases; panel (c): inviscid acoustic wave (function $A_i$); panel (d): viscosity-dominated disk response (function $H_i$). All the functions have the same integral $\int_{\infty}^{+\infty} = 1$, ensuring the invariance of the total torque against the physical processes at play in the disk. The main contribution to the integral comes from a region of order unity around the origin $x = 0$ (exact resonance), showing that the resonant torque is exerted over a typical width $W_{\rm LER}$ of a few times $\alpha \times a_m$ around the resonance, where $\alpha$ is the dominant coefficient found in Table 4.2.

& Pringle, 1974):

$$\Gamma_\nu = 3\pi n a^2 \nu \Sigma_0, \tag{4.36}$$

where $\nu$ is the kinematic viscosity. For $|\Gamma_m/\Gamma_\nu| > 1$, the angular momentum luminosity at the edge of the disk is entirely transferred to the central body *via* the LER. It is useful to parametrize $\nu$ through a length parameter $h$:

$$\nu = h^2 n. \tag{4.37}$$

The length $h$ is the typical local thickness of the disk, which is in turn a few times the size of the largest particles (Schmidt et al., 2009).

Combining Eqs. â4.5, 4.32, 4.36 and 4.37, we obtain:

$$\left|\frac{\Gamma_m}{\Gamma_\nu}\right| = \frac{4\pi}{9}\left(\frac{1}{q}\right)^{4/3}\left(\frac{m-1}{m}\right)^{5/3}\left(\frac{R}{h}\right)^2 \mathcal{A}_m^2 \tag{4.38}$$

### 4.4.4 Clearing the corotation zone: time scales

We consider a ring covering a region around a given resonance radius $a_m$. If $|\Gamma_m/\Gamma_\nu| > 1$ the disk is truncated, creating a void between the ring and the corotation radius $a_c$, the ring being pushed away from $a_c$. This generally happens for low values of $|m|$, see Fig. 4.5.

As $|m|$ increases (i.e. as one gets closer to $a_c$), $\Gamma_m$ decreases and the disk may be not truncated anymore. However, the LERs transfer angular momentum to the disk, causing a secular migration that pushes it away from the corotation radius over a typical time scale of $t_{\rm mig} = H/\Gamma_m$, where $H$ is the angular momentum carried by the disk. Denoting $a$ and $W$ the mean radius and radial width of the ring, respectively, we have $H \sim 2\pi W \Sigma_0 \sqrt{GMa^3}$. Using Eqs. 4.3 and 4.7, we obtain

$$H \sim 2\pi\Sigma_0 W \left(\frac{m-1}{m}\right)\left(\frac{\Omega R^3}{q}\right), \tag{4.39}$$

and from Eq. 4.32:

$$t_{\rm mig} \sim \frac{H}{\Gamma_m} = \frac{3q}{4\pi^2}\left(\frac{W}{R}\right)\left(\frac{T_{\rm rot}}{\mathcal{A}_m^2}\right), \tag{4.40}$$

where $T_{\rm rot} = 2\pi/\Omega$ is the rotation period of the body. If the ring is covering several resonances, then all the corresponding torques must be added, so that:

$$t_{\rm mig} \sim \frac{H}{\sum \Gamma_m} = \frac{3q}{4\pi^2}\left(\frac{W}{R}\right)\left(\frac{T_{\rm rot}}{\sum \mathcal{A}_m^2}\right), \tag{4.41}$$

where the summation concerns the resonances covered by the disk.

In order to illustrate the migration of a particle under the effect of the LERs, we have considered the case of mass anomalies of $\mu = 4 \times 10^{-4}$ and $\mu = 8 \times 10^{-4}$. This is about 10 times larger than the $\mu$'s expected from Chariklo's topographic features (see below), but has the advantage of increasing the migration rate, and thus require less computation time. Moreover, we have chosen a Stokes friction $-0.01 \times \mathbf{\Delta v}$, as defined in Eq. 4.34. Again, the friction coefficient is about 10 times larger than the real case of Chariklo, but has the advantage of showing better the resonance locations.

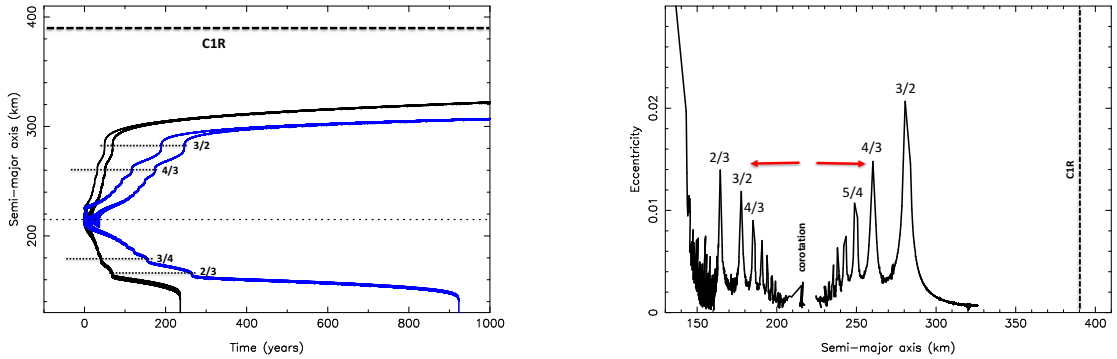


Figure 4.4: Left panel - Evolution of the semi-major axes of particles starting at the corotation radius (dotted line), and submitted to a Stokes friction $-0.01 \times \mathbf{\Delta v}$ ( Eq. 4.34). The particles first escape the corotation zone and then migrate away, towards the body (whose surface is at 130 km) inside the corotation, and outwards outside the corotation. Note the "kicks" applies at each resonance crossing, due to the resonant torque. The location of ring C1R is marked by the dashed line. Mass anomalies of $\mu = 4 \times 10^{-4}$ (blue curves) and $\mu = 8 \times 10^{-4}$ (black curves) create LERs at locations labelled 3/2, 4/3, etc... Right panel - Example of migrations (indicated by the red arraows) for two of the particles shown on left panel, for the case $\mu = 8 \times 10^{-4}$. At each resonance crossing, the eccentricity of the particle is excited, and then damped again due Stokes friction. Note that the particles did not have the time to reach the outer 2/1 LER near 340 km in those particular integrations.

## 4.5 Applications to Chariklo's ring system

We now apply our results to Chariklo's ring system. Although some factors entering in Eqs. 4.40 and 4.38, can securely be estimated, others remain largely unknown. However, some general behavior can still be deduced from the results obtained in the previous sections.

We adopt here a volumetric, reference radius $R \sim 130$ km for Chariklo. Furthermore, the rotational parameter $q$ (Eq. 4.7) can be re-expressed as $q \sim 3\pi/(G\rho T_{\rm rot}^2)$, where $\rho$ is the bulk density of the body, assuming a homogeneous sphere of typical radius $R$. Using $T_{\rm rot} = 7.004 \pm 0.036$ h (Fornasier et al., 2014), we get $q \sim 0.22/\rho_{\rm g\ cm^{-3}}$. The density should be close to 1 g cm$^{-3}$ for an expected icy Chariklo. Thus, taking $q \sim 0.22$ should be correct to within a factor of 2.

The angular momentum contained in Chariklo's spin is $H_C \sim MR^2\Omega$.

Using Eq. 4.39, the ratio of the ring angular momentum to that of the central body is $H/H_C \sim 2\pi\Sigma_0 WR/qM$. By analogy with Saturn's rings, we may take a typical value of $\Sigma_0 = 500$ kg m$^{-3}$ (Colwell et al., 2009). Moreover, taking $W \sim 100$ km for the width of an initial debris disk and $M \sim 10^{19}$ kg, we obtain $H/H_C < 10^{-4}$. This shows that any exchange of angular momentum between the disk and the body will induce minimal changes on Chariklo's spin rate $\Omega$.

### 4.5.1 Lindblad resonances

The width $W_{\rm LER}$ of the region where most of the angular momentum is deposited at a LER can be estimated using Eq. 4.35 and the values listed in Table 4.2. For instance, if Chariklo's debris disk is dominated by self-gravity, then $W_{\rm LER,G} \sim |\alpha_G| \times a_m$. This can be re-written:

$$W_{\rm LER,G} \sim 2 \times 10^{-4} \left(\frac{T_{\rm rot}}{\rm h}\right) \sqrt{\left(\frac{|m-1|}{m^2}\right) \left(\frac{\Sigma_0}{\rm kg\ m^{-2}}\right) \left(\frac{a_m}{\rm km}\right)}\ {\rm km} \qquad (4.42)$$

Using $\Sigma_0 \sim 500$ kg m$^{-2}$, $a_m \sim 250$ km and $T_{\rm rot} \sim 7$ h provide:

$$W_{\rm LER,G} \sim 0.5 \sqrt{\frac{|m-1|}{m^2}}\ \ {\rm km} \qquad (4.43)$$

Conversely, for a disk where collisions (i.e. the viscosity $\nu$) are the dominant process, we have $W_{\rm LER,G} \sim |\alpha_\nu| \times a_m$. Writing $\nu \sim h^2 n$ (Eq. 4.37), we obtain:

$$W_{\rm LER,\nu} \sim \left[\frac{7}{9(m-1)}\right]^{1/3} \left(\frac{h}{a_m}\right)^{2/3} \times a_m \sim \frac{0.06}{(m-1)^{1/3}} \left(\frac{h}{\rm m}\right)^{2/3}\ \ {\rm km}, \quad (4.44)$$

i.e. $W_{\rm LER,\nu} \sim 0.2/(m-1)^{1/3}$ km for a typical value of $h \sim 5$ m.

Comparison of Eqs. 4.43 and 4.44 shows that self-gravity should dominate viscosity, but not my much, in terms of disk behavior near a LER. In any case, the typical values of $W_{\rm LER}$ should be of the order of a fraction of kilometer, whatever the main physical process is acting in the disk.

From Eq. 4.5, we see that the spacing between two adjacent LERs for large $m$'s is $|a_{m+1} - a_m| \sim 2a_c/3m^2$. By comparison with Eq. 4.43, we see

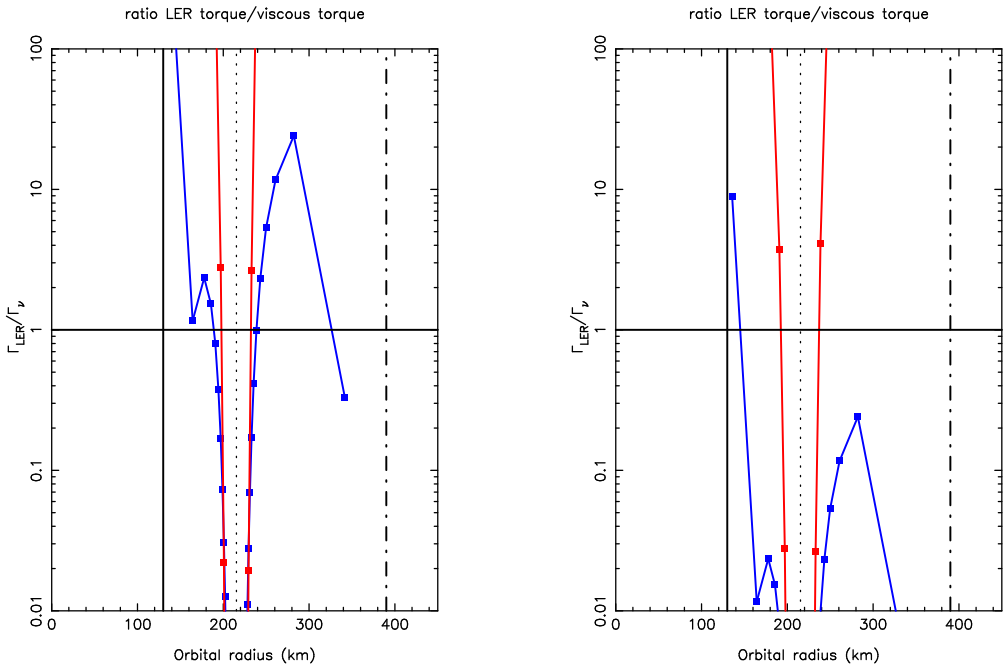


Figure 4.5: The ratio $|\Gamma_m/\Gamma_\nu|$ (Eq. 4.38) at various $(m-1)/m$ Lindblad resonances. The used parameters are: $T_{\rm rot} = 7$ h, $R = 130$ km, $q = 0.22$, $z = 5$ km, $A - B = 20$ km. Red: triaxial ellipsoid, blue: mass anomaly. In each panel, the vertical solid, dotted and dot-dashed lines are respectively: Chariklo's radius, the corotation radius and the location of the main ring C1R. The horizontal solid line marks the level $|\Gamma_m/\Gamma_\nu| = 1$ above which the disk is truncated. Left panel - Low viscosity case, using $h = 2$ m. Righ panel - High viscosity case, using $h = 20$ m. See text for details.

that $W_{\rm LER}$ becomes larger than the spacing $|a_{m+1} - a_m|$ for large values of $m \sim 40$, i.e. close to the corotation radius. In other words, the strongest LERs corresponding to low values of $m$ (Fig. 4.5) are isolated, each depositing locally angular momentum at the rate given by Eq. 4.32.

We calculate the coefficients $\mathcal{A}_m$ from Table 4.1 by using $\mu \sim (z/R)^3$ in the case of the mass anomaly (recalling that $z$ is the height of the topographic feature) and $\epsilon = (A - B)/R$ (Eq. 4.19) in the case of an ellipsoidal body. From Chapter 3, we get typical values $z \sim 5$ km, i.e. an order of magnitude estimation $\mu \sim 5 \times 10^{-5}$. Similarly, taking $A - B \sim 20$ km and $R \sim 130$ km, we obtain $\epsilon \sim 0.15$.

The quantity $h$ is the least constrained quantity of all, as it is a microscopic parameter. More precisely, it is the length factor entering in the definition of the kinematic viscosity $\nu$ (Eq. 4.37), and is eventually a mea-

sure of the size of the largest ring particles. Colwell et al. (2009) give typical values of $\nu = 10^{-3} - 10^{-1}$ m$^2$ s$^{-1}$ for Saturn's A ring. From $n = 2.5 \times 10^{-4}$ s$^{-1}$ in the case of Chariklo, we obtain a typical range $h = 2 - 20$ m.

The resulting viscosity eventually sets the minimum torque value above which disk truncation occurs (Eq. 4.38). The resulting torque ratios are plotted in Fig. 4.5. In both the low $h = 2$ m and high $h = 20$ m viscosity cases, the effect the elongation is overwhelming: the disk is truncated for all LERs that are farther than $\sim 10$ km from the corotation. The effect of a mass anomaly is less drastic. For instance, in the low viscosity case ($h = 2$ m), an equatorial topographic feature of height $z = 5$ km can truncate the disk at the outer 2/1, 3/2, ... 7/6 LERs, and the inner 1/2, 2/3, 3/4 LERs, but not weaker LERs that are closer to the corotation radius. In the high viscosity case ($h = 20$ m), none of the corresponding LERs can truncate the disk, except for the innermost 1/2 LER.

Independently of the truncation issue, the migration time scales associated with the torque deposition (Eq. 4.41) are very short. For instance, if we place a 100-km wide disk outside the corotation radius (i.e. typically between 230 and 330 km, see Fig. 4.5), it will be pushed away beyond the outermost LER in a fraction of year if the body has $A - B = 20$ km, and some tens of thousands years due to $z = 5$ km topographic features. Time scales are even smaller for a disk that is initially placed between Chariklo's surface and the corotation radius.

Note that the the outermost resonance is the 2/1 outer LER near 340 km in the case of a mass anomaly, and the 3/2 outer LER near 280 km in the case of the ellipsoid body (due the the symmetry of the problem, the 2/1 LER vanishes, see the discussion laed earlier).

Thus, we are left with a region around the corotation, where the LERs are too weak for pushing the material away from that region. However, as seen now, the corotation sites representing maxima of energy, dissipative collisions will also deplete that zone.

### 4.5.2 Corotation resonances

The level curves of $(3/8)(\Delta a/a_c)^2 + f(\phi)$ (Eq. 4.26 and Table 4.1) define the trajectories of the particles in the $(a, \phi)$ space, see examples in Fig. 4.2.

Using Eq. 4.30, we obtain the full width of the corotation site (i.e. the maximum radial excursion of a particle trapped in that region) in the case of an ellipsoidal body:

$$W_{\rm cor} \sim 4R\sqrt{\frac{2\epsilon}{5}} \tag{4.45}$$

For $R \sim 130$ km and $A-B \sim 20$ km, the body has an elongation parameter $\epsilon \sim 0.15$ (see definition in Eq. A.11). Thus, $W_{\rm cor} \sim 120$ km, i.e. $\pm 60$ km on each side of $a_c$ (Fig. 4.2). Note in passing that from Eq. 4.31, the critical value of $\epsilon$ for which the corotation points are unstable is $\epsilon_{\rm crit} \sim 0.16$ for $q = 0.22$. Thus, the value of $\epsilon$ is close to that that would cause the linear instability of the corotation points.

From Eqs. 4.24 and 4.30, we see that the difference of potential energy per unit mass between the maximum (stable point) and minimum (unstable saddle point) levels is:

$$\Delta E = \frac{3}{5}\epsilon q^{2/3}\frac{GM}{a_c} \tag{4.46}$$

The typical energy loss (per unit mass) that a particle suffers during a collision is $\sim v_{\rm rms}^2$, where $v_{\rm rms}^2$ is the velocity dispersion in the ring, which is in turn related to the viscosity length parameter $h$ through $v_{\rm rms}^2 \sim hn$. Thus, the collisional dissipation rate per unit mass for a given particle is $dE/dt \sim h^2n^2/t_c$, where $t_c$ is the average time between collisions. The time is takes to bring a particle from a stable corotation point to an unstable saddle point, i.e. the time scale to clear the corotation zone, is $t_{\rm clear} = \Delta E/(dE/dt)$. Expressing $a_c$ as a function of $R$, we finally obtain:

$$t_{\rm clear} = \frac{3}{5}\left(\frac{R}{h}\right)^2 \epsilon \times t_c \tag{4.47}$$

Using again $R = 130$ km, $\epsilon = 0.15$. and $h = 2 - 20$ m, and noting that the collision time $t_c$ is typically an orbital period (7 h) for a dense disk, we have $t_{\rm clear} = 3 \times 10^3 - 3 \times 10^5$ years. Although large uncertainties are present in the estimation of $t_{\rm clear}$, the corotation clearing time is very small compared to the age of the solar system, or even compared to Chariklo's residence time on its present orbit, some 10 Myr (Horner et al., 2004).

Note finally that a mass anomaly of the order of $\mu = 5 \times 10^{-5}$ would create a corotation potential that is much shallowed than that caused by

an elongated body. Consequently, the value of $\Delta E$ is much smaller and the corotation clearing time much shorter.

## 4.6 Discussion

In this chapter, we have shown that:

• Mass anomalies or an ellipsoidal shape give rise to torques at $(m-1)/m$ Lindblad resonances. They push the material of a debris disk inside the corotation radius towards the central body, and the material outside that radius to the outer part of the system.

• Topographic features typical of those of Chariklo (a few kilometers in height) and/or elongations of the order of 0.15 result in very short migration times scales.

• The corotation region, where the Lindblad resonances are weak, is itself unstable due to dissipative collisions. Again, the clearing time scales of that zone are short.

Fig. 4.4 shows that the rings C1R and C2R are outside the outermost 2/1 LER (near 340 km), as expected from the results above. The question that arises now is to know why the rings are currently situated near 400 km, and not closer to the 2/1 LER. Part of the answer could be that as the disk material migrates outwards, it get closer to Chariklo's Roche limit, and then keen to accrete into moonlets. Those moonlets could act in turn as shepherds for the remaining disk, and the present situation could be the final stage of a mixture of moonets and rings that have reached an equilibrium.

This poses another question: for the mechanism proposed here to work, Chariklo's Roche limit must be outside the outermost 2/1 LER, otherwise the disk material would accrete into moonlets and no ring could survive. From, Eq. 4.5), the 2/1 LER is at

$$a_{2/1} = 2^{2/3} a_c = 2^{2/3} \left( \frac{GM}{\Omega^2} \right)^{1/3}$$

On the other hand, ring particles tend to accrete inside an orbital radius

$$a_{\rm Roche} \sim \left( \frac{4\pi}{\gamma} \right)^{1/3} \left( \frac{\rho}{\rho'} \right)^{1/3} R$$

(Tiscareno et al., 2013), where $\rho'$ is the density of the particles and $\gamma$ is a dimensionless factor that describes the particles. For instance, $\gamma = 0.85$ for a fluid particle (providing the classical expression for the Roche limit), or $\gamma = 1.6$ for a more realistic particle that fills its lemon-shapedRoche lobe (Porco et al., 2007).

The condition stated above is then $a_{2/1} < a_{\rm Roche}$, which eventually reduces to

$$\rho' < \frac{3}{4\gamma}\frac{\Omega^2}{G}. \tag{4.48}$$

Using a rotation period of 7 h, this provides $\rho' < (700/\gamma) = 440$ kg m$^{-3}$, adopting the value $\gamma = 1.6$ that seems more appropriate for planetary rings (Tiscareno et al., 2013). The 440 kg m$^{-3}$ value is in fact typical of the small Saturnian moons that are close to or inside the rings (Thomas, 2010). No direct measurement of the density of individual ring particles has been made so far. However, they are thought to consist in under-dense $\rho < 1000$ kg m$^{-3}$ material made of rubble-pile aggregates (Charnoz et al., 2009), which makes the 440 kg m$^{-3}$ value mentioned above plausible.

It is interesting to note that, in the frame of our model, low density particles are required for a ring to form around a small body. This favors icy rings over rocky particles. Also, it is interesting to note that if the central body rotates too slowly, then at some point the condition above requires unrealistically underdense particles. In essence, for a slow rotator, the LERs are too far away from the body, and the disk that is pushed to those regions accretes into satellites instead of remaining a ring.

# Chapter 5

# Conclusions

As already mentioned in the Introduction, stellar occultations by TNOs and Centaurs is a powerful technique that allows to study the shape and size of small distant Solar System objects. So far, over a dozen TNOs and Centaurs has been observed with this technique, providing sizes and shapes with typical accuracies ranging from a few to about ten kilometers, depending on the body. This is much better than any other technique, beating thermal-derived measurements by at least one order of magnitude.

In that context, I participated to the discovery of a ring system around the Centaur object (10199) Chariklo during an occultation in 2013 (a work made at the beginning of my PhD). This is the first ring system around a small Solar System object and the fifth after the rings of the giant planets. However, the basic physical characteristics of Chariklo and its rings remain fragmentary. With an angular size of about 80 mas (rings included), Chariklo is unresolved from ground-based and space-based images, so that the observation of stellar occultations remains the only tool to study this system in detail.

In this thesis I addressed three important points for improving the whole chain that goes from stellar occultation observations to scientific results: the use of specific fast cameras, the data analysis that constrains the sizes and shapes of the objects and, in the case of Chariklo, the physical implications of shape onto the ring dynamics.

*Characterization of cameras and time acquisition.* In the first part I analyzed the sensitivity and timing accuracy of two alternative occultation kits, consisting in a fast portable camera, a time registration system, and the ac-

quisition software. The use of portable kits is of paramount importance as they allow us to increase the chances of detection of a stellar occultation and to cover properly the occultation path of an object. More precisely, I performed tests on two alternative cameras, the Kite EMCCD camera from Raptor Photonics and the ZWO ASI178MM CMOS. The goal was to determine the relative efficiency under typical conditions found in the observation of stellar occultations. From those tests I determined that the Kite performance is better than the CMOS camera, in term of SNR, reaching stars one magnitude fainter under the same conditions. This allow us to reach roughly 2-3 times more stars, which in consequence increase in the same factor the number of potential targets to observe stellar occultations.

I confirmed that the current time-acquisition system, based on the TimeBox device, has an absolute accuracy better than 20 ms with respect to the reference time, UTC. This translates into an accuracy in the order of 400 m in the sky plane, which is more than appropriate for the current status of stellar occultations by TNOs and Centaurs.

The direct consequence of these tests was our purchase of two Kite-based kits and five CMOS-based kits in the frame of the Lucky Star project. This is a compromise between price, performance and quantity of available kits. Together with the already existing Merlin kits (based in a previous EMCCD camera model) this provides a good balance between state of the art cameras, and less performing ones. Note that it is important to dispatch as many as possible stations in the shadow paths, SNR allowing.

It is important to mention that those tests required many important changes in the acquisition software proposed by the manufacturer of those cameras and the TimeBox.

My tests also define a rigorous protocol concerning the accuracy of time registration and validation of the camera sensitivity. Eventually this may be used as a guide line for other teams to specify the range of conditions under which the best performances are obtained. This is particularly important for the amateur community which actively participates to the observations, in a context where misleading numbers given by manufacturers sometimes overestimates the performances of a given equipment.

The first observations with these new kits were performed during the

successful recent observation of the occultation by Chariklo of 2017 June 22 in Namibia, whose results are not incorporated in this work.

*Physical characterization by stellar occultations.* In the second part of the thesis I addressed the problem of how to extract physical properties of an body from occultation data. Three object were considered, each with increasing degree of complexity. The first case involved a well sampled multi-chord occultation by the scattered disc object 2007 $UK_{126}$, the second a two multi-chord occultations by the plutino 2003 $AZ_{84}$ separated by a couple of years, and the third involves five single and double chord occultations by the Centaur object Chariklo observed between 2013 and 2016.

For 2007 $UK_{126}$, the size and shape was derived by adjusting an elliptical limb model to the occultation chord extremities. In this project, my work consisted in deriving the density under the assumption of hydrostatic equilibrium of an homogeneous body (a Maclaurin spheroid). For the nominal rotation period of 11 hours, the object density lies in the range [320, 1740] kg $m^{-3}$, while for $T = 8$ hr (the lowest plausible rotation period) the density lies in the range [600, 3300] kg $m^{-3}$. Additionally, I found that the most probable values for the density are close to the upper limit of the respective density range. These results were presented in Benedetti-Rossi et al. (2016).

For 2003 $AZ_{84}$, elliptical limbs were fitted to each stellar occultation, resulting in two ellipses with substantially different size and orientation in the sky. We interpret this as being due to a body with the shape of a Jacobi ellipsoid that has been observed in 2012 and 2014 at two different rotation angles. Using the elliptical fits as a starting point, my contribution was to adopt simplifications to derive a range of compatible orientation and shape for the object, parametrized by the uniform density of a triaxial body in hydrostatic equilibrium (the Jacobi solution). Under these assumptions, the density was constrained to a narrow region around $\sim$870 kg $m^{-3}$ and opening angle $B \sim 48°$. These results were presented in (Dias-Oliveira et al., 2017).

This said, the main part of this chapter concentrates on the analysis of five stellar occultations by the Centaur object Chariklo, observed between 2013 and 2016. In this analysis I adopted a Bayesian-MCMC method to

determine size, shape, density and orientation of Chariklo's main body. The occultation data indicate that Chariklo's main body is triaxial with dimensions $a = 148^{+6}_{-4}$ km, $b = 132^{+6}_{-5}$ km and $c = 102^{+10}_{-8}$ km. Restricting ourselves to a homogeneous body in hydrostatic equilibrium (Jacobi solution) the dimensions are $a = 157 \pm 4$ km, $b = 139 \pm 4$ km and $c = 86 \pm 1$ km. The Jacobi solution yields a geometric albedo for the ring particles of $p_p$ less than 2%. This is darker than Uranus ring particles, and seems implausibly low, suggesting that Chariklo is not a Jacobi ellipsoid, and favoring the generic triaxial ellipsoid from which I obtain a more reasonable value of $p_p \sim 10\%$.

Another implication of my work is the presence of topographic features ranging from 6 to 11 km, depending on the models. This is comparable to the topographic features found on the Saturnian satellites Hyperion and Phoebe, that have the same range of size and density as Chariklo.

*The dynamics of rings around a non-spherical body.* In the third part of the thesis, I considered the effect of resonances between the mean motion of the ring particles and the rotation of a non-spherical central body. Elaborating from my results on Chariklo's shape, I studied two simple cases, a spherical body with a mass anomaly placed at its equator and a homogeneous triaxial ellipsoid. In both cases, the mass excess with respect to a spherical reference body is much larger than for the giant planets. As a consequence, the interactions between the main body and a collisional disk of material in its equatorial plane rapidly depletes the corotation region, where the orbital period of the particles equals the rotation period of the main body. From our estimation of Chariklo's mass and rotation period, this is located at a radius of $\sim 220$ km. In both scenarios, the torque exerted by the mass excess at the location of the Lindblad resonances, pushes the material inside the corotation radius towards the central body, and the material outside that radius towards the outer part of the system. More precisely, it pushes the material outside the outermost Lindblad resonance. In the case of the mass anomaly hypothesis, this corresponds to the 2/1 Lindblad resonance near 340 km, while in the case of the ellipsoid this corresponds to the 3/2 resonance near 280 km.

The scale of the topographic features and/or elongations derived for Chariklo, result in very short migration times scales of the material in the

corotation region, at most some tens of thousands years. This resonant mechanism explains why the inner region of Chariklo's surroundings is devoid of rings and why they are relatively far away (∼400 km) from the central body.

At that point, I consider another problem, which is the accretion of the pushed material into moonlets instead of remaining as a ring. This requires a reasonable density for the ring particle of typically $\sim 400$ kg m$^{-3}$ such that they remain inside the Chariklo's Roche limit. In that context, rings and moonlets possibly coexist, with the latters acting as shepherding moonlets for confining the rings.

**Perspectives**

My work was developed during an important turning point concerning stellar occultations, that is, the first results obtained using the astrometric catalog from the ESA Gaia mission. In practice, predictions can now be improved by a factor at least ten with respect to the previous period. For instance, with the first data release (DR1) of Gaia in late 2016, occultation predictions by Chariklo improved down to a level of 10 mas (about 100 km projected at the distance of the body). A further step forward will be reached with the DR2 catalog, to be released in April 2018. It will include the star proper motions and provide star positions at the sub-mas accuracy level. For instance, a special early release of a star position from DR2 concerning the star occulted by Chariklo on 2017 June 22 has been kindly provided by the Gaia project. This provided a prediction that was eventually good at the 3 mas level (30 km at Chariklo) and lead to five successful ring detections and four successful main body detections. The 3 mas discrepancy stems from the uncertainty of Chariklo's ephemerides, that will be improved to better predict the next events.

This has important consequences for the future, as my Bayesian-MCMC method and tools can readily be applied to these new data sets. This can be done without further conceptual modifications or adoption of further simplifications. In this context, my method can also be extended to the analysis of occultations by other TNOs which are targets of interest for the ERC project Lucky Star, or others.

Turning back to Chariklo, the new data sets will bring independent constraints on the position of Chariklo's center relative to the ring center. In that way, it may serve to detect ring eccentricities and constrain further their dynamics.

In this thesis I adopted a Bayesian approach for the inference of the model parameters, but comparing various models in the Bayesian framework was left outside of the scope of this work. This is a natural extension of this work that can be applied to give preference to two or more body models that fit the occultation data equally well.

Additionally, the predictions of the projected limb shape of two competing models can help optimizing the deployment of mobile stations during future stellar occultations. In particular, detection of topographic features along the limb of those bodies will be made possible thanks to the accuracy of the Gaia catalog releases. For instance, expected topographic features of 10 km at Chariklo's surface represent an angle of 1 mas in the sky plane. The deployment of several stations in a band of a about 50 km in width will thus permit to detect these features. Not only we will have a global view of the shape and size of the body, but also a more "geological" approach of this object and others.

The results presented in Chapter 4 are generic and can be applied to other ring systems found around other TNOs. In particular, a recent occultation by the dwarf planet Haumea[1] indicates the presence of a ring system around the body. The calculations presented in Chapter 4 appear to be consistent with the orbital radius of that ring, considering the shape of Haumea derived from this occultation and the known rotation period of that body.

**Acknowledgements**

Rodrigo LEIVA acknowledges support from CONICYT-PCHA/Doctorado Nacional/2014-21141198

Part of the research leading to these results has received funding from the European Research Council under the European Community's H2020 (2014-2020/ ERC Grant Agreement n 669416 "LUCKY STAR").

[1]These results are not published yet and cannot be discussed elsewhere to avoid breaking the embargo policy.

Based on observations obtained at the Southern Astrophysical Research (SOAR) telescope, which is a joint project of the Ministério da Ciência, Tecnologia, e Inovação (MCTI) da República Federativa do Brasil, the U.S. National Optical Astronomy Observatory (NOAO), the University of North Carolina at Chapel Hill (UNC), and Michigan State University (MSU).

Based on observations obtained with the SARA Observatory 0.6 m telescope at Cerro Tololo, which is owned and operated by the Southeastern Association for Research in Astronomy (saraobservatory.org).

# Bibliography

Abramowitz, M., & Stegun, I. 1968, Handbook of mathematical functions with formulas, graphs and mathematical tables (New York: Dover Publications)

Allen, R. L., Gladman, B., Kavelaars, J. J., et al. 2006, The Astrophysical Journal, 640, L83

Altenhoff, W. J., Menten, K. M., & Bertoldi, F. 2001, Astronomy and Astrophysics, 366, L9

Alvarez-Candal, A., Ortiz, J. L., Morales, N., et al. 2014, Astronomy & Astrophysics, 571, A48

Araujo, R. A. N., Sfair, R., & Winter, O. C. 2016, The Astrophysical Journal, 824, 80

Assafin, M., Camargo, J. I. B., Vieira Martins, R., et al. 2010, Astronomy and Astrophysics, 515, A32

—. 2012, Astronomy & Astrophysics, 541, A142

Balmino, G. 1994, Celestial Mechanics & Dynamical Astronomy, 60, 331

Bauer, J. M., Grav, T., Blauvelt, E., et al. 2013, The Astrophysical Journal, 773, 22

Belskaya, I., Bagnulo, S., Barucci, M., et al. 2010, Icarus, 210, 472

Benedetti-Rossi, G., Sicardy, B., Buie, M. W., et al. 2016, The Astronomical Journal, 152, 156

Bérard, D., Sicardy, B., Camargo, J. I. B., et al. 2017, Astrophysical Journal (submitted), arXiv:1706.00207

Biver, N., Bockelée-Morvan, D., Colom, P., et al. 2002, Earth, Moon, and Planets, 90, 5

Bockelee-Morvan, D., Lellouch, E., Biver, N., et al. 2001, Astronomy and Astrophysics, 377, 343

Boyce, W. 1997, Celestial Mechanics and Dynamical Astronomy, 67, 107

Braga-Ribas, F., Sicardy, B., & Ortiz, J. 2011, Dps2011, 6, 1

Braga-Ribas, F., Vieira-Martins, R., Assafin, M., et al. 2014a, Revista Mexicana de Astronomia y Astrofisica: Serie de Conferencias, 44, 3

Braga-Ribas, F., Sicardy, B., Ortiz, J. L. J., et al. 2013, The Astrophysical Journal, 773, 26

Braga-Ribas, F., Sicardy, B., Ortiz, J. L., et al. 2014b, Nature, 508, 72

Brosch, N. 1995, Monthly Notices of the Royal Astronomical Society, 276, 571

Brown, M. E. 2000, The Astronomical Journal, 119, 977

—. 2013, The Astrophysical Journal, 767, L7

Brown, M. E., & Koresko, C. D. 1998, The Astrophysical Journal, 505, L65

Brown, M. E., Trujillo, C., & Rabinowitz, D. 2004, The Astrophysical Journal, 617, 645

Bus, S. J., A'hearn, M. F., SCHLEICHER, D. G., & Bowell, E. 1991, Science, 251, 774

Camargo, J. I. B., Vieira-Martins, R., Assafin, M., et al. 2014, Astronomy & Astrophysics, 561, A37

Chandrasekhar, S. 1987, Ellipsoidal figures of equilibrium (New York: Dover Publications), 264

Charnoz, S., Dones, L., Esposito, L., Estrada, P., & Hedman, M. 2009, Origin and Evolution of Saturn's Ring System, ed. M. Dougherty, L. Esposito, & S. Krimigis, 537

Chen, Y.-T., Kavelaars, J. J., Gwyn, S., et al. 2013, The Astrophysical Journal, 775, L8

Choi, Y. 2002, Icarus, 160, 300

Colwell, J., Nicholson, P., Tiscareno, M., et al. 2009, The Structure of Saturn's Rings, ed. M. Dougherty, L. Esposito, & S. Krimigis (Dordrecht: Springer), 375

Delsemme, A. 1982, in IAU Colloq. 61

Desmars, J., Camargo, J. I. B., Braga-Ribas, F., et al. 2015, Astronomy & Astrophysics, 584, A96

Dias-Oliveira, A., Sicardy, B., Lellouch, E., et al. 2015, The Astrophysical Journal, 811, 53

Dias-Oliveira, A., Sicardy, B., Ortiz, J. L., et al. 2017, The Astronomical Journal, 154, 22

Dotto, E., Barucci, M., Leyrat, C., et al. 2003, Icarus, 164, 122

Duffard, R., Pinilla-Alonso, N., Ortiz, J. L., et al. 2014, Astronomy & Astrophysics, 568, A79

Duncan, M. J. 1997, Science, 276, 1670

Durech, J., Delbo, M., Carry, B., Hanus, J., & Ali-Lagoa, V. 2017, 1

Edgeworth, K. E. 1949, Monthly Notices of the Royal Astronomical Society, 109, 600

El Moutamid, M., Sicardy, B., & Renner, S. 2014, Celestial Mechanics and Dynamical Astronomy, 118, 235

Elliot, J., Dunham, E., Bosh, A., et al. 1989, Icarus, 77, 148

Elliot, J. L. 1979, Annual Review of Astronomy and Astrophysics, 17, 445

Elliot, J. L., Ates, A., Babcock, B. A., et al. 2003, Nature, 424, 165

Elliot, J. L., Person, M. J., Zuluaga, C. A., et al. 2010, Nature, 465, 897

Ellis, K., & Murray, C. 2000, Icarus, 147, 129

Ferraz-Mello, S. 1985, Celestial Mechanics, 35, 209

Foreman-Mackey, D., Hogg, D. W., Lang, D., & Goodman, J. 2013, Publications of the Astronomical Society of the Pacific, 125, 306

Fornasier, S., Lazzaro, D., Alvarez-Candal, A., et al. 2014, Astronomy & Astrophysics, 568, L11

Fraser, W. C., Gwyn, S., Trujillo, C., et al. 2013, Publications of the Astronomical Society of the Pacific, 125, 1000

French, R., Nicholson, P., Porco, C., & Marouf, E. 1991, Dynamics and structure of the Uranian rings, ed. J. Bergstralh, E. Miner, & M. Matthews (Tucson, AZ: The University of Arizona Press), 327–409

Gaia Collaboration, Lindegren, L., Lammers, U., et al. 2016a, Astronomy & Astrophysics, 595, A2

Gaia Collaboration, Brown, A. G. A., Prusti, T., et al. 2016b, Astronomy & Astrophysics, 595, A1

Goldreich, P., & Tremaine, S. 1980, The Astrophysical Journal, 241, 425

Goodman, J., & Weare, J. 2010, Communications in Applied Mathematics and Computational Science, 5, 65

Gregory, P. 2005, Bayesian Logical Data Analysis for the Physical Sciences: A Comparative Approach with Mathematica Support, 1st edn. (Cambridge: Cambridge University Press), 488

Guilbert, A., Barucci, M. a., Brunetto, R., et al. 2009, Astronomy and Astrophysics, 501, 777

Guilbert-Lepoutre, a. 2011, The Astronomical Journal, 141, 103

Gunnarsson, M., Bockelée-Morvan, D., Biver, N., Crovisier, J., & Rickman, H. 2008, Astronomy and Astrophysics, 484, 537

Hedman, M. M., & Nicholson, P. D. 2014, Monthly Notices of the Royal Astronomical Society, 444, 1369

Henrard, J., & Lemaitre, A. 1983, Celestial Mechanics, 30, 197

Hinson, D., Linscott, I., Young, L., et al. 2017, Icarus, 290, 96

Horner, J., Evans, N. W., & Bailey, M. E. 2004, Monthly Notices of the Royal Astronomical Society, 354, 798

Horner, J., & Lykawka, P. S. 2010, Monthly Notices of the Royal Astronomical Society, 402, 13

Hubbard, W. B., Hunten, D. M., Dieters, S. W., Hill, K. M., & Watson, R. D. 1988, Nature, 336, 452

Hyodo, R., Charnoz, S., Genda, H., & Ohtsuki, K. 2016, The Astrophysical Journal, 828, L8

Janesick, J. R. 2001, Scientific Charge-Coupled Devices (Bellingham, WA USA: SPIE), doi:10.1117/3.374903

Jewitt, D. 2009, The Astronomical Journal, 137, 4296

Jewitt, D., Garland, C. A., & Aussel, H. 2008, The Astronomical Journal, 135, 400

Jewitt, D., & Kalas, P. 1998, The Astrophysical Journal, 499, L103

Jewitt, D., & Luu, J. 1993, Nature, doi:10.1038/362730a0

Küppers, M., O'Rourke, L., Bockelée-Morvan, D., et al. 2014, Nature, 505, 525

Lellouch, E., Santos-Sanz, P., Lacerda, P., et al. 2013, Astronomy & Astrophysics, 557, A60

Levison, H. F., & Duncan, M. J. 1993, The Astrophysical Journal, 406, L35

Levison, H. F., & Morbidelli, A. 2003, Nature, 426, 419

Luu, J., Marsden, B. G., Jewitt, D., et al. 1997, Nature, 387, 573

Lynden-Bell, D., & Pringle, J. E. 1974, Monthly Notices of the Royal Astronomical Society, 168, 603

Meech, K. J., & Belton, M. J. S. 1990, The Astronomical Journal, 100, 1323

Melita, M. D., Duffard, R., Ortiz, J. L., & Campo-Bagatin, A. 2017, Astronomy & Astrophysics, 602, A27

Meyer-Vernet, N., & Sicardy, B. 1987, Icarus, 69, 157

Mommert, M., Harris, A. W., Kiss, C., et al. 2012, Astronomy & Astrophysics, 541, A93

Mommert, M., Hora, J. L., Harris, A. W., et al. 2014, The Astrophysical Journal, 781, 25

Murray, C. D., & Dermott, S. F. 2000, Solar System Dynamics (Cambridge: Cambridge University Press), 575, doi:10.1017/CBO9781139174817

Ortiz, J. L., Sicardy, B., Braga-Ribas, F., et al. 2012, Nature, 491, 566

Ortiz, J. L., Duffard, R., Pinilla-Alonso, N., et al. 2015, Astron. Astroph., 576, A18

Porco, C. C., Thomas, P. C., Weiss, J. W., & Richardson, D. C. 2007, Science, 318, 1602

Prialnik, D., Brosch, N., & Ianovici, D. 1995, Monthly Notices of the Royal Astronomical Society, 276, 1148

Rousselot, P. 2008, Astronomy and Astrophysics, 480, 543

Ruprecht, J. D., Bosh, A. S., Person, M. J., et al. 2015, Icarus, 252, 271

Santos-Sanz, P., Lellouch, E., Fornasier, S., et al. 2012, Astronomy & Astrophysics, 541, A92

Santos-Sanz, P., French, R. G., Pinilla-Alonso, N., et al. 2016, Publications of the Astronomical Society of the Pacific, 128, 018011

Schindler, K., Wolf, J., Bardecker, J., et al. 2017, Astronomy & Astrophysics, 600, A12

Schmidt, J., Ohtsuki, K., Rappaport, N., Salo, H., & Spahn, F. 2009, Dynamics of Saturn's Dense Rings, ed. M. Dougherty, L. Esposito, & S. Krimigis (Springer), 413

Sekiguchi, T., Ootsubo, T., Hasegawa, S., et al. 2012, in LPI Contributions, Vol. 1667, Asteroids, Comets, Meteors 2012 (LPI), 6477

Sessin, W., & Ferraz-Mello, S. 1984, Celestial Mechanics, 32, 307

Sheppard, S. S., & Trujillo, C. 2016, The Astronomical Journal, 152, 221

Sheppard, S. S., Trujillo, C., & Tholen, D. J. 2016, The Astrophysical Journal, 825, L13

Shu, F. H. 1984, in IAU Colloq. 75: Planetary Rings, ed. R. Greenberg & A. Brahic (Tucson, AZ: University of Arizona Press), 513–561

Sicardy, B., & Dubois, V. 2003, Celestial Mechanics and Dynamical Astronomy, 86, 321

Sicardy, B., Widemann, T., Lellouch, E., et al. 2003, Nature, 424, 168

Sicardy, B., Colas, F., Maquet, L., et al. 2010, in Bulletin of the American Astronomical Society, Vol. 42, AAS/Division for Planetary Sciences Meeting Abstracts #42 (Washington, DC: American Astronomical Society), 993

Sicardy, B., Ortiz, J. L., Assafin, M., et al. 2011, Nature, 478, 493

Sicardy, B., Buie, M., Benedetti-Rossi, G., et al. 2015, in AAS/DPS Meeting Abstracts, Vol. 47, AAS/DPS, 104.01

Tancredi, G., & Favre, S. 2008, Icarus, 195, 851

Thomas, P. 2010, Icarus, 208, 395

Tiscareno, M., Hedman, M., Burns, J., & Castillo-Rogez, J. 2013, Astrophys. J. Letters, 765, L28

Tiscareno, M. S., & Malhotra, R. 2003, The Astronomical Journal, 126, 3122

Trujillo, C. a., & Sheppard, S. S. 2014, Nature, 507, 471

Womack, M., & Stern, S. A. 1997, Lunar Planetary Institute Publication, 28, 1575

Wood, J., Horner, J., Hinse, T. C., & Marsden, S. C. 2017, The Astronomical Journal, 153, 245

Yu, Q., & Tremaine, S. 1999, The Astronomical Journal, arXiv:9904424

Zacharias, N., Finch, C., & Frouard, J. 2017, The Astronomical Journal, 153, 166

Zacharias, N., Finch, C. T., Girard, T. M., et al. 2013, The Astronomical Journal, 145, 44

# Appendix A

# Potential of a homogeneous triaxial ellipsoid

The potential $U(\mathbf{r})$ formally given in Eq. 4.8 can be expanded with terms containing only even values of $m$, i.e. of the form $\cos[2p(L-\lambda_A)]$, where $m = 2p$ ($p$ integer). Outside a homogeneous ellipsoid, it reads (Balmino, 1994)[1]:

$$U(\mathbf{r}) = -\frac{GM}{r}\left\{\sum_{p=0}^{+\infty}\cos\left[2p(L-\lambda_A)\right]\left[\sum_{l=p}^{+\infty}\left(\frac{R}{r}\right)^{2l}C_{2l,2p}P_{2l,2p}\left(\sin\varphi\right)\right]\right\}, \quad \text{(A.1)}$$

where $\varphi$ is the latitude. The reference radius $R$ is given by:

$$\frac{3}{R^2} = \frac{1}{A^2} + \frac{1}{B^2} + \frac{1}{C^2}. \quad \text{(A.2)}$$

The coefficient $P_{l,p}$ is the associated Legendre polynomial[2]:

$$P_{l,p}(u) = (-1)^p \frac{(1-u^2)^{p/2}}{2^l l!}\frac{d^{l+p}}{du^{l+p}}\left[(u^2-1)^l\right]. \quad \text{(A.3)}$$

Note that for $p = 0$, $P_{l,0}$ is the classical Legendre polynomial, usually denoted $P_l(u)$.

Here we consider cases where the particle moves in the equatorial plane $OAB$, so that $\varphi = 0$. Using the binomial expansion of $(u^2-1)^l$, we get:

$$P_{2l,2p}(0) = (-1)^{(l-p)}\frac{(2l+2p)!}{2^{2l}(l+p)!(l-p)!} \quad \text{(A.4)}$$

[1]There is a typo in Balmino (1994), as his summation in $p$ starts at 1, and not at 0 as it should.

[2]Balmino (1994) does not introduce the factor $(-1)^p$ given in the classical definition of the Legendre polynomial, it seems to be transferred to $K_{lp}$ in his Eq. 3. Note that since the even value $2p$ appears in $P_{2l,2p}$, this does not alter the final result.

Moreover (see Boyce 1997):

$$C_{2l,2p} = \frac{3}{R^{2l}} \frac{l!\,(2l-2p)!}{2^{2p}\,(2l+3)\,(2l+1)!} \left(2-\delta_{(0,p)}\right) \times \sum_{i=0}^{\mathrm{int}\left(\frac{l-p}{2}\right)} \frac{(a^2-b^2)^{p+2i}\left[c^2-\frac{1}{2}\left(a^2+b^2\right)\right]^{l-p-2i}}{16^i\,(l-p-2i)!\,(p+i)!i!} \tag{A.5}$$

Because we want both negative and positive values of $p$ in Eq. 4.8, it is convenient that $p$ varies from $-\infty$ and $+\infty$ in Eq. A.1 too. This can be accomodated by replacing the factor $(2-\delta_{(0,p)})$ by 1 in Eqs. A.5, and replacing $p$ by $|p|$ when calculating $P_{2l,2p}$ and $C_{2l,2p}$.

This done, we re-write the generic expansion 4.8 as:

$$U(\mathbf{r}) = \sum_{p=-\infty}^{+\infty} U_{2p}(r) \cdot \cos\left[2p(L-\lambda_A)\right] \tag{A.6}$$

where:

$$U_{2p}(r) = -\frac{GM}{r} \sum_{l=|p|}^{+\infty} \left(\frac{R}{r}\right)^{2l} Q_{2l,2|p|} \tag{A.7}$$

and where $Q_{2l,2|p|} = C_{2l,2|p|} P_{2l,2|p|}(0)$, but taking care of replacing $(2-\delta_{(0,p)})$ by 1 in Eq. A.5 and replacing $p$ by $|p|$, as explained above. This provides the dimensionless coefficient $Q_{2l,2|p|}$:

$$\begin{aligned} Q_{2l,2|p|} = {} & \frac{(-1)^{l-|p|}}{R^{2l}} \frac{3}{2^{(2l+2|p|)}(2l+3)} \frac{(2l+2|p|)!(2l-2|p|)!l!}{(l+|p|)!(l-|p|)!(2l+1)!} \\ & \times \sum_{i=0}^{\mathrm{int}\left(\frac{l-|p|}{2}\right)} \frac{(A^2-B^2)^{|p|+2i}\left[C^2-(A^2+B^2)/2\right]^{l-|p|-2i}}{16^i\,(l-|p|-2i)!\,(|p|+i)!i!}. \end{aligned} \tag{A.8}$$

We can write $A^2-B^2 = (A+B)(A-B) \sim 2R(A-B)$ and similarly, $C^2-(A^2+B^2)/2 \sim -2R(A'-C)$, where:

$$A' = \sqrt{\frac{A^2+B^2}{2}}. \tag{A.9}$$

Then $Q_{2l,2|p|}$ can be re-expressed as:

$$Q_{2l,2|p|} = \frac{3}{2^{l+2|p|}(2l+3)} \frac{(2l+2|p|)!(2l-2|p|)!l!}{(l+|p|)!(l-|p|)!(2l+1)!} \times \sum_{i=0}^{\mathrm{int}\left(\frac{l-|p|}{2}\right)} \frac{1}{16^i} \frac{\epsilon^{|p|+2i}}{(|p|+i)!i!} \frac{f^{l-|p|-2i}}{(l-|p|-2i)!}, \tag{A.10}$$

where we define

$$\epsilon = \frac{A-B}{R} \quad \text{and} \quad f = \frac{A'-C}{R} \tag{A.11}$$

as the elongation and oblateness of the body, respectively[3].

Using Eqs. 4.10 and 4.11, we finally obtain near one isolated $(2p-1)/2p$ LER:

$$U_p^{\mathrm{LER}}(\mathbf{r}) = U_0(a) + e\frac{GM}{a}\left\{\sum_{l=|p|}^{+\infty}\left[4p-(2l+1)\right]Q_{2l,2|p|}\left(\frac{R}{a}\right)^{2l}\right\}\cdot\cos(\phi_{2p}), \tag{A.12}$$

where $\phi_{2p} = 2p\lambda_A - (2p-1)\lambda - \varpi$.

As $Q_{2l,2|p|}$ is globally of order $l$ in $\epsilon f$, we have

$$U(\mathbf{r}) = \sum_{p=-\infty}^{+\infty} U_{2p}(r)\cdot\cos\left[2p(L-\lambda_A)\right] = -\frac{GM}{r}\sum_{p=-\infty}^{+\infty}\left(\sum_{l=|p|}^{+\infty}\left(\frac{R}{r}\right)^{2l}Q_{2l,2|p|}\right)\cos\left[2p(L-\lambda_A)\right].$$

Keeping only the terms $l=|p|$ for each component in $p$:

$$U(\mathbf{r}) \sim -\frac{GM}{r}\sum_{p=-\infty}^{+\infty}\left(\frac{R}{r}\right)^{2|p|}Q_{2|p|,2|p|}\cos\left[2p(L-\lambda_A)\right]. \tag{A.13}$$

## A.1 Axisymmetric part of the potential

Eq. A.7 provides:

$$U_0(a) = -\frac{GM}{a}\sum_{l=0}^{+\infty}Q_{2l,0}\left(\frac{R}{a}\right)^{2l} \tag{A.14}$$

where

$$Q_{2l,0} = \frac{3}{2^l(2l+1)(2l+3)}\frac{(2l)!}{l!}\times\sum_{i=0}^{\mathrm{int}(l/2)}\frac{1}{16^i}\frac{\epsilon^{2i}}{(i!)^2}\frac{f^{l-2i}}{(l-2i)!}. \tag{A.15}$$

This can be compared to the classical expansion for the potential of an oblate spheroid, corresponding to the axisymmetric ellipsoid with $A=B>$

[3]For an axisymmetric ellipsoid (spheroid), $A=A'=B$, and $f\sim(A-C)/A$ coincides with the usual definition of oblateness.

$C$. In this case $\epsilon = 0$, and only the first term with $i = 0$ contributes to the sum above. Therefore

$$Q_{2l,0}(A = B) = \frac{3}{2^l(2l+1)(2l+3)} \frac{(2l)!}{(l!)^2} f^l. \tag{A.16}$$

and

$$U_0(a) = -\frac{GM}{a} \sum_{l=0}^{+\infty} Q_{2l,0}(A = B) \left(\frac{R}{a}\right)^{2l} = -\frac{GM}{a} \left[1 + \frac{f}{5} \left(\frac{R}{r}\right)^2 + ...\right] \tag{A.17}$$

At the lowest possible order ($l = 0$), we have $U_0 = -GM/a$, as expected from the asymptotic behavior of $U(\mathbf{r})$ at large $r$. Another possible classical expansion of $U_0$ for a spheroid is $U_0 = -(GM/r)[1 - \sum_{l=2}^{+\infty} J_{2l}(R/r)^{2l} P_{2l}(0)]$, so that we obtain by identification:

$$J_{2l} = -\frac{Q_{2l,0}(A = B)}{P_{2l}(0)} \tag{A.18}$$

For $l = 1$, we retrieve the classical result $J_2 = (2/5)f$.

## A.2 Resonant terms

The coefficient $Q_{2l,2|p|}$ in Eq. A.12 is globally of order $l$ in the small factor $\epsilon \times f$. Thus, the largest contribution in Eq. A.12 comes from the term $l = |p|$, for which

$$Q_{2|p|,2|p|} = S_{|p|} \times \epsilon^{|p|} \quad \text{where} \quad S_{|p|} = \frac{3}{2^{3|p|}(2|p|+3)} \frac{(4|p|)!}{(2|p|)!(2|p|+1)!} \tag{A.19}$$

Then, we may write Eq. A.13 as:

$$U(\mathbf{r}) = -\frac{GM}{r} \sum_{p=-\infty}^{+\infty} \left(\frac{R}{r}\right)^{2|p|} S_{|p|} \epsilon^{|p|} \cos\left[2p(L - \lambda_A)\right]. \tag{A.20}$$

And finally, using Eq. 4.10, the potential $U_p^{\mathrm{LER}}(\mathbf{r})$ near an isolated $(2p-1)/2p$ LER reads:

$$U_p^{\mathrm{LER}}(\mathbf{r}) = U_0(a) + e\frac{GM}{a} \left\{ \left[4p - (2|p|+1)\right] S_{|p|} \epsilon^{|p|} \left(\frac{R}{a}\right)^{2|p|} \right\} \cdot \cos(\phi_{2p}), \tag{A.21}$$

Table A.1: Values of $S_p$

| $p$ | 0 | 1 | 2 | 3 | 4 | 5 | 6 | 7 | 8 | 9 | 10 |
|---|---|---|---|---|---|---|---|---|---|---|---|
| $S_p$ | 1.000 | 0.1500 | 0.09375 | 0.08594 | 0.09521 | 0.1183 | 0.1587 | 0.2250 | 0.3328 | 0.5084 | 0.7974 |

Notes: values of $S_p$ are rounded off to four significant digits

where $\phi_{2p} = 2p\lambda_A - (2p-1)\lambda - \varpi$. From a numerical point of view, it is better to calculate iteratively $S_{|p|}$, rather than evaluating in Eq. A.19 large factors containing factorials. Using the equation above, we obtain:

$$S_{|p|+1} = 2\frac{(|p|+1/4)(|p|+3/4)}{(|p|+1)(|p|+5/2)} \times S_{|p|} \quad \text{with} \quad S_0 = 1. \tag{A.22}$$

Values of $S_p$ for $p = 1, ...10$ are listed in Table A.1. Fig. A.1 shows that for for large values of $p$, $S_p$ has an exponential behavior with respect to $p$, so that the factor $S_{|p|}\epsilon^{|p|} \propto (1.93\epsilon)^{|p|}$ rapidly tends to zero as $p$ increases, for small values of $\epsilon$.

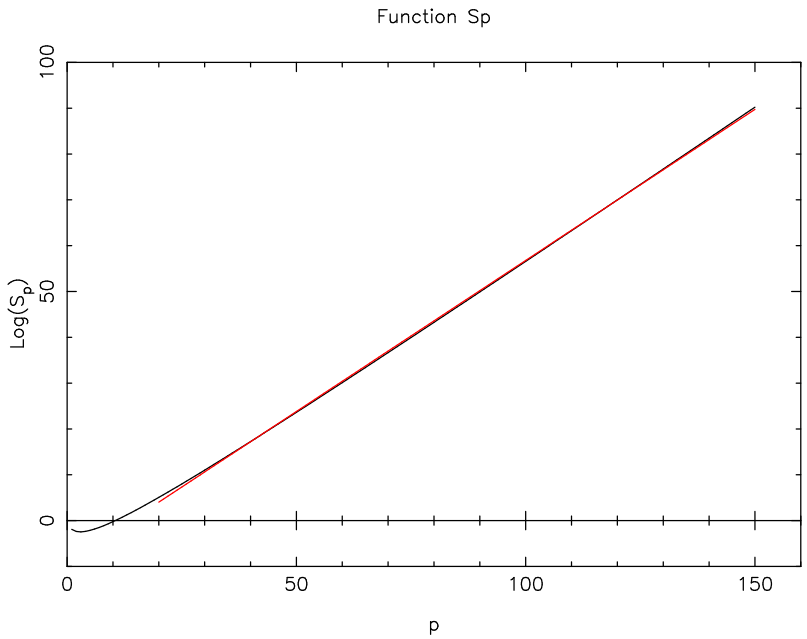


Figure A.1: Values of $\log(S_p)$ vs. $p$. The linear fit (red line) is performed for $m$ between 20 and 150, providing $(p, \log S_p) \sim -9.16 + 0.659p$, corresponding to $S_p \sim 1.05 \times 10^{-4} \times (1.93)^p$.

# Appendix B

# Search for gas emmision from Chariklo with ALMA

As commented in the Introduction, the formation mechanism of the ring system around Chariklo is unknown and among the possible scenarios is the formation of ring by cometary material ejected from the surface of Chariklo. To date, no cometary activity has been detected in this body as dust coma or gas emission.

The escape velocity at Chariklo's surface ($\sim$100 m $s^{-1}$) is comparable to the typical cometary dust ejection velocities expected for Centaurs Delsemme (1982). This raises the interesting possibility that Chariklo's rings could be formed by cometary material ejected from the surface with velocities large enough to prevent an immediate in-fall onto the surface but still small enough to prevent escape to infinity. Such material could thus accumulate in orbit. As mentioned before, the Centaur Chiron, has sporadic cometary activity and, in addition, stellar occultations reveal narrowly confined material around Chiron that could be rings or dust shell Ortiz et al. (2015); Ruprecht et al. (2015). The activity in (2060) Chiron has been modeled as the result of heating associated with crystallization of amorphous water ice Prialnik et al. (1995).

Unexpectedly, SPHERE/VLT observations acquired by our group in July 2015 (with the primary goal of directly imaging the rings) suggest a faint dusty "halo" around Chariklo (Figure B.1, Sicardy et al. (2015)). The halo appears to be elongated in a direction roughly perpendicular to that of the rings and with a 0.18" x 0.12" apparent size (i.e. about 1800 $\times$ 1200 km), i.e.

much more compact than was accessible to previous imaging searches for activity. From the H magnitude of the halo we estimated an optical depth of $\sim 4\times10^{-3}$. The halo could be maintained either by micrometeoroid bombardment on the rings or putative satellites or by faint cometary activity. Current data quality is not sufficient to assess the distribution of material in the halo, for example, we cannot distinguish between a 1/r distribution, expected for a coma due to comet-like activity, from a torus-like distribution (that could result from impact on the rings). Except for the regular monitoring of CO gas in comet 29P/Schwassmann-Wachmann (also classified as a Centaur), molecular searches on Centaurs have proven remarkably difficult. In fact, except for a tentative detection of CO gas in (2060) Chiron at 8.5 AU Womack & Stern (1997), with a reported production rate of $1.5\times10^{28}$ molec. $s^{-1}$ (i.e. comparable to the 29P production rate) and an unconfirmed detection of optical emission of CN from the same object Bus et al. (1991), no gas signatures have been found (while dust activity has been detected in $\sim$10 Centaurs, see Jewitt (2009)). Emphasis has been put on CO searches from mm/submm spectroscopy, and typical upper limits on the production rates are of order (1-5)$\times10^{28}$ molec. $s^{-1}$ Bockelee-Morvan et al. (2001),Jewitt et al. (2008). As regards the specific case of Chariklo, and assuming a gas kinetic temperature of 10 K, Bockelee-Morvan et al. (2001) derived upper limits of $2\times10^{28}$ molec. $s^{-1}$ for CO ($\sim 10^3$ kg $s^{-1}$) and $8\times10^{27}$ molec. $s^{-1}$ of HCN ($\sim$ 400 kg $s^{-1}$), indicating a strong apparent depletion in volatiles compared to comets.

**ALMA proposal** PI: R. Leiva. Co-Investigators: E. Lellouch; N. Biver; R. Moreno; L. Vanzi; B. Sicardy; D. Bockelee-Morvan; L. Maud.

In that context, we proposed to perform a deeper search of CO gas production with ALMA, at unprecedented sensitivity (factor of 10 fainter), with the goals of revealing for the first time a cometary activity for Chariklo and constraining ring origin models. The observation proposal was accepted during ALMA Cycle 4. Observations were completed for the TP-Array and the 7-meter array while for the extended array 2 out the 3 planned scheduling observation blocks were satisfactory observed. The data is currently in Quality Assurance stage 2 awaiting for delivery.

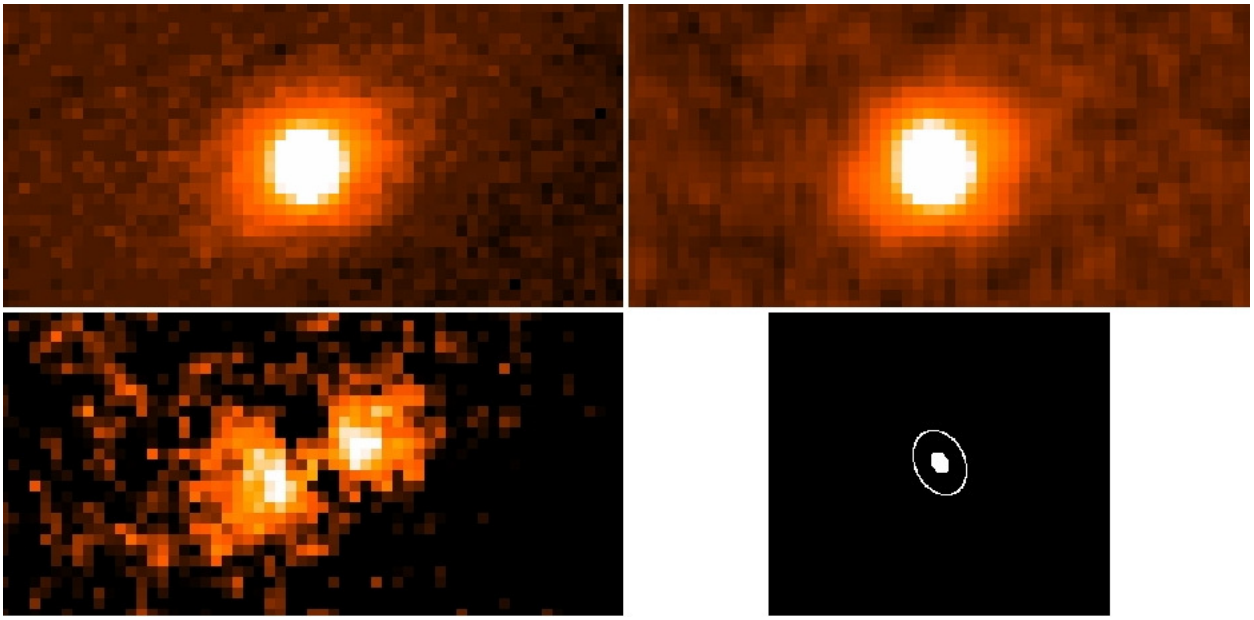

Figure B.1: Top left : The Chariklo image obtained by VLT/SPHERE on 21 July 2015, H-band, 15 min exposure time. Bottom left: subtraction of the observed image and a synthetic image based on the Chariklo+ring model shown in bottom right panel. A residual halo is revealed. Top right: synthetic Chariklo image using a model with Chariklo+ring+halo, after convolution by the stellar PSF, which satisfactorily reproduces the observation.

The proposal consist in the search for CO gas through the J=2-1 line at 230.538 GHz. Due to its volatility, CO is the most likely gas species to be produced in cometary activity at Centaurs distance from the Sun. As demonstrated by its detection in distant comets (e.g. in C/1995 O1 Hale-Bopp up to 14 AU Biver et al. (2002) and in 29P/Schwassmann-Wachmann at ∼6 AU Gunnarsson et al. (2008) and tentatively in Centaur Chiron at 8.5 AU Womack & Stern (1997), low J-transitions are best suited given the cold coma temperatures. Assuming plausible coma temperatures of 5 K to 20 K at ∼15 AU, the current heliocentric distance of Chariklo, the J=2-1 line appears the most favorable. To assess feasibility, we calculated the expected integrated linestrengh for a CO production of 2 $\times 10^{27}$ molec. $s^{-1}$, i.e. an order of magnitude lower than previous limits. We used a comet model (Haser density distribution, expansion velocity of 0.45 km/s Biver et al. (2002) and transition from LTE at the specified gas temperature in

the inner coma to radiative regime further out, taking into account infrared pumping by the Sun) and calculated the signal in the synthesized beam as a function of angular resolution, for several configurations of the 12m array as well as for the characteristic resolution of the ACA 7-m and the Total Power (TP) arrays (Figure B.2). As a comet model leads to a slow (1/r) flux decrease with distance to the nucleus (meaning also that there is strictly speaking no largest angular scale to the emission), the most compact configurations are the most sensitive, for a given collecting area. Therefore, the C40-1 configuration appears to be the most favorable one for the 12-m array, and the ACA-7m and TP are desired to probe the maximum extent of the emission. Requesting the ACA-7m and TP arrays along with the C40-1, the time multipliers for the ACA-7m and TP arrays (factors 5 and 8.5 respectively) are such that the maximum sensitivity is actually obtained with the TP array. Requesting 2 h on source for the 12-m array (3.3 hr 12-m time), we anticipate a detection of the CO(2-1) line at 4-10 $\sigma$ for a production rate of 2 $\times 10^{27}$ molec. $s^{-1}$ and gas temperatures of 5 to 20 K.

The above calculations are for a comet-like model of gas emission. This is justified because Chariklo's escape velocity is $\sim$0.1 km/s. Hence gases emanating from the body surface at typical velocities a few times larger are expected to be little affected by the object gravity field (for example, velocities of $\sim$0.5 km/s towards the Sun are observed on 29P/Schwassmann-Wachmann). We note however, that Chariklo might represent an interesting transition case between comet-like atmospheres and gravitationally-bound tenuous atmospheres (e.g. Io's and Pluto's, with escape velocities of 2.6 and 1.2 km/s). This scenario would be consistent with the very confined dusty halo visible in the VLT/SPHERE images. In this case, the CO emission would also be stronger and somewhat more confined than the above comet model predicts, warranting the need of the 12-m array in configuration C40-1 along with the ACA and TP arrays.

The observations, as planned, will permit to reach a detection sensitivity an order of magnitude deeper than previous searches. Note also that Chariklo's current southern declination (-33°) forbids an observation from any Northern hemisphere radio-telescope. If successful, the derived CO production rates will permit to (i) constrain the mechanism of ring forma-

tion from comet-like activity (ii) estimate a gas-to-dust ratio (once the dust halo will also be better characterized). More broadly, our observations will address the general question of the "comet-asteroid continuum", i.e. the blurring of the comet / asteroid boundary evidenced by the existence of orbitally and physically intermediate bodies (e.g. dormant comets, main-Belt comets, a.k.a. active asteroids...), the presence of water ice on several asteroids, and the recent spectacular gas detections, e.g. on Ceres Küppers et al. (2014) and on near-Earth asteroid (3552) Don Quixote Mommert et al. (2014). Beyond the process of ice sublimation that is at work in comets, asteroid activity may include a variety of mechanisms (see Jewitt (2009)). The detection of gas activity in the Centaur region would permit to estimate the amount of exposed CO ice on these objects, and by comparison to comets constrain their evolution and the activity mechanisms at work.

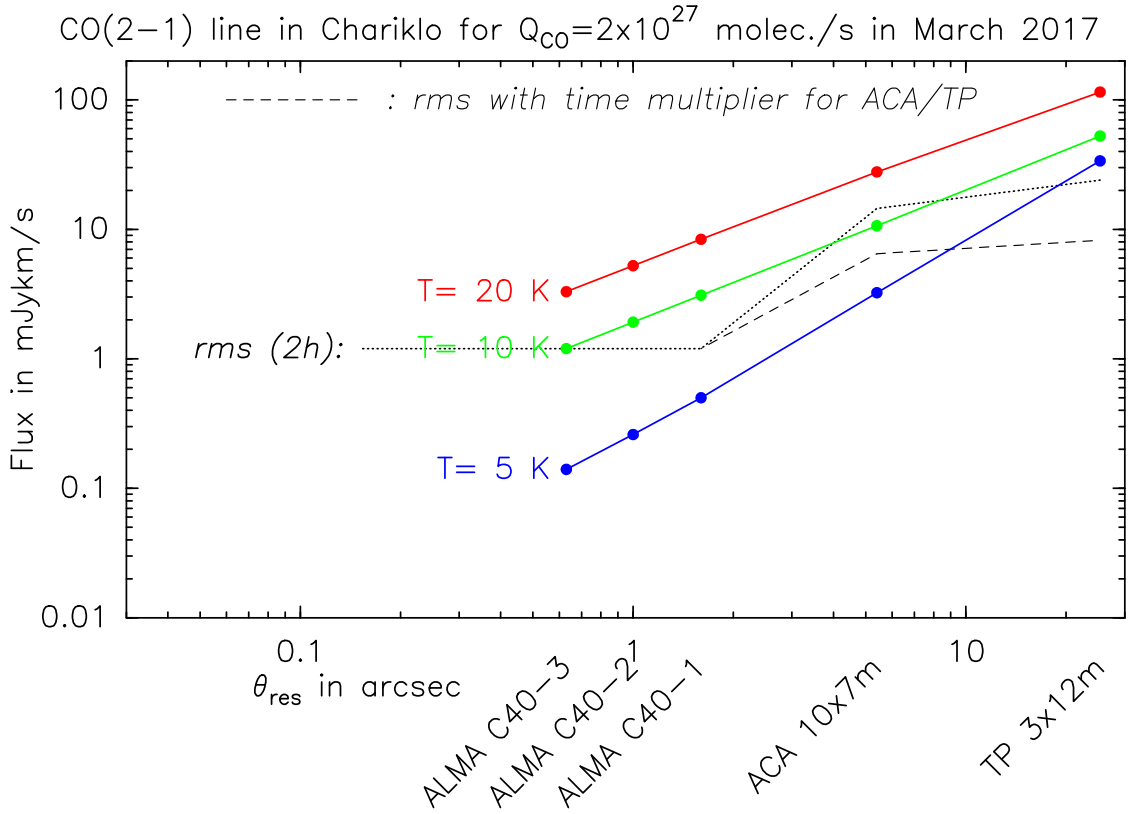


Figure B.2: Expected CO(2-1) line flux (mJy. km/s) for a CO production rate of $2\times10^{27}$ $s^{-1}$, different assumptions for the gas temperature (5, 10 and 20 K) and different spatial resolutions, corresponding to different ALMA, ACA and Total Power (TP) configurations. The dotted line shows the rms achievable in 2 hours on source (line width of 1 km/s). The dashed line is the rms achievable when allowance is made for multiplier time factors (5 for ACA and 8.5 for TP, respectively).

# Appendix C

# Other observations

The Table C.1 summarized all observations of stellar occultations that I performed. Several observations were done from the Pontificia Universidad Católica de Chile Observatory, located about 20 km from the center of Santiago, Chile. All observations from Santiago were done with a 40 cm telescope Meade LX200 equipped with an EMCCD camera Merlin Raptor. The UTC time was initially obtained using NTP servers and later on (starting in 2014) from a local GPS equipped with a PPS signal to improve the absolute accuracy (see section 2.3 for details about the timing accuracy) .

From fifteen observations involving five TNOs and one Centaur object, there were three positive detections and 1 no-detection. Results from these observations had been included in 3 publications as co-author, were my involvement was as observer and preliminary reduction of the data.

Quaoar is one of the largest TNOs and observations from the Quaoar occultation in 2011 provided the first accurate determination of the equivalent radius $R_{eq} = 555 \pm 2.5\ km$, a geometric albedo $p_V = 0.109 \pm 0.007$ and a density $\rho = 1990 \pm 460 kgm - 3$ under the assumption of hydrostatic equilibrium Braga-Ribas et al. (2013).

The stellar occultation by Pluto in 2012 July 18 provided one grazing chord from PUC Observatory out of the five positive detections. This occultation included an observation with NACO at VLT observatory, which is to date one the stellar occultation lightcurve witht the best SNR. In combination with a multi-chord stellar occultation observed May 4th 2013, this observation allowed to derive constraints on Pluto's atmospheric profiles, that is, density, pressure and temperature as a function of radius (Dias-

Table C.1: Observations of stellar occultations from Observatory UC.

| Date | Object | Observers | Result |
|---|---|---|---|
| 26/04/2015 | Chariklo | LV, RL | No detection |
| 16/2/2014 | Chariklo | LV, RL | Cloudy |
| 3/6/2013 | Chariklo | LV, RL | Ring discovery |
| 20/5/2013 | Ixion | RL, MT | No detection (Low SNR) |
| 7/5/2013 | Chariklo | LV, RL | No detection |
| 4/5/2013 | Pluto | LV, RL | Cloudy |
| 9/9/2012 | Pluto+Charon | RL, JMF | No detection |
| 24/8/2012 | Pluto+Charon | LV, RL, JMF | No detection |
| 18/7/2012 | Pluto | RL, JMF | Grazing atmosphere |
| 22/6/2012 | Ixion | LV, RL, JMF | No detection |
| 19/6/2012 | Ixion | LV, RL, JMF | No detection |
| 7/12/2011 | 2002 WC19 | LV, RL | Cloudy |
| 16/8/2011 | 2003 OP32 | LV, RL | Cloudy |
| 4/6/2011 | Pluto | LV, RL, IT | Detection |
| 4/5/2011 | Quaoar | LV, RL, IT | No Detection * |

Note. — A summary of stellar occultations by TNOs and Centaur objects observed from the Observatory UC, Santiago, Chile. Observatios Observers are Rodrigo Leiva (RL), Leonardo Vanzi (LV), Jose Miguel Fernandez (JMF) and Ignacio Toledo (IT).

Oliveira et al., 2015). Among the main results from these observations is the increase of Pluto atmospheric pressure about 6% in a time period of 9 months (this is the pressure at a reference radius r = 1275 km from the center of Pluto) confirming that Pluto's atmosphere was still expanding more than 20 years after its perihelion and three years before the arrival of New Horizons to the Pluto system. The radius of Pluto determined from this occultations $R = 1190 \pm 5$ km was consistent between error bars with the radius of $R = 1189.9 \pm 0.2$ km determined in the New Horizons flyby (Hinson et al., 2017).

The occultation by the Pluto-Charon system in June 4 2012 was observed from 4 sites in South America. From Santiago was visible the occultation by Pluto while the remaining 3 stations in (2 in Chile and 1 in Brazil) detected the occultation by Pluto and Charon. These results remain unpublished.

Finally, the occultation by the Centaur object Chariklo in 2013 June 3 was the fifth detection of rings in the Solar System, and the first around a small object. The observations performed from Santiago with exposure times of 1 second, provided a strong constraint in the location of the rings helping to derive the geometry of the ring system respect to the Chariklo's main body (Braga-Ribas et al., 2014b).

I also participated as PI in proposal for telescope time to observe stellar occultations, photometry to derive the rotational light curve of Chariklo close to a stellar occultation, and astrometry to improve Chariklo's predictions.

The program CNTAC 2016A at SARA-CT Telescope was accepted awarding six night to observe stellar occultation by the Centaur object Chariklo. Four night had good weather and were effectively used from were I obtained no detection of the occultation.

The program CN2016A-87 at the MPG 2.2m telescope was accepted awarding one night to perform astrometry of Chariklo and improve its orbit with the goal of improving the accuracy of the prediction of stellar occultations.

The program CLN2017AB-008 at the LCO-GT network was accepted awarding 10 hours to perform differential photometry of Chariklo and recover its rotational light curve close to a stellar occultation with the aim to

constrain its size, shape and orientation.